Seismic and aseismic slip : the Japanese subduction zone

Blandine Gardonio

Communauté UNIVERSITÉ Grenoble Alpes

THÈSE

Pour obtenir le grade de

DOCTEUR DE LA COMMUNAUTÉ UNIVERSITÉ GRENOBLE ALPES

Spécialité : **Terre Solide**

Arrêté ministériel : 25 mai 2016

Présentée par

Blandine Gardonio

Thèse dirigée par **David Marsan, Michel Campillo et Michel Bouchon**

préparée au sein de **ISTerre**
et de l'école doctorale **Terre Univers Environnement**

Glissements sismiques et asismiques : le cas du Japon

Thèse soutenue publiquement le **2 Mars 2017**,
devant le jury composé de :

David Marsan
Professeur à ISTerre Université Savoie Mont-Blanc, Chambéry, Directeur de thèse
Michel Campillo
Professeur à ISTerre Université Grenoble Alpes, Grenoble, Directeur de thèse
Michel Bouchon
Directeur de Recherche CNRS ISTerre, Grenoble, Directeur de thèse
Aitaro Kato
Associate Professor Earthquake Research Institute, The University of Toyo, Japon, Rapporteur
Raùl Madariaga
Professeur à l'ENS, Paris, Président
Alexandre Schubnel
Chargé de Recherche CNRS ENS, Paris, Examinateur
Anthony Sladen
Chargé de Recherche CNRS Géoazur, Nice, Examinateur
Olivier Lengliné
Maître de Conférence EOST, Université de Strasbourg, Strasbourg, Invité

Remerciements

Des scientifiques ont récemment prouvé que le Bonheur avait plusieurs origines :

- il proviendrait pour 50 % environ de la génétique.

Pour cela, j'aimerais remercier mes parents. Merci de m'avoir doté de tels gènes. Merci de m'avoir soutenue tout au long de mon projet, merci d'avoir été là à chacun de mes pas, les plus petits comme les plus grands, les plus trébuchants comme les plus sûrs et ce, depuis le tout premier.

Cette génétique me provient également de mes grands-parents et j'ai une pensée toute particulière pour mes Nonni car, grâce à ses sacrifices, j'ai la chance aujourd'hui de pouvoir faire le travail que j'ai choisi. Une pensée également à ma grand-mère Méyette qui nous a quitté récemment. Je l'imagine sur le trajet Lyon-Grenoble dans sa R5. . . en première. Elle m'aurait sûrement dit avec son accent dauphinois : « J'ai pas tout compris ce que tu as présenté, mais je suis bien fière de toi ma P'titoune ».

Cette génétique, je la partage en partie avec ma Big Sis d'amour. Qui est ma soeur jumelle. . . à 3 ans près. . . Merci pour tous tes encouragements, merci pour ta présence inestimable. Et biensûr, une grande pensée pour le frangin qui a la primeur des séismes que j'analyse quelques années plus tard. . .

Merci également à cette génétique qui fait que j'ai une famille sur qui je peux compter : ma tante, mes cousins. Et ce n'est pas la seule famille que je compte dans mon coeur car j'ai la chance d'avoir des Belles, des très jolies familles. Le clan Bouygues-Aizac-Lafaurie-Gardonio tient une place toute particulière dans mon coeur. Et biensûr, je tiens à remercier mes belles-mamans (Hélène, Ninette et Véro) ainsi que mes beaux-papas (Guy, Jacques et Pascal) pour leurs encouragements et leur aide tout au long de ce parcours.

40 % de notre bonheur viendrait de nos choix de vies, des rencontres que l'on fait, si on est heureux dans notre activité.

Il est certain que les belles rencontres ont marqué ma vie comme cette rentrée en petite section de maternelle où j'ai rencontré une petite brunette du nom de Coralie. On peut dire donc que tu as été présente pour le début et la fin de ma scolarité Coco ! Et puis, plus tard, les amitiés qui se forgent à l'adolescence et qui s'ancrent en nous, merci Tiphaine pour le bonheur que l'on vit ensemble au grès des colos et de la vie. Un immense merci à ma Magou qui a toujours été là pour moi et à Marine, la plus folle de toutes vous savez toujours me faire rire. Biensûr, il y a aussi toi, ma petite Marion

avec qui je partage les bonheurs de la vie et les petits bobos. Les affres et les joies de la maternité ;).

En ce qui concerne le bonheur dans l'activité, je tenais à remercier Pierre Laurent, car c'est en discutant avec lui que j'ai choisi de me tourner dans la recherche publique à la fin de mon Master 1. Merci à Mai-Linh de m'avoir présentée à Michel Bouchon et un immense merci à Michel et David de m'avoir supportée ces presque cinq dernières années.

Merci à Michel Campillo, d'avoir confirmé, grâce au cours de M1 et M2, que c'était bien la sismologie qui me passionnait. Merci également pour nos nombreuses discussions.

Merci Michel Bouchon pour ta bienveillance et ton enthousiasme permanent. Je sais grâce à toi que l'essentiel dans la recherche est de se faire plaisir ! Il me reste beaucoup à découvrir mais je n'oublierai jamais que l'essentiel et de faire ce qui nous plait, ce qui nous stimule. Je pars avec un bagage inestimable d'avoir travaillé à tes côtés. Tu m'as beaucoup appris sur comment mener les recherches (observer, observer et observer !). J'espère que je saurai transmettre à mes futurs étudiants l'enthousiasme que tu m'as donné.

Enfin, un merci tout particulier à toi, David. Tu m'as soutenue ces cinq dernières années, de stage en stage puis au long de cette thèse. Tu as su réfraîner mon enthousiasme lorsque je pensais pouvoir publier le prochain Science ou Nature et tu as su me remotiver quand j'étais au plus bas. Tu m'as poussée à donner le meilleur de moi même et tu m'as considérée comme une collègue. Merci de m'avoir traitée en tant que tel ;). Merci pour les soirées jeux, désolée de te battre à plâte couture à chaque fois...

Merci au laboratoire ISTerre où il fait bon être étudiante ! et merci à mes collègues qui sont vite devenus des amis. Je pense tout particulièrement à Virginie (une super prof et amie !), Bertrand, Vincent, Jorge, Okba,... Une pensée particulière pour mes premiers co-bureaux Anne, Jean et Isabella et biensûr pour ma Marie qui me manque un peu plus chaque jour mais grâce à qui j'ai une super culture musicale ! Un immense merci à Camille qui sait partager sa bonne humeur et son enthousiasme ! Merci à toute l'équipe des Flying Earth (ce nom déchire grave !) sans oublier les équipes Failles et Cycles. Les meilleures du labo, bien entendu !

Enfin, 10% du bonheur vient des conditions extérieures, du pays dans lequel on vit etc. . .. On arrive donc à 100

A ces 100% de bonheur, je peux doubler la mise. Et pour ça, je te remercie mon Chewie d'être là à mes côtés chaque jour, les bons comme les mauvais. Tu es mon rock (ah ah petit jeux de mots). Merci pour ton soutien sans failles (ah ah le 2e jeu de mot). Tu as su me donner du recul et de la motivation quand j'en avais besoin. Tu me connais mieux que personne... Et notre plus grande réalisation ces trois dernières années n'est certes pas ma thèse mais une jolie petite Chewbizette qui aime déjà collectionner des cailloux et qui nous apporte un bonheur sans limite...

Résumé

L'existence de glissements lents a été observé pour la première fois en Californie, sur une portion de la faille de San Andreas (Steinbrugge et al., 1960; Tocher, 1960). Ils ont ensuite été détéctés dans les années 90s avec l'avènement des GPS. Les interactions entre glissement lents, ou glissements asismiques (qui n'émettent pas d'ondes élastiques) et les glissements sismiques est cependant mal connue. Pourtant, cette question est fondamentale puisque des glissements lents ont été observés avant plusieurs séismes.

Par exemple, l'installation d'un glissement lent avant le séisme d'Izmit de 1999 en Turquie a été mise en évidence grâce à l'analyse de signaux répétitifs (Bouchon et al., 2011). De même, en étudiant le comportement des séismes répétitifs avant le méga-séisme de Tohoku de 2011, deux séquences de glissement lent en direction du point d'initiation ont été observées (Kato et al., 2012). D'autres glissements lents précédents des séismes de grandes ampleurs ont été reportés, notamment au Mexique, avant le séisme de Papanoa (Radiguet et al., 2016) de magnitude 7.3 et au Chili, avant le séisme d'Iquique de 2014 de magnitude 8.2 (Ruiz et al., 2014).

L'objectif de ce travail de thèse est de mieux caractériser les interactions qui existent entre glissements sismiques et asismiques dans une zone de subduction très largement instrumentée : le Japon. La très grande densité des réseaux Japonais (sismique courte et longue période, GPS) autorise des seuils de détection des glissements sismiques ou lents très bas, et permet d'utiliser des méthodes de réseaux afin de maximiser le rapport signal sur bruit. La recherche d'épisodes de déformation lente est basée sur plusieurs types d'observables et de méthodes, et est complétée par l'analyse des changements de taux de sismicité accompagnant ces épisodes. Cette thèse vise ainsi à mieux comprendre comment du glissement lent peut -ou non- accélérer l'occurrence de grands séismes, et les conditions requises pour se faire.

Abstract

Transient aseismic slip events (that do not emit elastic waves) were first discovered on the San Andreas fault in central California in 1960 (Steinbrugge et al., 1960; Tocher, 1960) and were later confirmed by the development and installation of GPS stations. Aseismic slip can occur on continental faults as well as on subduction zones. However, the interactions between aseismic and seismic slips are not fully captured yet. Understanding the mechanisms at stake on fault planes is fundamental since several large earthquakes were preceded by aseismic slip episodes.

For example, the setting of a slow slip event before the 1999 Izmit earthquake in Turkey was evidenced by the observation of repeating signals at one station (Bouchon et al., 2011). Also, by studying repeating earthquakes before the 2011 Tohoku earthquake, two slow slip episodes that migrated towards the rupture intitiation were observed (Kato et al., 2012). Other transient slips preceding large earthquakes occurred, including in Mexico, before the M7.3 Papanoa earthquake (Radiguet et al., 2016) and in Chile, before the 2014 Iquique earthquake (Ruiz et al., 2014).

The aim of this thesis is to better characterize the interactions between seismic and aseismic slip that can occur in a subduction zone largely instrumented : Japan. The very high density of the japanese monitoring networks (seismic networks, both at short and long periods, and GPS network), allows the detection of seismic and aseismic slip events with low intensity / size, and is amenable to the use of array methods to improve the signal-to-noise ratio. The search for episodes of transient deformation will be based on several observables and techniques, and is complemented by the analysis of the changes in earthquake rates concomittent to these episodes. This work thus gives new clues on how aseismic deformation can -or not- accelerate the occurrence of strong earthquakes, and on what are the conditions (tectonic, dynamic) for this to happen.

Table des matières

Introduction

Les tremblements de terre ont intrigué les populations depuis l'Antiquité. Le tout premier sismomètre au monde a été inventé en Chine, en l'an 132 après Jésus-Christ. Des nombreuses théories sont nées en Chine, en Grèce ou au Japon pour expliquer ce phénomène dévastateur. Nous pouvons citer celle du pneuma : Aristote avait émis l'hypothèse que les séismes étaient dûs à l'exhalaison sèche qui, au lieu de se diriger vers l'atmosphère pour donner naissance aux vents, se dirigerait à l'intérieur de la Terre pour donner naissance aux séismes. Cette théorie a séduit de nombreux philosophes par la suite, notamment Lucrèce, Sénèque, Pline. et a également été reprise au Moyen Âge (Isidore de Séville, Bède le Vénérable,...). Pendant la Renaissance, la théorie du pneuma a légèrement évolué : des gaz seraient la source des séismes mais ils seraient dus à des explosions souterraines de matière inflammable comme le soutenait le philosophe et chanoine Pierre Gassendi.

Au XVIIIième siècle, la Révolution Industrielle est en marche, elle apporte son lot de découvertes dont l'éléctricité. Une théorie nouvelle apparaît alors lancée par William Stukeley en Angleterre : " suivant les mêmes principes que, si un nuage non-électrique décharge son contenu sur n'importe quelle partie de la terre, lorsque celle-ci est dans un état hautement électrifié, un tremblement de terre doit nécessairement s'ensuivre."

Le séisme de Lisbonne en 1755 (magnitude estimée entre 8,6 et 9) qui a fait entre 50 000 et 70 000 victimes a très largement marqué les esprits mais ce n'est qu'au siècle suivant que les premières analyses sur les tremblements de terre sont lancées. Le XIXè siècle est riche en études scientifiques : Robert Mallet a écrit un rapport sur le séisme de Basilicate qui a eu lieu en 1857 ; Alexis Perrey a laborieusement catalogué tous les séismes anciens et contemporains. Ce travail a par la suite été repris par Montessus de Ballore pour relier les séismes à des structures géologiques.

Au Japon, le sismologue Fusakichi Omori a observé de nombreuses séquences de séismes à la fois sur des enregistrements de formes d'ondes mais aussi sur le terrain. Son étude de la sismicité globale a permis notamment de voir que les répliques d'un séisme ont une distribution caractéristique en temps et en espace. Il s'est notamment rendu à San Fransisco en 1906, suite au séisme qui a ravagé la ville.

Les premières théories sur les origines mécaniques des séismes émergent alors. En 1911, H.F. Reid proposa que les séismes fussent dus à un relâchement de contrainte causé par un cisaillement soudain sur une faille. Quelques années plus tard, Wegener propose la théorie de la tectonique des plaques pour expliquer la dérive des continents.

Cette hypothèse ne fera consensus que tardivement, dans les années 60. C'est alors que l'origine tectonique des séismes est mise en évidence. En parallèle, les ondes sismiques ont été utilisées pour imager l'intérieur de la Terre notamment par la première femme sismologue, Inge Lehman, qui a, grâce à ses travaux, démontré l'existence de la graine solide.

La seconde partie du XXe siècle a donné lieu à de nombreuses expériences afin de mieux comprendre l'origine mécanique des tremblements de terre. Le mécanisme de « stick-slip », ou patin-ressort, utilisé comme analogie aux séismes a notamment été proposé par Byerlee et Brace lors d'expériences réalisées sur des échantillons de granite (Brace and Byerlee, 1966, 1968). Suite à ces travaux, deux lois ont émergé afin d'expliquer la nucléation de glissements instables : « slip-weakening law » pour laquelle le coefficient de friction ne dépend que du glissement (Ida, 1972; Campillo and Ionescu, 1997; Uenishi and Rice, 2003) et la loi rate-and-state pour laquelle le coefficient de friction dépend du taux de glissement et d'une variable d'état (Dieterich, 1979; Dietrich, 1979; Ruina, 1983; Marone, 1998). Parallèlement aux développements expérimentaux, des observations sur le terrain ont permis de découvrir un tout nouveau type de glissement : le glissement asismique. Il a été découvert sur un segment de la faille de San Andreas en 1960 (Steinbrugge et al., 1960; Tocher, 1960).

Une zone de transition a été identifiée à Parkfield entre la portion glissante de façon asismique de la faille de San Andreas et la portion qui a rompu lors d'un grand séisme qui a eu lieu en 1857. Plusieurs séismes de magnitude 6 ont eu lieu dans cette zone (1922, 1934, 1966, 2004). L'analyse des sismogrammes des séismes qui ont lieu à Parkfield ont mis en évidence des ruptures, des magnitudes ainsi que des mécanismes au foyer similaires (Bakun and McEvilly, 1984; Bakun and Lindh, 1985). Il s'agirait donc de séismes répétitifs. D'autres séismes répétitifs ont été identifiés dans la zone de transition avec des temps de récurrence de quelques mois à quelques années (Nadeau et al., 1995; Nadeau and Johnson, 1998). Ces séismes répétitifs ont lieu sur la même aspérité qui est supposée être régie par le glissement sismique l'entourant (Ellsworth and Beroza, 1995; Nadeau and McEvilly, 1999; Igarashi et al., 2003). Ils peuvent donc être utilisés comme marqueurs de glissement lent.

Des signaux répétitifs ont eu lieu avant le séisme d'Izmit, en Turquie (Bouchon et al., 2011). Les auteurs suggèrent l'installation d'un glissement lent pour expliquer cette sismicité particulière. De même, en étudiant le comportement des séismes répétitifs avant le méga-séisme de Tohoku-oki de 2011, deux séquences de glissement lent en direction du point d'initiation ont été suggérées (Kato et al., 2012). D'autres glissements lents précédents des séismes de grandes ampleurs ont été reportés, notamment au Mexique, avant le séisme de Papanoa, grâce à l'analyse de données GPS (Radiguet et al., 2016) ainsi qu'au Chili, avant le séisme d'Iquique de 2014 de magnitude 8.2, grâce à une analyse combinée des données GPS et de la sismicité (Ruiz et al., 2014).

Le lien entre glissement lent et séisme est particulièrement marquant au Japon, au niveau de la péninsule de Boso où des glissements lents ont lieu de façon régulière, toujours accompagnés d'une augmentation de la sismicité régionale.

Le Japon est une zone tectonique complexe qui est largement instrumentée. Cette immense quantité d'informations disponible permet une analyse fine des signaux sismiques par le biais de différents outils. On cherche donc, dans cette thèse, à mieux comprendre les interactions entre les glissements lents et les glissements plus rapides qui produisent des séismes. Différentes analyses de la sismicité, et notamment des séismes répétitifs permettent d'obtenir une image plus fine de l'interaction entre glissements sismiques et asismiques.

Dans un premier chapitre, nous aborderons tout d'abord les notions de glissements sismiques et asismiques. Nous commencerons par présenter différentes observations d'interactions sismiques et asismiques sur les zones de faillles. Nous introduirons ensuite un modèle mécanique qui permet de décrire ces deux types de glissement. Nous présenterons ensuite les séismes répétitifs. Pourquoi sont-ils d'une grande importance dans le lien entre glissements sismiques et asismiques ?

Le second chapitre est consacré à la présentation du contexte tectonique du Japon. Nous allons introduire les différents types de glissements observés ainsi que les interactions qui existent entre ces glissements. Nous décrirons ensuite l'activité sismique ayant lieu sur les trois zones d'étude sur abordées dans ce manuscrit : la zone de rupture du séisme de Tohoku, la Péninsule de Boso et la zone de Kanto.

Pour la suite du manuscript, nous étudierons les interactions entre glissements sismiques et asismiques qui peuvent avoir lieu au cours d'un cycle sismique.

Nous commencerons par aborder la phase pré-sismique au cours du Chapitre 3. Nous présenterons une méthode basée sur l'analyse multidimensionnelle de signaux sismiques. Cette approche, sous réserve de conditions de réseau bien particulières, permet la détection d'évènements sismiques cachés par du bruit ou des codas sismiques. Un exemple de l'application de l'analyse multidimensionnelle sera présenté dans ce chapitre. Nous avons analysé les signaux sismiques trois mois avant le méga-séisme de Tohoku-oki. En utilisant près de 500 séismes, nous avons été capables de trouver 465 séismes non catalogués. L'analyse spatio-temporelle de cette nouvelle sismicité a permis de confirmer la mise en place d'une phase de migration 23 jours avant le séisme de Tohoku-oki. De plus, la phase d'activation de la région débute en Novembre 2010 pour se terminer quelques jours avant le mégaséisme où une quiescence est observée.

Dans le quatrième chapitre, nous aborderons les interactions entre glissements sismiques et asismique lors de la phase cosismique et plus précisément, lors de la rupture d'un glissement lent dans la zone de Boso. Grâce à une analyse combinée de signaux sismiques et de signaux GPS, nous sommes en mesure d'établir une nouvelle histoire de glissement au niveau de cette région bien connue pour ces séismes lents. Nous aborderons également les différences entre les glissements lents successifs et les conséquences sur l'activation de la sismicité dans cette zone proche de la ville de Tokyo.

Dans le cinquième chapitre, nous terminerons l'analyse des interactions entre glissement sismique et asimique lors du cycle sismique en présentant les conséquences du séisme de Tohoku-oki sur la sismicité dans la zone de Kanto. L'analyse des séismes répétitifs dans la zone a permis de mettre en évidence une augmentation du taux sismique des

deux plaques en subduction. De plus, les magnitudes des séismes répétitifs augmentent après le mégaséisme. Cela suppose l'installation d'un glissement lent sur les deux plaques en subduction dans la zone de Kanto.

Le dernier chapitre, consiste en une discussion/conclusion où nous aborderons les différents résultats obtenus au cours de cette thèse afin de résumer ce que nous avons pu apprendre sur le lien qui existe entre glissements sismiques et asismiques. En conclusion, nous synthétiserons les principaux résultats apportés par ce travail. Nous discuterons également des développements futurs qu'il reste à accomplir.

Chapitre 1

Seismic and Aseismic slip : observations and definitions.

In this chapter, we define the seismic and aseismic slip and present the interactions of these two types of slip. First, we present the different observations that were made in the field. Then, we briefly introduce the laboratory-derived rate-and-state friction law that models the interactions between seismic and aseismic slip. We will see that it also fully describes the seismic cycle.

The second part of the chapter presents the interactions that exist between seismic and aseismic slip. In order to fully capture this link, first, we mechanically define what is an asperity and how it is related to the surrounding medium that we call anti-asperity. Then we introduce Repeating Earthquakes (REs) and present how they can be used as proxys to assess the aseismic slip.

1.1 Observations on faults.

Interactions between seismic and aseismic slip occur during the seismic cycle. For example, the observation of a slip that occurred after a large event was done after the 1994 Mw 7.6 Sanriku, Japan earthquake, and was made possible thanks to the development of geodetic instruments (Heki and Tamura, 1997). This systematic postseismic slip can last up to years and can be located outside the coseismic slip zone for its most part : this corresponds to the postseismic slip.

Geodetic instruments revealed themselves as powerful tools to detect slip transients in subduction zones, especially Slow Slip Events (SSEs) in Japan (Hirose et al., 1999;

Ozawa et al., 2001) and in Cascadia (Dragert et al., 2001) and reviewed by Schwartz and Rokosky (2007).

Interactions between seismic and aseismic slip also occur before a rupture. Laboratory experiments evidenced a nucleation phase before rupture (Dietrich, 1992; Ohnaka, 2003; Thompson et al., 2009; McLaskey and Kilgore, 2013; Latour et al., 2013; McLaskey and Lockner, 2014; Passelègue et al., 2014; Scuderi et al., 2016).

The first study of such a preparatory phase on subduction zones were made in the 1970s and 1980s after the great Chilean earthquake of May 22, 1960 (Kanamori and Cipar, 1974). The authors evidenced a low-frequency signal about 15 minutes before the main shock. This observation was later confirmed by the analysis of the amplitude and phase spectra of signals recorded at eight stations and by fitting them with the Haskell model (Cifuentes and Silver, 1989). Another observation of a potential precursory phase was made before the Japan Sea earthquake M7.7 that occurred on May 26, 1983. Linde et al. (1988) analyzed the data of three borehole strain meters and evidenced the occurrence of transient strain events that they believe to be aseismic, a few months before the main shock. These transients stop only a few days after the earthquake. More recently, repetitive seismic signals occurred a few minutes and a few seconds before the 1999 Izmit earthquake, in Turkey (Bouchon et al., 2011). This can suggest either the setting of an aseismic slip in the area that surrounds the asperity and that rapidly reloads it or a stress-transfer driven cascade as observed by Ellsworth et al. (2016).

The existence of a slow slip prior the Tohoku-oki earthquake (Kato et al., 2012) as well as multiple foreshocks and slow-slip events before the Mw8.1 Iquique earthquake that occurred in Chile, in 2014 was evidenced by studying geodetic data (Ruiz et al., 2014) and REs in the main shock areas (Kato and Nakagawa, 2014). Also, the Papanoa earthquake that occurred on April 2014, in Mexico was clearly triggered by a slow slip episode observed with GPS data (Radiguet et al., 2016).

The interactions between seismic and aseismic slip can be modeled by the rate-and-state law that we define in the next section.

1.2   Rate-and-State Friction Law : asperities and barriers.

Earthquakes are fast slips that can be seen as frictional instabilities that spontaneously release elastic energy accumulated in the surrounding medium due to slow and constant tectonic deformation. The frictional strength is thus a fundamental parameter that controls the occurrence of such rapid slips. Laboratory experiments conducted in the 1970s by Dieterich (1972; 1978; 1979; 1979) who studied friction on granite samples resulted in the formulation of the « rate-and-state » friction law in the 1980s by Rice and Ruina (Ruina, 1983; Rice, 1983). In these experiments, Dieterich observed the behavior of the friction coefficients of a spring-and-slider system which is the simplest mechanical model for earthquakes. The friction characterizing the contact between the slider and the support is defined with two coefficients : the static friction coefficient, μ_s (at rest) and the dynamic friction coefficient, μ_d (during rupture). Static friction coefficient must be exceeded for slip to begin. Slip is then resisted by the dynamic friction coefficient.

In the experiments, Dieterich observed 1) that μ_s increases logarithmically with hold time (Dietrich (1972), figure 1.1a) and 2) in response to an increase (or decrease) of the sliding velocity, the frictional strength first rapidly increases (or decreases) before reaching a new frictionnal level characterized by a new constant sliding velocity (Dietrich (1978); Dieterich (1979); Dietrich (1979), figure 1.1b). This instantaneous variation in friction coefficient is called the direct effect and scales as the logarithm of the velocity change. Furthermore, it takes the sliding block a characteristic slip distance Dc to relax towards the steady-state.

Following these experimental results, Dieterich (1979) ; Ruina, (1983) and Rice, (1983) concluded that the friction coefficient μ depends on slip rate v and a state variable θ that characterizes the age of the microscopic contacts on the rough interface :

$$\tau_f = \sigma\mu(v,\theta) = \sigma\left[\mu_0 + a\ln\frac{v}{v_0} + b\ln\frac{v_0\theta}{D_c}\right] \qquad (1.1)$$

Where σ is the normal stress, μ_0 is a reference friction coefficient, a and b are non dimensional parameters and v_0 is a normalizing constant.

The state variable evolves with time or during sliding to continuously renew the population of contacts. Thus, a state evolution law, called 'aging-law' was defined as :
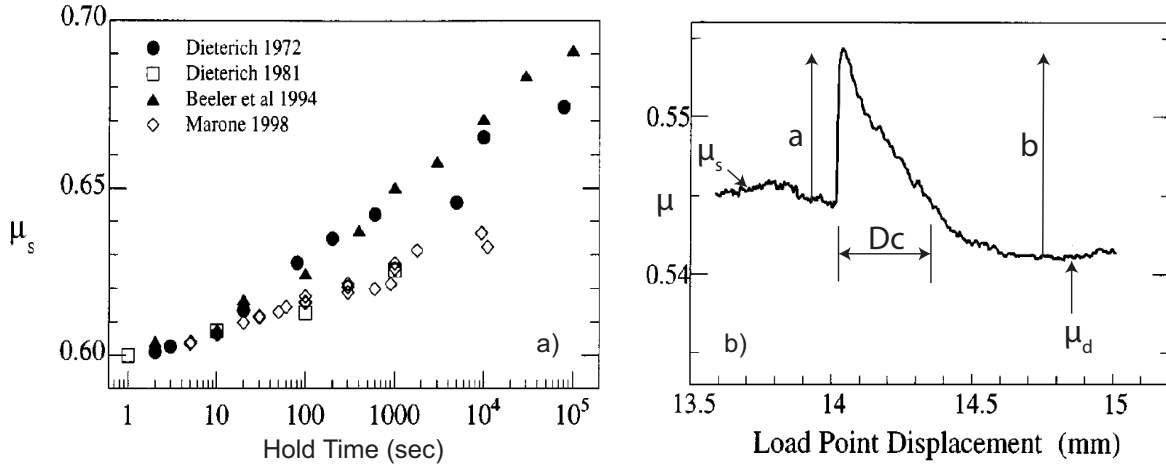
FIGURE 1.1 – a) Relative variation in static friction on a rock interface as a function of the hold time. Experiments were conducted on bare rock surfaces (black symbols) and on granular fault gouges (open symbols), from Marone (1998). b) Friction coefficient evolution with time during a change in loading velocity : the direct effect is clearly visible and parameters a and b and the caracteristic distance Dc are well defined, from Marone (1998).

$$\dot{\theta} = 1 - \frac{v\theta}{D_c} \tag{1.2}$$

Another relationship that characterizes θ was proposed by Ruina, (Ruina, 1983), named the 'slip-law' :

$$\dot{\theta} = -\frac{v\theta}{D_c} \ln \frac{v\theta}{D_c} \tag{1.3}$$

When considering the steady-state sliding case, $\dot{\theta}$ vanishes and the two different evolution law lead to a constant value of θ noted $\theta_{ss}(v) = Dc/v$. From equation 1.1, the corresponding steady-state frictional stress τ_f^{ss} is thus given by :

$$\tau_f = \sigma\mu(v, \theta) = \sigma \left[\mu_0 + (a - b) \ln \frac{v}{v_0} \right] \tag{1.4}$$

The steady-state definition of the rate-and-state law is fundamental to describe the mechanics involved in seismic and aseismic slip. Steady state friction presents two behaviors depending on the sign of $(a - b)$ parameter that characterizes different stabilities

properties. If $(a - b) < 0$, there is velocity weakening, slip instabilities can develop leading to a rupture or a seismic slip. On the contrary, if $(a - b) > 0$, velocity strengthening occurs meaning that the system is unconditionnally stable, no rupture can nucleate in this field. The slip present is called 'aseismic'.

Medium presenting velocity weakening are called asperities, whereas medium presenting velocity strengthening are barriers, or anti-asperities.

The subduction zone was schematized by Schwartz and Rokosky as a succession of frictional property changes according to depth (Schwartz and Rokosky, 2007). However, the Sumatra earthquake of 2004 followed by the Tohoku earthquake in 2011 illustrated that the updip zone must not be considered as stable anymore.

1.3   Interactions between seismic and aseismic slip.

In this section, we present the interactions between seismic and aseismic slip at the asperity scale. We also define the Repeating Earthquakes (REs) and how they can be used as a proxy for the aseismic slip.

1.3.1   Interactions at the scale of an asperity.

A fault zone can be considered as a complex medium presenting a heterogeneous distribution of the rate-and-state steady-state friction parameter $(a - b)$ as shown in fig 1.2a. Following Scholz (1990), Pacheco et al. (1993) illustrated a subduction zone with the presence of three different units : stable, conditionally stable , or unstable. Stable fields are velocity-strengthening and are characterized by a steady slip and no strain accumulation. They are said to be 'uncoupled', that is, the two plates can slip freely. This displacement can be viewed as a moving walkway that slips freely and without emitting elastic waves, thus, it slips aseismically. The unstable areas have a friction behavior opposite to the stable zones. They are velocity-weakening and are totally locked. They are said to be 'coupled', meaning that the plates have numerous areas in contact. They can be viewed as glue dots that break during slip episodes and remain locked between them. The third unit corresponds to the conditionally stable fields and slips steadily between two ruptures of the asperities that they surround. They can however slip faster during a rapid release of stress during the rupture of a nearby asperity.

The aseismic slip occuring in the stable areas, loads the asperities that are present in the medium. This load can be seen as stable in time and corresponds to the interseismic period in the seismic cycle of the asperity, which is the longest phase in the cycle (figure 1.2b). The strain on the asperity increases steadily. Then, the slip accelerates, this is the nucleation phase. At a certain threshold, the loading is too important to still be supported by the asperity which ruptures, emitting elastic waves that can be recorded at surface (figure 1.2b). This corresponds to the coseismic slip. Another consequence is a change of stress state in the surrounding medium which leads to an acceleration of slip which might break other close by asperities. Once the rupture is finished, the slip around the asperity progressively slows down. This corresponds to the postseismic phase. With time, the contacts that broke during the coseismic slip will heal, this will slowly increase the coupling between the two sides of the fault plane.

This simplified description of the interactions between stable and unstable zones during the seismic cycle was made more complex with the work of Chen and Lapusta (2009) who modelized that during the interseismic phase, the slip in the stable field penetrates the asperity allowing it to release a part of the accumulated strain aseismically. During their simulations, a significant amount of slip on the velocity-weakening patches is accumulated aseismically (even if the patches also rupture seismically) ranging from 99% to 20% of total slip according to the simulated moment magnitude (from 0.3 to 3.7). On the contrary, the rupture of the asperity leads to an increase of slip rate and postseismic slip in the aseismic medium (Kato, 2003; Chen and Lapusta, 2009).

1.3.2 Repeating Earthquakes used as aseismic slip proxys.

An asperity has its own finger prints : its seismic signal emitted during rupture. Every time it breaks during the seismic cycle, it will emit the same seismic signal (cf. fig 1.2b). This signal corresponds to the combination of three effects : the source + the propagation path + the instrumental effects of the stations. Thus, by simply comparing the recorded signals it is possible to define groups of Repeating Earthquakes (REs). As we already mentionned, the REs can be due to the loading of the surrounding aseismic slip. This is a strong hypothesis that allows to use REs as proxys to assess the evolution of the surrounding medium : if the asperity breaks periodically, the aseismic slip rate is constant and stable (fig. 1.3). An increase in time of occurence of REs indicates an increase of aseismic slip and inversly. Thus, by following the temporal evolution of this particular type of earthquakes, it is possible to detect transient slip events.
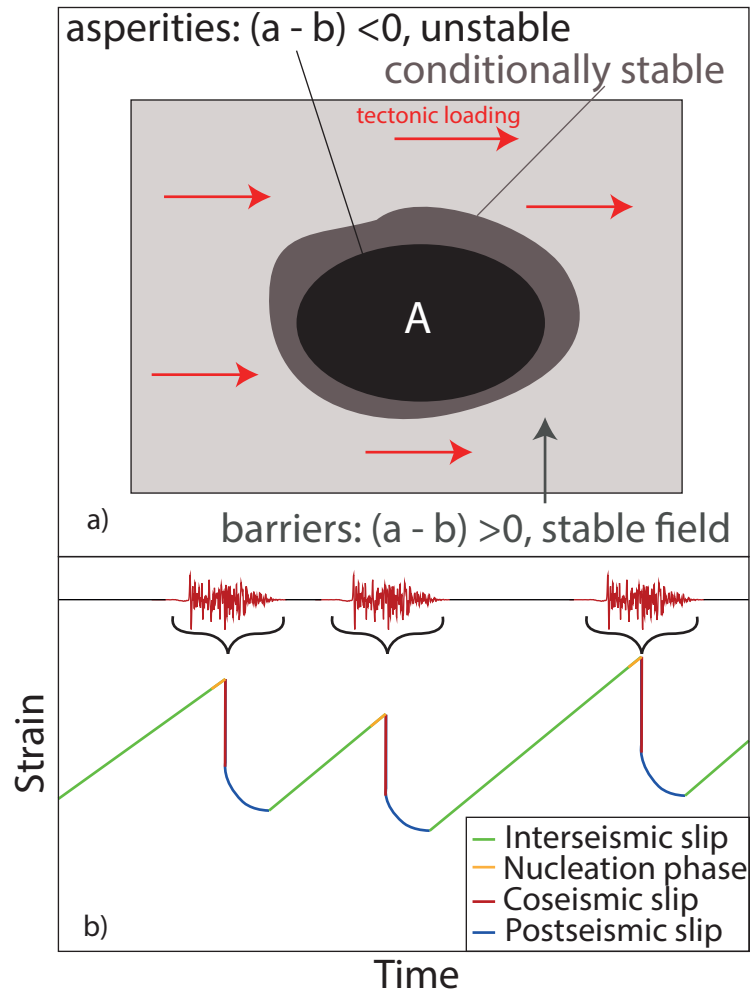
FIGURE 1.2 – a) Schematic diagram of a fault plane. Tectonig loading is shown with the red arrows. The rate-and-state steady-state friction parameter $(a - b)$ is heterogeneous on the fault : seismic asperities are velocity weakening patches for which $(a - b) < 0$ whereas the aseismic medium, called barrier or anti-asperity, corresponds to a velocity strengthening field $(a - b) > 0$. Conditionally stable zones are also present (see text). b) Bottom : Evolution of the strain underwent by the asperity A with time characterizing the seismic cycle of the asperity. Four stages are shown : interseismic slip, a nucleation phase, co- and post-seismic slip. Top : seismic signals of the elastic waves emitted by the asperity during its multiple ruptures.

As mentionned in the introduction, REs have been first studied in California, within the creeping (or aseismically slipping) section of the San Andreas fault (Nadeau et al.,
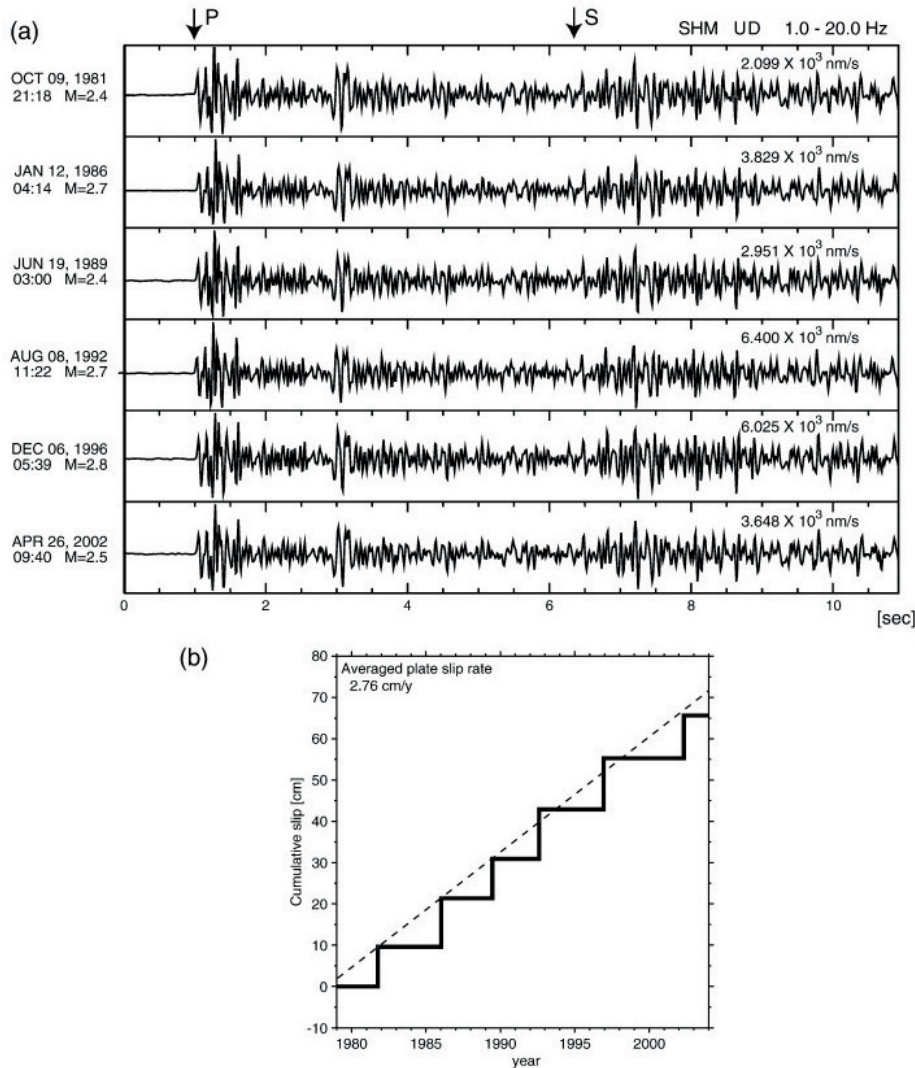
FIGURE 1.3 – a) Normalized waveforms of REs studied beneath Kanto area, in Japan, on the Philippine Sea plate. b) Cumulative slip of the RE group of (a). The line corresponds to the best fit by the least squares method, from (Kimura et al., 2006).

1995; Nadeau and Johnson, 1998). This discovery excited the seismologists : an evidence of the characteristic earthquake cycle had been found. REs have been then used to assess the evolution of stress with time in Parkfield (Lengliné and Marsan, 2009) but also along the North Hayward fault (Bürgmann et al., 2000). They were also studied on subduction fault zones, especially in Japan : off Sanriku (Uchida et al., 2003), to assess interplate coupling in the NE Japan (Igarashi et al., 2003; Matsuzawa et al., 2004; Uchida et al., 2009) or to define the subdution plate configuration (Kimura et al., 2006).

In Parkfield REs mainly present a periodic behavior which lead Nadeau and Johnson (1998) to estimate the cumulative slip recorded by the asperity establishing the relationship between the amount of slip d (m) and the seismic moment M_o (N.m), defined by equation 4.1 :

$$log(d) = -1.04 + 0.17log(M_o) \qquad (1.5)$$

Kimura et al., (2006) used this relationship to estimate the cumulative slip in the asperity given in figure 1.3. They obtain more than 12 cm of slip for a M2.7 event which is only possible if the asperity also slips aseismically.

Chen and Lapusta (2009) modelized the REs as frictional instabilities on a fault in an elastic medium. They acounted for inertial effects due to seismic events and used the Rate-and-State law described above. They found that aseismic slip must be present at the asperity to explain the high stress drops considered.
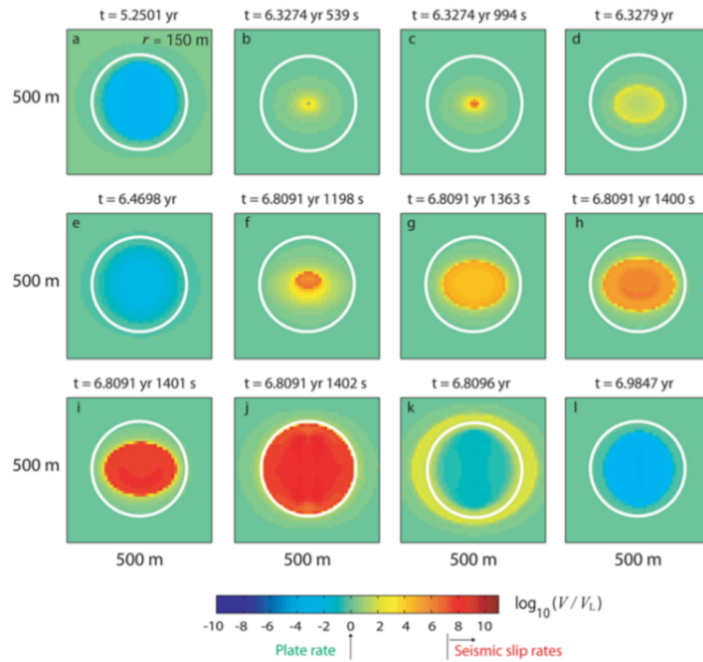
FIGURE 1.4 – Snapshots of slip velocity distribution for one earthquake cycle and a radius of 150m corresponding to Mw=2.9. Seismic slip is red while aseismic slip is blue. Postseismic creep is seen to be induced by the coseismic slip, in interaction with the surrounding rate-strengthening zone, from Chen and Lapusta (2009).

Chen and Lapusta (2009) also found that to obtain the values of recurrence times oberved at Parkfield, they needed a smaller slip rate than usually used in previous stu-

dies (4.5mm/yr instead of 23mm/yr). Furthermore they found that the ratio of seismic moment Mo to the total seismic moment (i.e aseismic plus seismic moments) varies from 0.001 to 0.8 for a radius range of 88m (Mw=0.9) to 350m (Mw=3.7). This ratio can be seen as the ratio between coseismic slip and total slip (including post-seismic creep) on the asperity.

The slip behavior of an asperity is thus mainly aseismic and the used of Nadeau and Johnson relationship (1998) might not be suited for REs in Kanto area.

1.4   Conclusion

Interactions between seismic and aseismic slip was evidenced theoretically as well as experimentally but are not fully understood. The aim of this study is to search for episodes of transient deformation by using REs and by detecting resembling earthquakes. This will bring new insights on how aseismic deformation can -or not- accelerate the occurrence of strong earthquakes, and on what conditions. The very high density of the Japanese monitoring geodetic and seismic networks allows the detection of events with low intesity and/or size. However, the use of geodetic data is made difficult in some areas because they are 1) far from the coast (as it is the case for the Tohoku rupture zone) 2) above the double subduction zone (as in Boso and Kanto area). We thus focus our study in these three zones applying different detection techniques on the seismic data.

Chapitre 2

The Japanese Subduction Zones.

In this chapter, we introduce the tectonic context of Japan, the different type of slips that can be found on the Japanese subduction zones. The second part of this chapter is dedicated to the presentation of the areas studied in this manuscript.

2.1 Tectonic context.

The tectonic context of Japan is highly complex wich made it one of the richest area in the world to study earthquakes. Two plates subducts beneath the North American plate (NA) : the Pacific plate which is dense and cold (PAC) and the Philippine Sea plate that is light and young (PHS), figure 2.1.

PAC subducts at the north-east of the main island, Honshu. It dives to the west with a velocity of around 80 mm/yr along the Japan and the Izu-Bonin trenches. PHS subducts from the south-east to the north-west, south of Honshu. It is slower than PAC with a velocity of 34 mm/yr at the Sagami Trough where it plunges above PAC, and with a velocity of 56 mm/yr along the Nankai Trough. Thus, there is a triple junction point off-coast of the Boso Peninsula, close to the megapole of Tokyo.

Volcanism is associated with the subduction zones : 110 active volcanoes were listed by the Japanese Meteorological Agency (JMA, figure 2.2). This intense volcanic activity can interact with earthquakes (Eggert and Walter, 2009; Donne et al., 2010; Aizawa et al., 2016). More recently, the Mw7.1 Kumamoto earthquake offered a rare opportunity to study such interactions. The event occurred on 16 April 2016 around 30 km southwest of Aso caldera, one of the largest volcanoes in the world. Four M$\geq$5 forshocks preceded
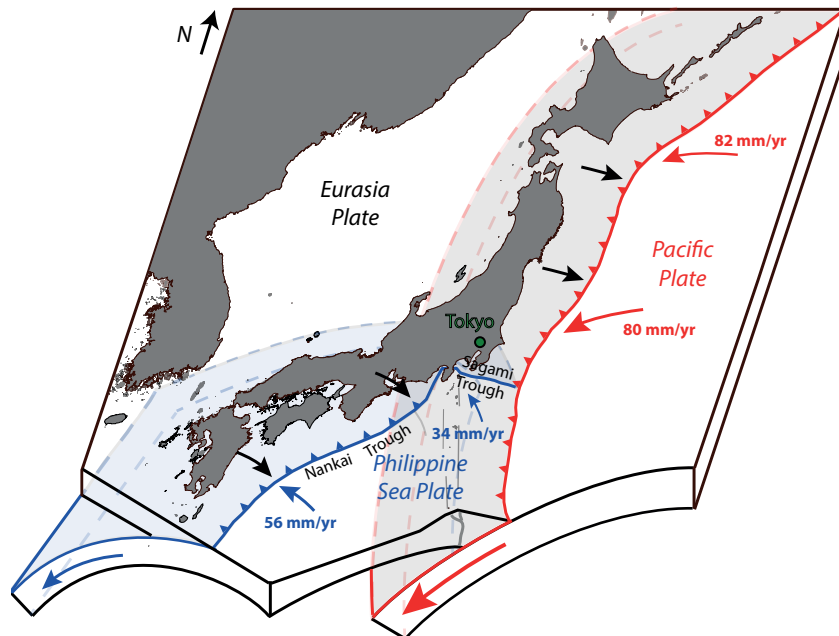
FIGURE 2.1 – Subduction zones in Japan. Both subductions of PAC and PHS are shown. Note that the triple junction point is located off-coast Boso Peninsula, close to Tokyo (modified from Reverso (2015)).

the earthquake including a Mw6.2 event (Kato et al., 2016). Because of the presence of magma beneath the Aso volcanic complex, the coseismic rupture stopped at that point (Lin et al., 2016; Yagi et al., 2016).

Crustal seismicity is not always linked to volcanic activity but mainly comes from the relaxation of the internal deformation of tectonic plates. Crustal events occur at shallow depths (10-30 km) and can thus be highly devastating due to the proximity of areas vulnerable to strong ground motion. We can list as examples of such damaging events the 1891 Nobi earthquake of Mj 8.0 (JMA magnitude), the 1948 Fukui earthquake (Mj 7.1), the 1995 Southern Hyogo Prefecture (Kobe) earthquake (Mj 7.3), and the 2004 mid-Niigata Prefecture earthquake (Mj 6.8).
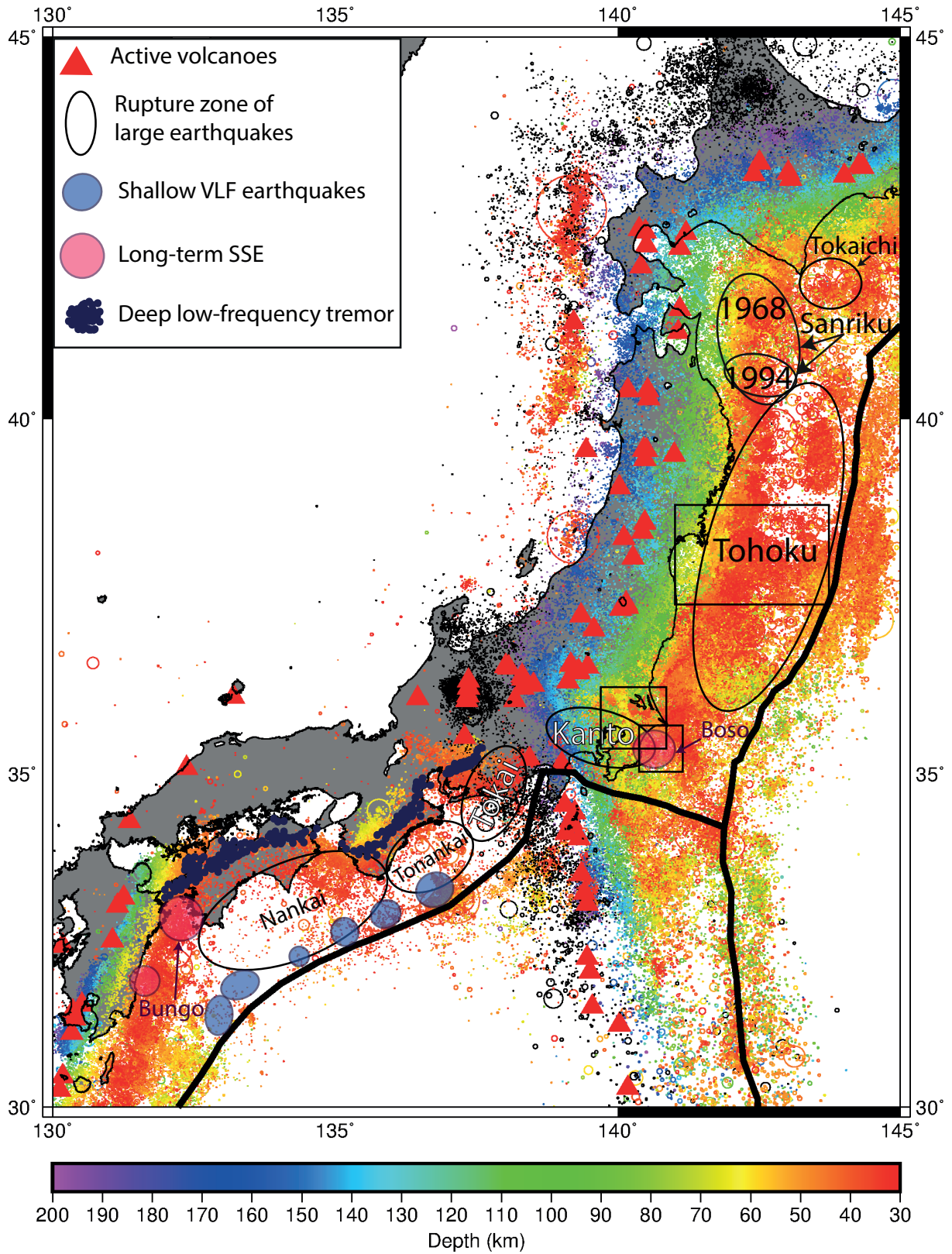
FIGURE 2.2 – Tectonic setting of the Japanese subduction zones. Plate limits are indicated by thick black lines. Active volcanoes are located with red triangles. All M≥5 earthquakes from 1923 to 2015 with a depth between 30 and 300 km are color coded according to their depth. The area of rupture of major earthquakes are indicated with black ellispoids and their names are given. Black rectangles indicate the areas studied in this manuscript. Several types of slips are found in the southwestern Japan : SSEs (pink circles), VLF (blue circles) and deep low-frequency tremors (dark blue dots).

However, the main source of seismic activity in Japan is the double subduction zone that hosts thousands of earthquakes every year ranging from a few kilometers to hundreds kilometers depth (figure 2.2). Three main ruptures occurred along the Nankai-Sagami Trough in the past century : the Nankai (1946, Mw 8.3), the Tonankai (1944, Mw 8.1) events and one of the most traumatic earthquake in Japan history, the Kanto earthquake (M 7.9), in 1923. Several historical earthquakes struck the northeastern part of Japan, on PAC. Most recent events include the 1994 Mw 7.6 Sanriku earthquake, the 2003 Mw 8.1 Tokaichi earthquake and, the main one, the 2011 Mw 9.0 Tohoku-Oki earthquake that we further describe in section 3.3.1.

2.2   Slips on the Japanese Subduction Zones.

The Japanese Subduction Zones are complex and offers the possibility to study a wide range of slip behaviors. Indeed, the deployment of geodetic and seismic networks as GEONET and Hi-net in Japan has contributed to the discovery of other types of earthquakes than the one presented above. There exist slow earthquakes that show a transitionnal slip from stable to unstable slips.

The ideal area to present the interaction between slow and fast slip is southwest Japan (figure 2.2). Two types of slow earthquakes can be found along the downdip edge of the seismogenic zone : 1) geodetic slow earthquakes that are Slow Slip Events (SSEs, in pink in figure 2.2) that can be short- (few days to few weeks) or long-term (months to years), both types can be found in Bungo channel area (Hirose et al., 1999; Ozawa et al., 2004; Hirose and Obara, 2005), interacting with each other (Hirose and Obara, 2005) and 2) seismic slow slip events : very-low frequency earthquakes (VLF) that have a dominant period of tens of seconds. Tremor episodes accompany both short-term SSEs and VLFs. They are located along a belt of around 30 * 600 km^2 (Obara (2002); Obara et al. (2004); Ito et al. (2007), blue in 2.2). These episodes are called ETS : Episodic Tremor and Slip and were first discovered in Cascadia (Rogers and Dragert, 2003). They present recurrent activity and usually break one fault segment at a time (although the 2006 Kii and Tokai SSE propagated over a gap, Ito et al. (2007)).

Long-term SSE episodes of 2003 and 2010 in Bungo channel have almost identical moment magnitudes, slip areas and durations (Ozawa et al., 2013). This characteristic behavior is also observed for the Boso SSEs. The magnitude (from 6.4 to 6.6) and the rupture breaks the same characteristic patch (Ozawa et al., 2003; Sagiya, 2004; Hirose

et al., 2012, 2014). The SSEs on Boso Peninsula have always been accompanied by swarm-like seismicity located at the northern downdip edge of the slow slip patch (Ozawa et al., 2007; Hirose et al., 2012), triggered by the stress released during the SSEs (Hirose et al., 2014).

VLFs associated with short-term SSEs can be found along the Ryukyu trench, southwestern Japan (Nishimura, 2014; Nakamura and Sunagawa, 2015; Yamashita et al., 2015). They can also be excited by regular earthquakes as it was the case during the Mw7.5 Kii peninsula event and its Mw7.2 foreschock (Obara and Ito, 2005). VLFs located in the accretionary prisms present a stress drop 0.1% of an ordinary earthquake (Ito and Obara, 2006). Furthermore, the authors evidenced that the fault radius of a VLF is 10 times greater than the one of a regular earthquake and that the rupture and slip velocity were slower than those of an ordinary earthquake. This suggests that the asperity that breaks during a VLF is rather soft and slow.

In Nankai, the subducting plate hosts all these different types of slip where they all interact together (figure 2.3). Patches of VLF earthquakes are surrounded by aseismic slow slip areas. A slow slip event begins when the shear stress reaches the yield stress of this area. This increases the shear stress in the surrounding area and thus on the patches of VLF earthquakes. These patches eventually rupture resulting in a low stress drop and low velocity rupture. The micro-cracks also present in the area might rupture due to the migration of the SSE. These cracks have smaller source sizes and weaker shear strength than VLF earthquakes and generate deep low-frequency tremors. In turn, the SSE can load the upper part of the subduction zone leading to its rupture.

Unlike the Nankai zone, PAC presents few SSEs, VLFs and tremors. However, some events were detected, especially off-Tohoku. Two slow slip events occurred in the area of the maximum coseismic slip of Tohoku-oki earthquake in 2008 and just before the mega-thrust event (Ito et al., 2013). Anomalous tremors were also detected in this zone (Ito et al., 2015). Eventually, VLFs were found in the off-Tohoku region, mainly north and south of the rupture zone but also in the central part of the rupture (Matsuzawa et al., 2015). The number of all the slow earthquakes observed is much smaller than that in Nankai. Furthermore, the presence of such events close to regular earthquakes zones and within the slip region of Tohoku-Oki earthquake is different than the spatial distribution of events in Nankai zone.

The different behaviors between the two subduction zones implies that the frictional properties of the plates are different. This might be due to the fact that PAC dives
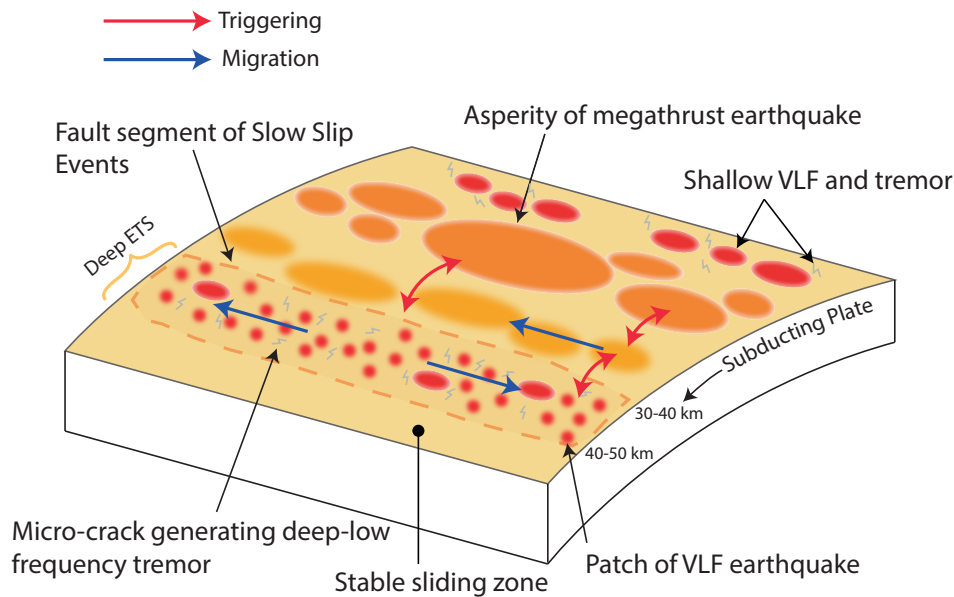
FIGURE 2.3 – Schematic view of the subduction zone in Nankai showing the location and interactions between the different types of slip (red arrows). The rupture of a megathrust earthquake is characterized by a fast slip (orange ellipsoid). They interact with slow slips that consist of long-term SSEs (yellow ellipsoids) and the deep ETS zone (delimitated by an orange dashed line). When the SSE occurs in the deep ETS zone, it can migrate and thus activate the patches of VLF earthquake and also rupture the micro-cracks that generates deep-low frequency tremors (modified from Ito at al., (2007) and Obara and Kato, (2016)).

twice faster than PHS. It also dives deeper impacting on the geothermal gradient (80 K/km and 35 K/km on average for PAC and PHS respectively, (Tanaka et al., 2004)) and on the presence of fluids in the interface. The fluid pressure being an important factor in controlling the conditionnaly stable sliding fields where slow earthquakes occur it it thus not surprising to observe less slow earthquakes in PAC than in Nankai area. Furthermore, the observation of VLFs, slow slip events, REs and large earthquakes in the same area suggests that the frictional properties in the subduction interface are highly heterogeneous.

2.3 Studied areas.

In this manuscript, we focus on three areas : Kanto, Boso and the Tohoku rupture zone. These are ideal places to study the link between seismic and aseismic slip since they host REs (Kimura et al., 2006; Kato et al., 2012), SSEs (Ozawa et al., 2003; Sagiya, 2004; Hirose et al., 2012, 2014) and a mega-thrust earthquake. In this section, we present all three areas and their characteristics.

2.3.1 The Tohoku rupture zone.

On March 2011, the 11th, a Mw9.0 megathrust earthquake struck the Japan trench offshore Northern Honshu (Ozawa et al., 2011). It strucked one of the best monitored zone in the world, where historical earthquakes occurred in the past (Tsumura, 2005). The rupture area was approximately 500 km long and 200 km wide. It was the first Mw9.0 event to be recorded by a dense network of continuous and broad-frequency-range seismic stations. The dense seismic network along with geophysical investigations allowed to constrain the geometry of the subduction zone. Furthermore, surface deformation was also well studied using the GEONET (geodetic Global Positioning System network, Sagiya et al. (2000)). The decadal monitoring of geodetic strain helped to characterize the inter-seismic deformation (Suwa et al., 2006; Hashimoto et al., 2009; Loveless and Meade, 2011). Furthermore, the down-dip part of the rupture area underwent a long-term slip acceleration seen by GPS data (Ozawa et al. (2011) (black lines in figure 2.4), Mavrommatis et al. (2014); Yokota and Koketsu (2015)).

The Tohoku earthquake was surprising in many aspects : 1) the maximum forecast magnitude for this area was 8.2 (Earthquake Research Committee), 2) for the second time in earthquake history (the first time was for the Sumatra earthquake in 2004, Chlieh et al. (2007)), large co-seismic slip was evidenced close to the trench (Ide et al., 2011), a zone that was classicaly thought as stable. This produced a large tsunami wave responsible for at least 20,000 deaths and that triggered a nuclear disaster, 3) high frequency radiations were found at the deeper part of the rupture zone whereas the shallow part weakly radiated at high frequencies (Ide et al., 2011; Lay et al., 2012).

Several inversions of geodetic measurements were made to estimate the co- and post-seismic of the megathrust earthquake (Ozawa et al., 2011; Simons et al., 2011). Sea floor measurements were aquired both before (Matsumoto et al., 2008) and after the Tohoku earthquake (Kido et al., 2011; Iinuma et al., 2012) and were used to estimate pre-, co-

and post-seismic slip jointly, indicating that the postseismic slip might be located on the same area than the coseismic slip (Perfettini and Avouac (2014), figure 2.4).
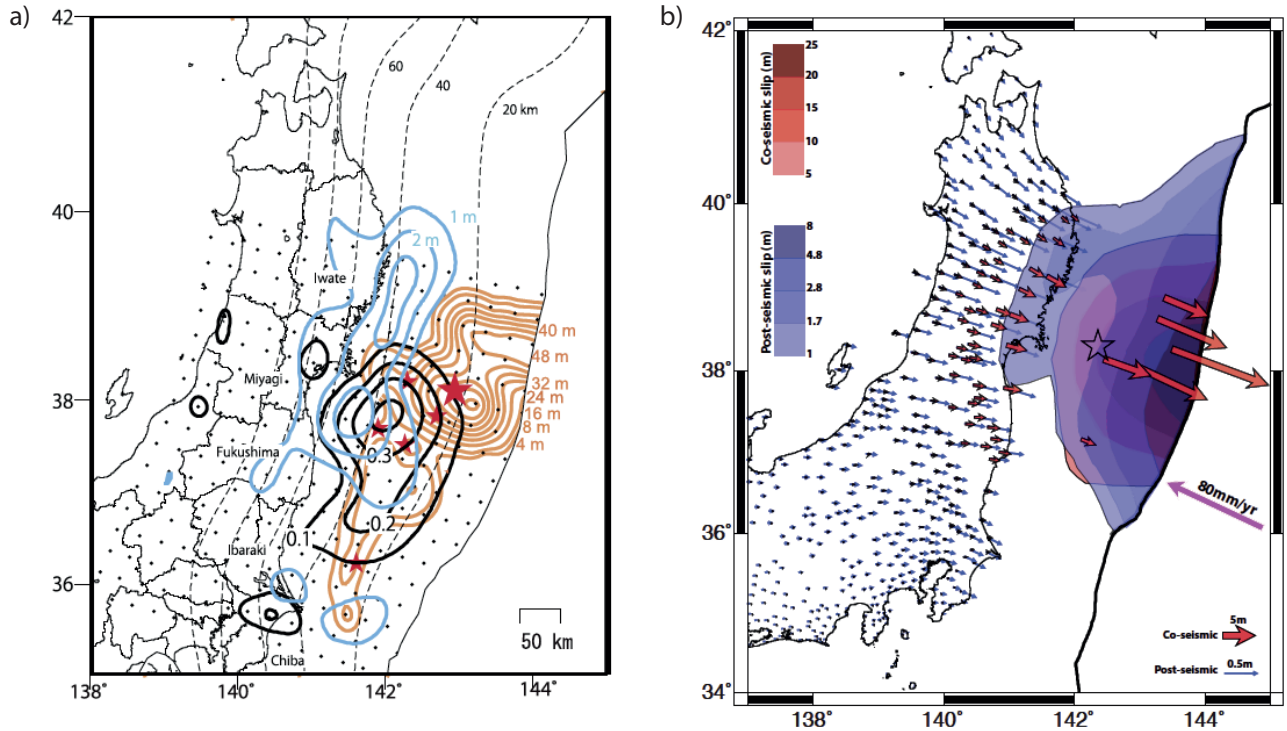

FIGURE 2.4 – a) Preceding aseismic slip (black contours with an interval of 0.1 m), coseismic slip of the Tohoku earthquake (red contours with an interval of 8 m), and afterslip of the Tohoku earthquake (blue contours with an interval of 1 m), estimated with inland GPS stations. Small stars indicate the epicenters of the five Mw > 6.5 subduction earthquakes that occurred between 2003 and 2011. The large star shows the epicenter of the Tohoku earthquake, from Ozawa et al. (2011). b) Co-(red) and post-seismic (blue) slip distribution of the Tohoku-Oki earthquake. The authors used inland GPS stations and campaign measurements of 6 sea floor displacements. Red vectors represent the measured co-seismic displacement vectors at the GEONET GPS stations and the blue vectors represent post-seismic displacements over 279 days following the Tohoku-Oki earthquake. The six near trench stations include coseismic slip and 21 days of post-seismic slip. Star shows main-schocks epicenter (Wei et al., 2012), from Perfettini and Avouac (2014).

There was a preseismic phase that started on mid-January coincidently with the activation of deep seismicity (Bouchon et al. (2016), figure 2.5). The preseismic phase went on as a burstlike seismicity in mid-February that lasted around 23 days (Hirose et al., 2011). Two days before the mainshock, a Mw7.3 foreshock struck close to the initation point of the Tohoku earthquake. The seismicity between the biggest foreshock

and the mainshock contains several M≥6 earthquakes and appeared to migrate towards the mainshock epicenter, indicating the presence of afterslip (Ando and Imanishi, 2011) and/or interaction mechanisms between earthquakes (Marsan and Enescu, 2012). Two disctinct sequences of slow-slip transients propagating towards the initiation point was evidenced by the use of REs (Kato et al., 2012).
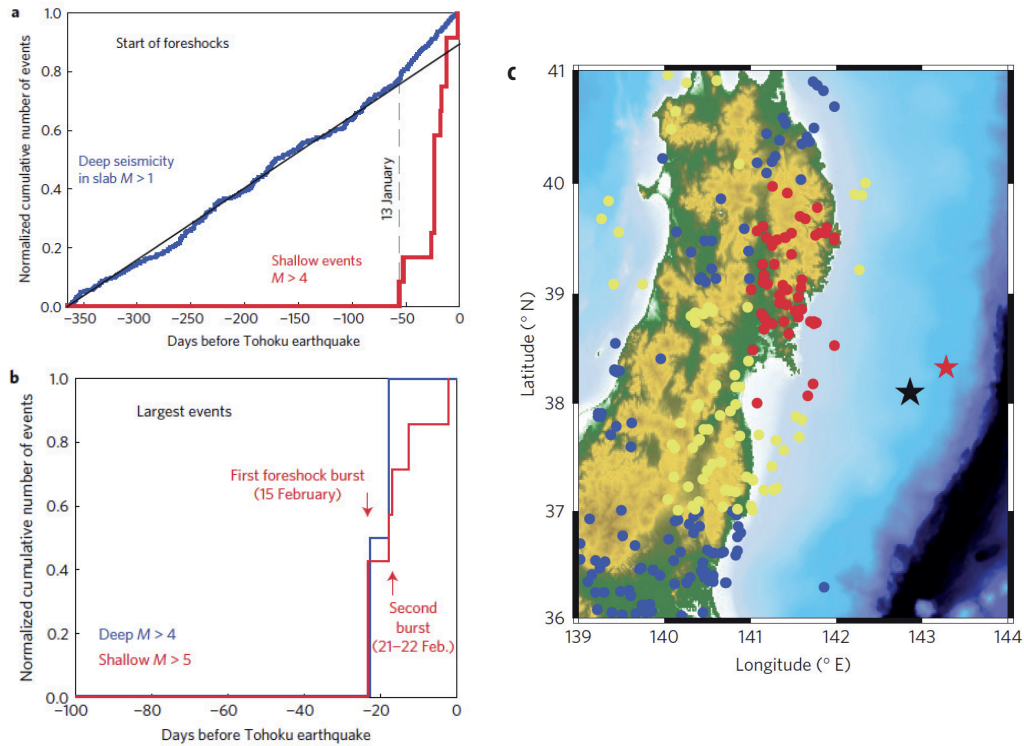

FIGURE 2.5 – a) Time evolution of shallow (≤40 km) foreshocks and deep (≥80 km) seismicity before the earthquake. Events after the Mw 7.3 foreshock of 9 March are not included. The black line is the least-square fit before the foreshocks start on 13 January. b) Timing of the largest deep and shallow events occurring in the 100 days before the earthquake. c) Events M>1 deeper than 80 km. The area is divided into zones of 1°*1° in latitude/longitude and events are coloured according to the activity increase in their zone, measured relatively to the activity rate in the preceding year : blue (decrease), yellow (0–50% increase), red (50–100% increase), black (>100% increase). Stars show the earthquake (black) and Mw 7.3 foreshock (red) epicentres, from (Bouchon et al., 2016).

The presence of one of the densest network in the world close to the rupture area is a real opportunity to obtain a fine image of the preseismic phase. The approach that we present in the manuscript uses the seismic stations as a dense receiver network. This method has been first used in underwater acoustics (Bienvenu and Kopp, 1983)

and geophysics (Samson, 1983; Glangeaud and Latombe, 1986). More recently, it was used to locate sources of hydrothermal activities using seismic noise (Legaz et al., 2009; Vandemeulebrouck et al., 2010; Cros et al., 2011) and noise source location (Corciulo et al., 2012; Chmiel et al., 2016). The method is based on phase matching between continuous data and templates allowing to detect events that ressemble templates even with a low signal-to-noise ratio.The analysis confirms the two seismic bursts on 2011/2/16 and 2011/2/26 evidenced by Kato et al., (2012) but also shows that the seismic crisis has actually started on November 2010 and that the seismic rate accelerated until the 8th of March when a quiescence is observed. The seismic migration is also evidenced by the study of events detected at low frequency (1-8Hz). The analysis of high frequency detections (14-20Hz) revealed highly active areas that strongly reacted to the M7.3 foreshock since M4.8 to M6 earthquakes occurred there.

2.3.2 Boso area.

As previously mentionned, Boso area is well known for the occurrence of several slow slip events (SSE) along the top interface of PHS at shallow depth (between 10 and 30 km), in 1983, 1990, 1996, 2002, 2007, October 2011 and 2014 that have a clear signature on geodetic measurements and have a moment magnitude between 6.4 and 6.6 and rupture the same characteristic patch (Ozawa et al., 2003; Sagiya, 2004; Hirose et al., 2012, 2014). The SSEs on Boso Peninsula have always been accompanied by swarm-like seismicity located at the northern downdip edge of the slow slip patch (Ozawa et al. (2007); Hirose et al. (2012), figure 2.6), triggered by the stress produced during the SSEs (Hirose et al., 2014).

A first estimation of the recurrence interval of these transients was 4 to 7 years since 1983 (Hirose et al., 2012). However, the recurrence interval tends to decrease from 6.4 to 2.2 years from 1996 to 2014 (Ozawa, 2014). This shortening being possibly a by-product of a long-term acceleration in loading rate (Reverso et al., 2016). Furthermore, Boso area is located at the southern end of the Tohoku-oki rupture and was sensitive to stress perturbation caused by the megathrust earthquake since a SSE occurred only three days (Kato et al., 2014) and few months after it (Hirose et al., 2012).

It is necessary to better constrain the slip history of this area since modelizations show that the recurrence intervals become shorter when closer to a large interplate earthquake nearby (Matsuzawa et al., 2010; Mitsui, 2015). Are there smaller SSEs in Boso area or are the SSEs really characteristic ? Are the SSEs always triggered because of the
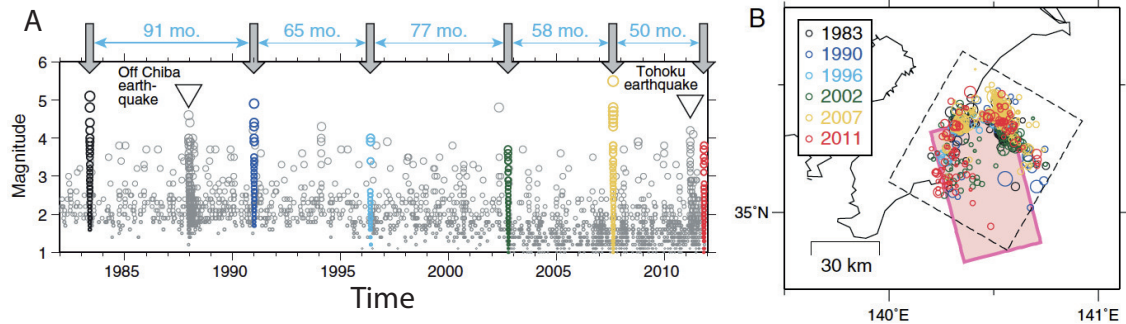
FIGURE 2.6 – a) Seismicity near the Boso Peninsula. The earthquake magnitude versus occurrence time is plotted for the events that have occurred in the dashed rectangle area in B. Gray arrows show the occurrence times of the Boso SSEs and accompanying earthquake swarms. Inverted triangles indicate the occurrence times of the 1987 Off-Chiba and 2011 Tohoku earthquakes. b) Map around the Boso Peninsula showing the epicenters of earthquakes that occurred during the six swarm episodes. Pink rectangle shows the fault area of the 2011 SSE (from Hirose et al., (2012)).

accumulation of a slip deficit with time (Sagiya, 2004; Nishimura et al., 2007; Reverso et al., 2016) ? To answer these fundamental questions we analyse the distributions in time and space of REs. We also analyse GPS data removing seasonal signals, the trend and the common mode. The combination of these observations allows to identify two unknown SSEs that are smaller in magnitude and/or lateral extension than the already known ones.

2.3.3 Kanto area.

Beside its closeness to the triple junction point, the Kanto area presents numerous seismological specificities. Coupling on the PHS-PAC contact area is weak (Uchida and Matsuzawa (2011), figure 2.7). Coupling is also smaller on the PAC interface in this area compared to the northern part of the plate where the M9.0 Tohoku earthquake struck (black ellipsoid 2.2). The difference in coupling is thought to be one of the reasons why the southern limit of the rupture lies just above Kanto.

Furthermore, the area underwent several major earthquakes in the past (Grunewald and Stein, 2006; Nyst et al., 2006). The last one was the Kanto earthquake (M7.9) that
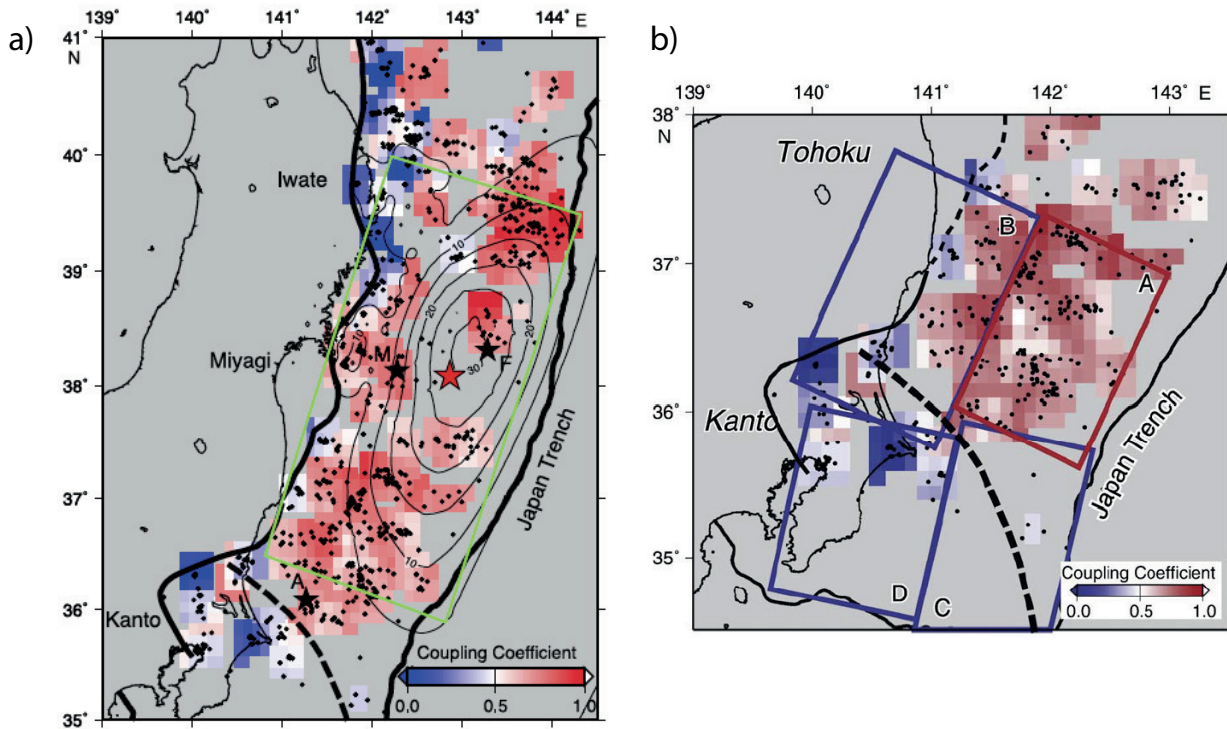
FIGURE 2.7 – a) Interplate coupling coefficient estimated from small repeating earthquakes for the period from 1993 to March 2007 (color). Distribution of small repeating earthquakes (black dots) and coseismic slip area (contours, Iinuma et al. (2011) are also shown in this figure. Bold lines denote the down-dip limit of interplate earthquakes (Igarashi et al., 2001; Uchida et al., 2009) and the trench axis. Dashed bold line denotes northeastern limit of the Philippine Sea plate (Uchida et al., 2009). The averaged coupling coefficient is estimated for every 0.3 degree by 0.3 degree windows that have three or smaller repeating earthquake groups. The red star indicates the hypocenter of the 2011 Tohoku earthquake. Stars marked by M, F and A indicate the hypocenter of the 2005 Miyagi-oki earthquake (M 7.2), the M 7.3 earthquake on March 9, 2011 and the largest aftershock on March 11, 2011 (M 7.7), respectively, from Uchida et al., (2009). b) zoom in Kanto area, from Uchida and Matsuzawa (2011).

struck in 1923 causing the deaths of over 140,000 people (figure 2.2). The main shock consisted of right-lateral slip with a thrust component on a low-angle fault plane in the Sagami trough (Nyst et al., 2006). More recently, one of the main aftershocks of the Tohoku earthquake occurred off-coast of Kanto with a magnitude 7.9. Furthermore, an increase in seismic activity in the Kanto region was observed just after the mainshock (Toda et al., 2011).

An earthquake of magnitude 7 or more would be disastrous on a human and economic

scale since Kanto hosts one of the biggest megapole in the world : Tokyo. It is thus vital to understand the seismotectonics of this region. The complexity of the area and its particular location (southern to the limit of Tohoku rupture) make Kanto a unique chance to further analyze the link between aseismic and seismic slip. To do so, we thoroughly study repeating earthquakes (REs) that are known to happen in this area (Kimura et al., 2006; Uchida et al., 2010). The seismicity of PHS is located between 0 and 50 km depth and overlies PAC events that are found between 0 and 100 km depth. In the past, they were mainly used to define plate boundaries in the Kanto area (Kimura et al., 2006; Uchida et al., 2009). Here, the observation of their time recurrence brings the opportunity to assess the consequences of a megathrust event on aseismic slip off the rupture area.

2.4   Conclusion

This manuscript aims at studying the relationship between seismic and aseismic slip events in the Japanese subduction zone, in three specific areas : Kanto, Boso and the Tohoku rupture zone. The search for episodes of transient deformation is based on the observation of REs behavior and on a new method to detect resembling earthquakes. The next three chapters of the manuscript describes in details the work done on these three areas. In chapter 6, we discuss on the new clues brought by these observations and conclude on what remains to be done.

Chapitre 3

Earthquake detection during the preseismic phase of the great Mw9.0 Tohoku earthquake.

3.1 Foreword

The observation and analysis of a precursory phase to rupture is one of the greatest challenge that we have to adress in seismology : is it actually possible to define such a phase ? Are big earthquakes always preceded by a preparating time ? In the end, it all comes down to one question : is it possible to fully capture the preseismic phase in order to forecast earthquakes ?

Forecasting such desastrous events is often seen as the Holly Grail of the seismologists since it would prevent thousands of deaths and preserve the economy of the most vulnerable countries. However, the path is still long. In this chapter, we focus on the analysis of the preparatory phase of a large earthquake. This preseismic phase includes the end of the intersemic phase and the nucleation phase (figure 3.1). These periods are characterized by a continuous increase in strain that is accompanied by seismicity.

As shown in figure 3.1, a certain noise level can be present in the seismic signals, hiding small events that can characterize the occurrence of transient slips.

Traditionnaly, the technique of cross-correlation between seismic events has been widely used to detect Repeating Earthquakes (Nadeau and McEvilly, 1997; Matsuzawa et al., 2002; Uchida et al., 2003; Kimura et al., 2006). However, this technique is limited
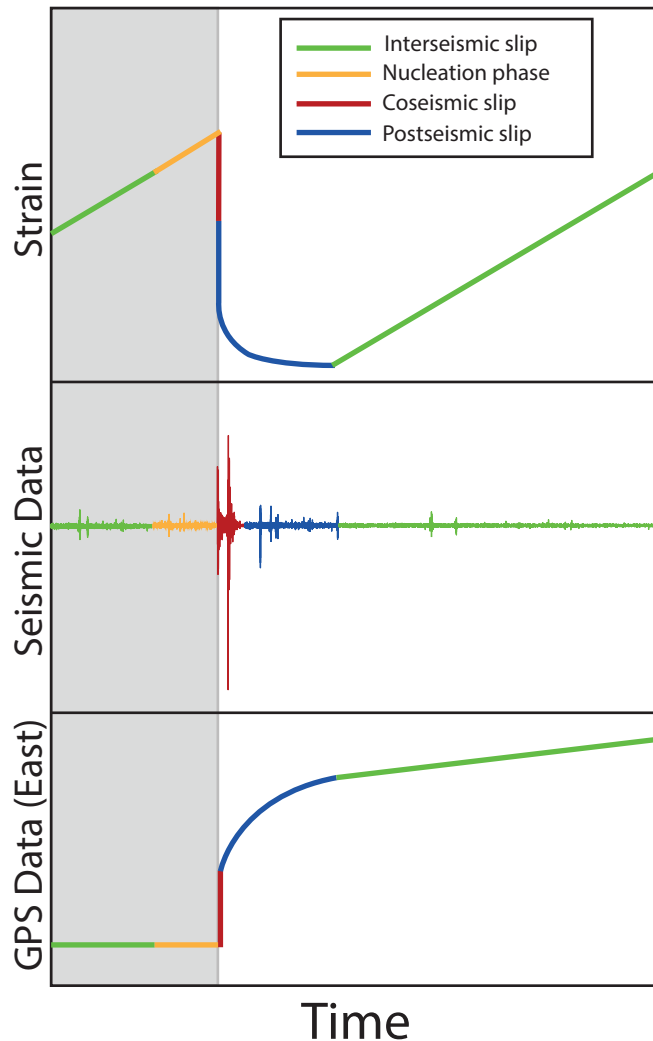
FIGURE 3.1 – The seismic cycle. Top : evolution of strain with time during the seismic cycle. Middle : example of a seismic waveform that represents a sequence with a mainshock (in red) and its foreshocks and aftershocks occurring respectively before (nucleation phase in orange) and after (postseismic phase, in blue). Bottom : displacement at surface recorded with GPS, along the East component. In this chapter, we focus on the preseismic phase that includes of the end of the interseismic phase and the nucleation phase.

when the signal to noise ratio is low preventing the detection of very small events while they are essential to capture the whole history of a preseismic phase. Thus, one of the biggest step that we must deal with towards the Grail is the detection of such small signals. Thanks to the extension of networks and the quality of acquired data we enter

a new era where we can think of the detection at a different scale : the network scale in its entirety.

The method that we present in this chapter uses the information of the coherency of the entire network in order to detect small events before the Tohoku earthquake. It has been first introduced by Mermoz (1976) and used in underwater acoustics (Bienvenu and Kopp, 1983; Turek and Kuperman, 1997; Jensen et al., 2011) and seismic exploration (Samson, 1983; Glangeaud and Lacoume, 1985; Glangeaud and Latombe, 1986). In this section, we also present the different tests to estimate the resolution of the method. We then present the results and the slip history before Tohoku earthquake.

3.2   Abstract.

The existence of transient slip episodes in the rupture zone of the Tohoku earthquake
that was highly coupled is a conandrum. In this study, we use a Multi-Dimensionnal
Template Matching (MDTM) technique in order to detect the signals emitted during
transient slip episodes that are hidden in the continuous signal. This allows to better
capture the slip history in the rupture zone of the most instrumented megathrust ear-
thquake. Indeed, we detect two types of signal : low frequency detections (between 1
and 8 Hz) that well-recorded the episodes of migration evidenced by Kato et al., (2012)
and high frequency detections (between 14 and 20 Hz) that occurred on the future rup-
ture zones of the M4.8 to M6.8 earthquakes that struck the area between the Mw7.3
foreshock and the Tohoku earthquake. The activity rate of the events detected at high
frequency started on the 2010/11/30 and increased until the Tohoku earthquake. This
increase is marked by several burst-like episodes suggesting recurrent slow slip events on
an aseismic patch north and east of their rupture zones. Thus, the rupture zones of the
M4.8 to M6.8 earthquakes appear to have been loaded during several phases, lasting for a
few months prior their ruptures. Eventually, the Mw7.3 foreshock triggered the ruptures,
further contributing in loading the asperity that initiated the M9.0 Tohoku earthquake.

3.3   Introduction

Recent laboratory experiments have evidenced a nucleation phase before rupture
of rock samples (Ohnaka, 2003; Thompson et al., 2009; McLaskey and Kilgore, 2013;
McLaskey and Lockner, 2014; Passelègue et al., 2014; Scuderi et al., 2016) and on po-
lycarbonates (Latour et al., 2013). The first observations of such a preparatory phase
prior to subduction earthquakes were made in the 1970s and 1980s after the great Chi-
lean earthquake of May 22, 1960 (Kanamori and Cipar, 1974). The authors evidenced
a low-frequency signal about 15 minutes before the main shock. This observation was
then confirmed by the analysis of the amplitude and phase spectra of signals recorded at
eight stations and by fitting them with the Haskell model (Cifuentes and Silver, 1989).
Another observation of a potential precursory phase was made before the Japan Sea
earthquake M7.7 that occurred on May 26, 1983. Linde et al., (1988) analysed the data
of three borehole strain meters and evidenced the occurrence of transient strain events
that they believe to be aseismic, a few months before the main shock. These transients
stopped only a few days after the earthquake. The analysis of teleiseismic data recorded

before the 1989 Macquarie Ridge earthquake suggests the occurrence of a slow deformation process prior the mainshock (Ihmlé et al., 1993). A more systematic analysis was done for 107 shallow-focus earthquakes and revealed that 20 of them presented such a precursory phase (Ihmlé and Jordan, 1994). Foreshock sequences were studied in California by relocating the events, especially for the 1992 Landers earthquake (Dodge et al., 1995, 1996).

More recently, repetitive seismic signals occurred within a few minutes before the 1999 Izmit earthquake, in Turkey (Bouchon et al., 2011). This can suggest either the setting of an aseismic slip in the area that surrounds the asperity and that rapidly reloads it or a stress-transfer driven cascade as observed by Ellsworth et al. (2016) who used 9 stations to analyze the sequence of foreshocks that occurred before the Izmit earthquake. The existence of slow slip prior the Tohoku-oki earthquake (Kato et al., 2012; Ito et al., 2013) as well as multiple slow-slip events before the Mw8.1 Iquique earthquake that occurred in Chile, in 2014 (Kato and Nakagawa, 2014) were evidenced by studying repeating earthquakes in the main shock areas. Also, the Papanoa earthquake that occurred on April 2014, in Mexico was clearly triggered by a large slow slip episodee observed with GPS data (Radiguet et al., 2016). These observations strongly suggest the occurrence of aseismic slip in the area that surrounds the earthquake asperity and that rapidly loads it.

The displacement of inland GPS stations before the Tohoku earthquake shows a decrease of slip deficit rate, hence of coupling, between 1998 and 2011 downdip the coseismic rupture zone of the megathrust earthquake (Mavrommatis et al. (2014); Yokota and Koketsu (2015), figure 3.2).

This indicates the occurrence of a long-term and largescale deformation transient before the Tohoku earthquake. The preseismic phase of the megathrust earthquake begins to be seen in the catalog in mid-January, coincidently with an increase of deep (>80km) seismicity (Bouchon et al. (2016), figure 2.5). The preseismic phase went on as a burst-like seismicity in mid-February that lasted for about 23 days (Hirose et al., 2011). Two days before the mainshock, a Mw7.3 foreshock struck close to the initiation point of the Tohoku earthquake. The seismicity between this largest foreshock and the mainshock includes several M≥6 earthquakes and appears to migrate towards the mainshock epicenter, suggesting the presence of afterslip (Ando and Imanishi, 2011) and/or interaction mechanisms between earthquakes (Marsan and Enescu, 2012). Two distinct sequences of slow-slip transients propagating towards the rupture initiation point were evidenced by the detection of REs (Kato et al., 2012).
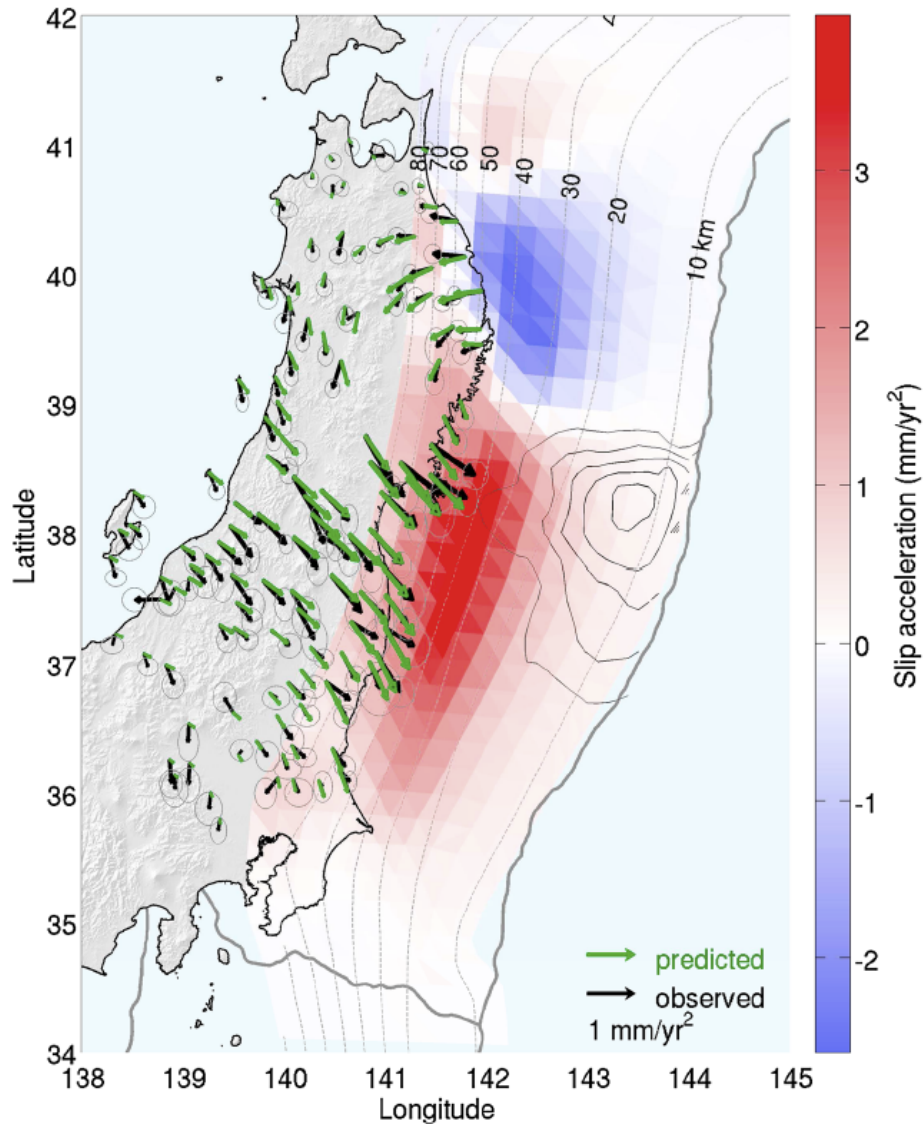
FIGURE 3.2 – Inversion of interseismic accelerations for slip acceleration on the Japan
Trench plate interface. Observed accelerations with 2σ error ellipses are shown in black ;
model fit in green. Colored patches show the estimated distribution of slip acceleration
(dip-slip component) on the plate interface. Black contours indicate the slip distribution
of the 2011 Mw 9.0 Tohoku-oki earthquake in 10 m intervals (Hooper et al., 2013) from
(Mavrommatis et al., 2014).

However, the detailed analysis of the seismicity during the preseismic phase is missing.
The density of the Japanese seismic network of continuous and broad-frequency range
stations offers a unique opportunity to apply an improved detection technique before the
Tohoku earthquake.

Several methods were developped in the past to detect and localize small events using matching phase signals on an array (Got et al., 1994; Rost and Thomas, 2002; Gibbons and Ringdal, 2006). In earthquake detection, the technique of cross-correlation between seismic events has been widely used to detect Repeating Earthquakes (Nadeau and McEvilly, 1997; Matsuzawa et al., 2002; Uchida et al., 2003; Kimura et al., 2006). The waveform matching technique was also successful in detecting low frequency earthquakes (LFE) and non-volcanic tremors (NVT), (Shelly et al., 2007; Aso et al., 2011) as well as detecting missing earthquakes during foreshock (Bouchon et al., 2011; Kato et al., 2012) or aftershock sequences of large earthquakes (Lengliné and Marsan, 2009; Peng and Zhao, 2009; Lengliné et al., 2012).

In this study, we apply a spectral matrix analysis technique that has been first introduced by Mermoz (1976) and used in underwater acoustic (Bienvenu and Kopp, 1983; Turek and Kuperman, 1997; Jensen et al., 2011) and seismic exploration (Samson, 1983; Glangeaud and Lacoume, 1985; Glangeaud and Latombe, 1986). This method considers the network as an array of receivers instead of using the classical station by station approach. We use all the M$\geq$ 2 earthquakes that occurred from mid-February 2011 to the time of the megathrust earthquake as templates events and we search for their matches in the continuous signal from 2011/1/1 to 2011/3/11.

3.4 Data and Methods.

3.4.1 Method

The method presented here is a Multi-Dimensional Template Matching (MDTM) technique based on the use of the spectral density matrix of a template recorded by an array of sensors. The algorithm is implemented in the frequency domain. A template is composed with signals $d_j(t)$ recorded in the time-domain, we first align the traces in order to have all the P wave arrival times at the beginning of the window. To do so, we estimate the time of arrival at each station using a P wave velocity of 6.8 km/s. Precision is not necessary here but we must have the information about the coherent signal that we want to retrieve in the continuous signal (so all the P waves in the window). Then, we compute the Fourier transform of the signals for the N stations : $d(\omega) = [d_1(\omega), ..., d_N(\omega)]$, where $d_j(\omega) = FT[d_j(t)]$ and calculate the cross-spectral density matrix (CSDM) K (i.e. a N x N matrix) as :

$$K(\omega) = d(\omega)d^*(\omega), \tag{3.1}$$

where $*$ indicates the Hermitian transpose operation (figure 3.3).

The information that we wish to retrieve in the continuous signal is the phase of the signals for every station. Furthermore, we search for signals that contain balistic waves and are thus coherent between stations.

The next step consists in decomposing the matrix K in eigenvalues and eigenvectors. Since the matrix K is squared and hermitian, an eigen decomposition or a Singular Value Decomposition (SVD) give the same results. Here, we use the eigen decomposition as :

$$K(\omega)v = \lambda v. \tag{3.2}$$

This allows to decompose the CSDM as an ensemble of eigenvectors v and eigenvalues λ that we sort in descending order.

We apply the same moveout on the continuous signal as we did for the template events using a P wave velocity of 6.8 km/s. Using the first eigenvector that contains the most energetic and coherent signal, we can define a new trace that is a projection of the continuous signal D, where $D_j(\omega) = FT[D_j(t)]$ on the first eigenvector for every frequency as :

$$Z(\omega) = \sum_{i=1}^{N} v_1^* D(\omega) v_1. \tag{3.3}$$

At this stage, we obtain N signals $Z_j(t)$ in time, one per station j, obtained by the inverse FT of $Z_j(\omega)$. Once the projected signal is defined, we can easily work in the time-domain in order to compare the template and the output. To do so, we define a reference signal for the template on one hand and for the output on the other hand by propagating the signal recorded at station j to one reference station. This prevent from calculating the coherency station by station and has the advantage of keeping the information contained in the output signal. The reference station is the one with the highest signal-to-noise ratio among the ten first arrival stations. We define the propagator (Green function) as :

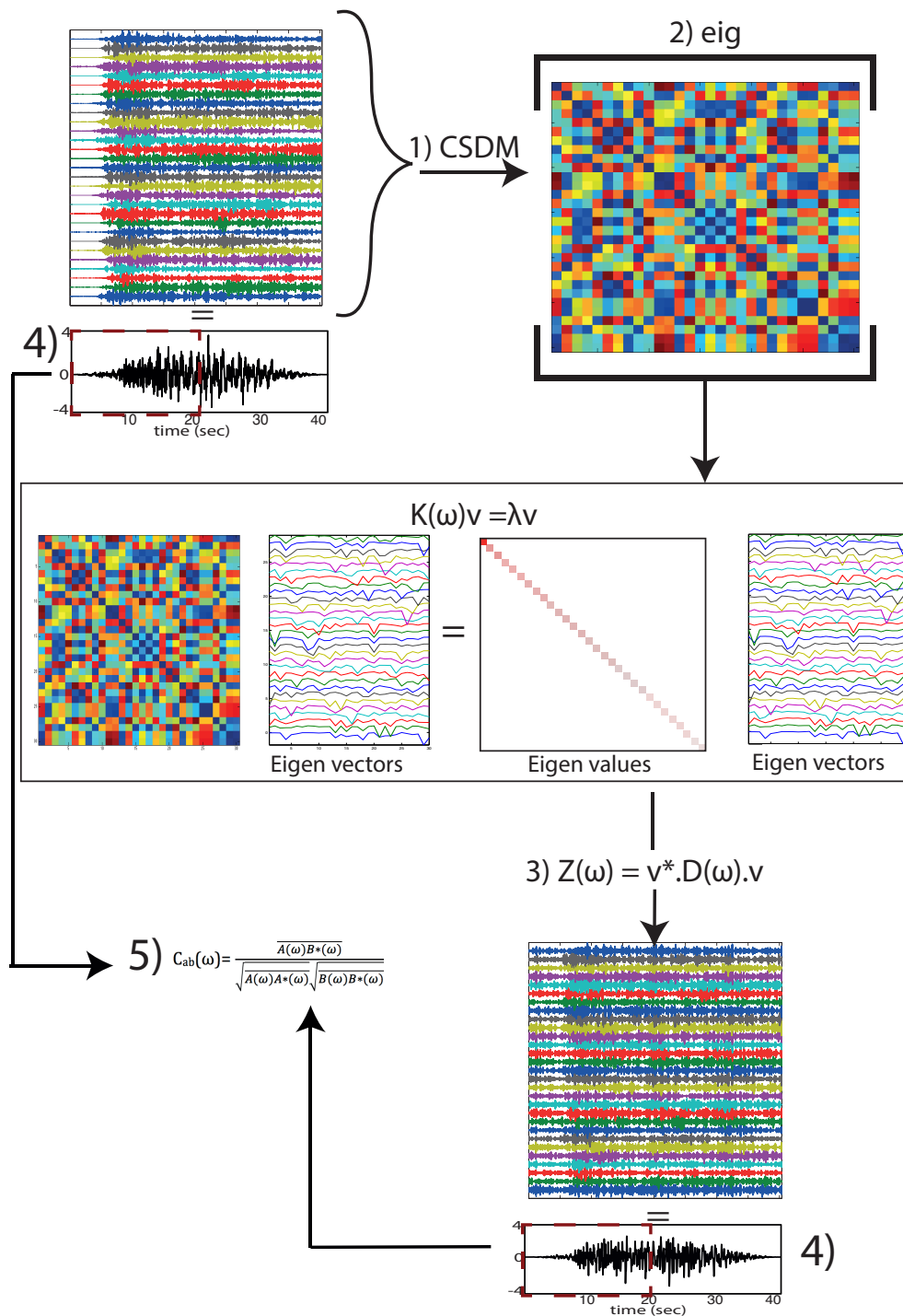$$G_j(\omega) = \frac{d_{ref}(\omega)}{d_j(\omega)}, \tag{3.4}$$

FIGURE 3.3 – Description of the stages used in the detection algorithm. 1) CSDM calculation, 2) Eigen Decomposition, 3) Projection on the continuous signal using the eigen vectors. 4) Definition of the reference signals, 5) coherency calculation.

with $d_{ref}(\omega)$ the Fourier transform of the signal recorded at the reference station and $d_j(\omega)$ the Fourier transform of the signal recorded at station j.

Finally, we obtain a reference signal A for the template :

$$A = d_{ref}^{(j)}(t). \tag{3.5}$$

We do the propagation (equation 3.6) and sum (equation 3.7) for the projected signals $Z_j(\omega)$ using the very same Green function $G_j(\omega)$, to obtain B :

$$Z_{ref}^{(j)}(\omega) = Z_j(\omega)G_j(\omega). \tag{3.6}$$

$$B = \frac{1}{N}\sum_{j=1}^{N} Z_{ref}^{(j)}(t). \tag{3.7}$$

The last stage of the detection algorithm consists in calculating the coherency between A and B (figure 3.3, 5) over their 20 first seconds, which correspond to the arrival and coda of the P wave, as :

$$C_{AB}(\omega) = \frac{\overline{A(\omega)B^*(\omega)}}{\sqrt{\overline{A(\omega)A^*(\omega)}}\sqrt{\overline{B(\omega)B^*(\omega)}}}. \tag{3.8}$$

The coherency is calculated between two frequencies, f1 and f2, with f ranging between 1 and 20 Hz, and $f2 = f1 + \Delta f$ with Δf=5 Hz minimum. We keep only the maximum value of coherency from all the calculated frequency bands.

We compare this detection method with the simple calculation of the coherency station by station. To do so, we add a certain level of noise to the original data and calculate the coherency between 1 and 8 Hz, station by station, between the original and the noisy signals with or without projection (figure 3.4). The signals are normalized and the noise standard deviation is n times the standard deviation of the signal. We first compare the two detection methods for an auto-detection (cf fig. 3.4a) and see that without any noise in the signal, the coherency without projection is equal to 1. It is slightly lower, although it remains high, with the projected signal. This is due to the fact that the projected signal is a linear combinations between stations due to the projection step. It is still possible to obtain a high coherency value (above 0.9) with noise up to 2 times the amplitude of the signal with the projection method. The coherency value

then decreases rapidly when the noise level increases further but it is always higher than without projection. We also test the results with two different signals that do not show any similarity and see that the coherency is always low regardless of the noise level (cf fig. 3.4b) : the projection thus does not create artificially high coherency values when the continuous signal does not contain the template waveform.
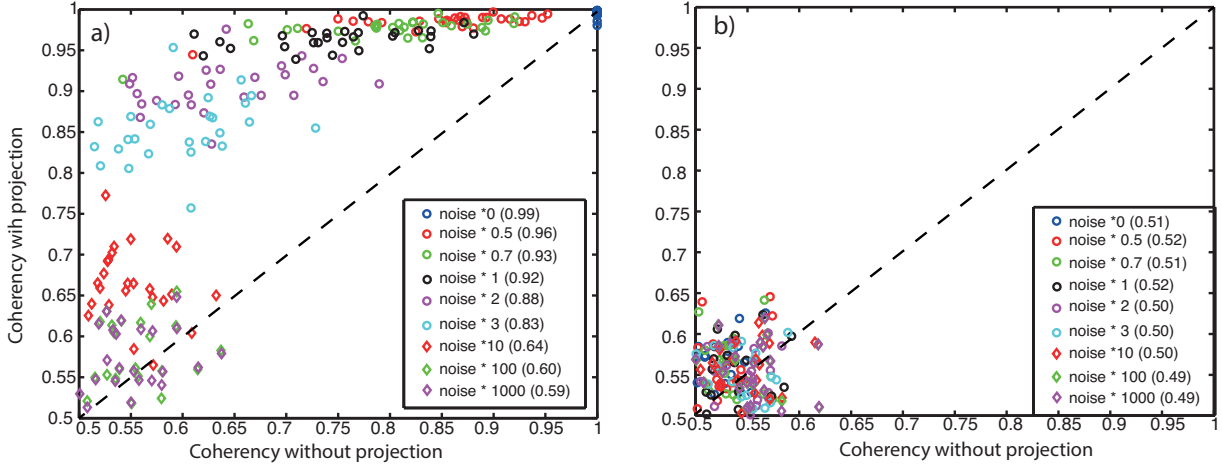

FIGURE 3.4 – Comparison of the coherency calculated with and without projection at every station used in this study. The level of noise is given in the legend. The coherency between the two reference signals for the projection method is given in brackets for every noise level. The dashed line has a slope of 1. a) for an auto-detection : the noise is added to the original data and we calculate the coherency between the original and the noisy signal ; b) the noise is added to a random earthquake signal that bears no similarity with the template.

3.4.2 Data

The preseismic phase of the Tohoku earthquake seems to start in mid-January coincidently with an outburst of deep seismicity (Bouchon et al., 2016). The preseismic phase went on with bursts of seismicity in mid-February that lasted about 23 days (Hirose et al., 2011). Two days before the mainshock, a Mw7.3 foreshock struck close to the initation point of the Tohoku earthquake (figure 3.5). The post-seismic slip of this foreshock is mainly located between the two epicenters (Ohta et al., 2012). Furthermore, its aftershocks were mostly located north to the epicenter (figure 3.5 b).

In order to apply the array-based technique, we use all the 498 $M \geq 2$ earthquakes

that occurred from 2011/2/13, time of the beginning of the study by Kato et al. (2012),
to 2011/3/11, in the JMA catalog, as the template events.

Using the technique presented above, we search for resembling signals in the vertical
component of continuous signals of 33 Hi-net stations located in Tohoku prefecture (figure
3.5). The sampling frequency of these stations is 100 Hz. We analyzed the continuous
signal from the 2011/1/1 to the 2011/3/12 in order to observe the potential activation
of the area around mid-January.

The projection of the CSDM is done for every template over the gap filled continuous
signal on a sliding window that is 4096 samples long (40.96 sec) and that slides every
512 samples (5.12 sec). Every coherency value is kept in an output file. We establish a
first coherency threshold as the mean + 5 times the standard deviation which gives a
value around 0.73. We finally filter out duplicate detections of the same event that were
detected by several templates by taking the maximum coherency value in every 40s -long
windows. An example of a detection is given in figure 3.6. The detection is highest at
high frequencies, between 14 and 20 Hz. The algorithm allows to detect mainly the P
wave arrival which corresponds to the most energetic phase at high frequencies (figure
3.6 on the right).

3.4.3   Tests on the method

In this section, we present different tests conducted to explore the robustness and
limits of the method.

First, we analyse the use of the reference signals compared to the calculation of the
coherency station by station 1) using the maximum coherency value and 2) using the
coherency calculated between 1 and 20 Hz (figure 3.7). To do so, we use a pair of events
that are highly similar so the output coherency is close to 1 in the best-case scenario.
The coherency computed between 1 and 20 Hz presents value between 0.7 and 0.9. The
use of a sliding window with a minimum length of 5 Hz to compute the coherency and to
keep the maximum value logically improves the coherency at every station. Finally, the
computation of the coherency between the two reference signals gives a value of 0.995
which is slightly above the mean coherency computed with the maximum value (0.99).
The computation of the coherency using reference signal is faster than calculating it
station by station and it allows to keep only one characteristic value after the projection.

Using the same pair of events, we test if the detection is robust by replacing the signal
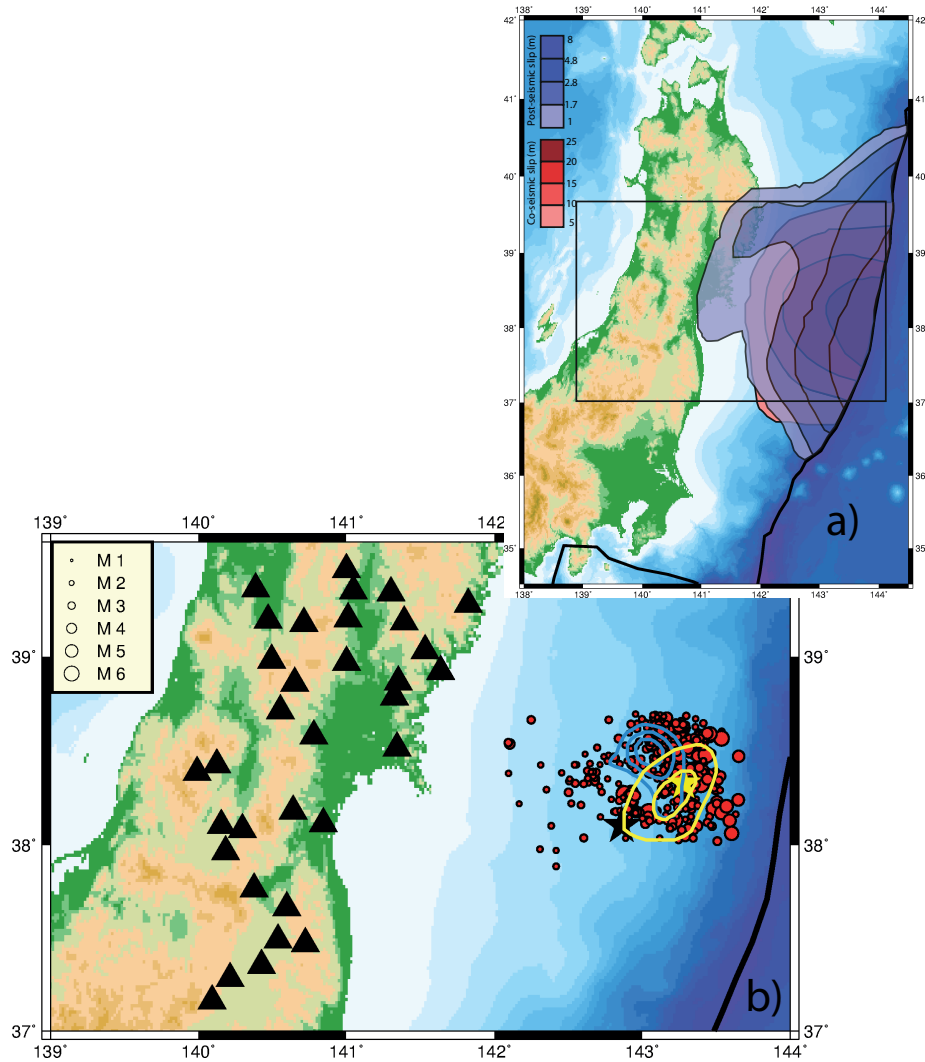
FIGURE 3.5 – Map of the region of the 2011 Tohoku-oki earthquake. a) Co- (red) and post-seismic (blue) slip distribution of the Tohoku eartquake estimated using both GEONET GPS stations and six near trench stations that include co-seismic slip and 21 days of post-seismic slip (modified from Perfettini and Avouac (2014)). b) Location of the templates (red circles) and of the Hi-net stations (black triangles) used in this study. The black and yellow stars locate the epicenter of the Tohoku earthquake and its Mw7.3 foreshock. Estimated co-seismic and post-seismic slip ditribution of the Mw7.3 foreshock are given with blue and yellow contours drawn at respectively every 0.5 m and 0.1 m interval with a maximum of 1.5 m and 0.4 m (Ohta et al., 2012).

of the template by continuous signal that contains only noise at one or more station and computed the coherency of the reference signals after projection (figure 3.8). If we chose a threshold of 0.8, we can still detect the event with a minimum of 5 stations. For a
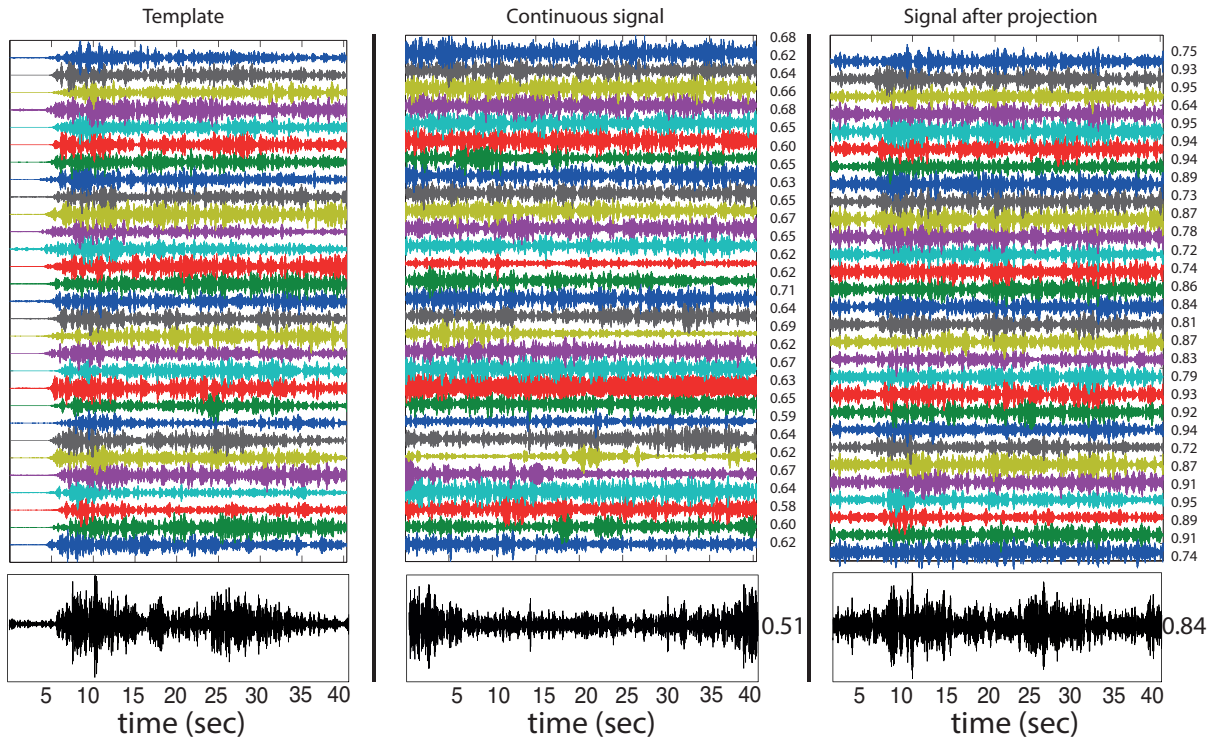
FIGURE 3.6 – Example of a detection at high frequencies (between 14 and 20 Hz). The template signal recorded at every station is shown on the left. We project the first eigen vector of the CSDM of the template over the continuous signal that is shown in the middle, obtaining the projected signal (on the right). The coherency values between the input signal on one hand and the continuous and projected signals on the other hand are shown on the right of every trace. The black signals at the bottom show the normalized reference signals and the coherency values between the reference signals are indicated on the right.

higher threshold, of 0.9, it is not possible to detect the event when half of the stations are replaced by noise. This indicates that the method is robust and works even with a small number of stations. However, it is better to use numerous high quality stations (20 to 30) in order to increase the number of detections.

Then, we test different lengths of sliding window to see if we can gain in precision on the coherency value (figure 3.9). The method indicates that when shortening the duration of the sliding window we improve the accuracy on 1) the coherency value and 2) the time of detection since a sliding window of 64 samples is shorter than one second. However, the computation of the algorithm with sliding windows of 64 and 128 samples is highly time and CPU consuming and not realistic when considering almost 500 templates over
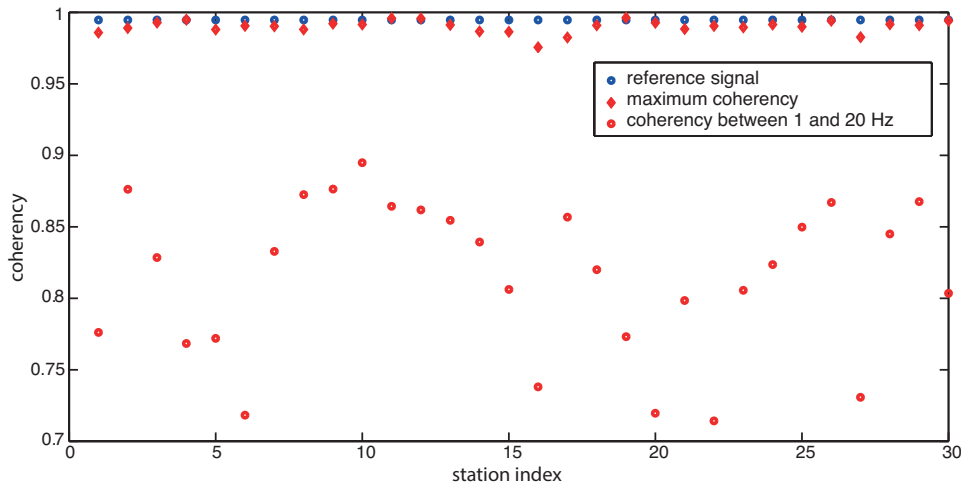
FIGURE 3.7 – Comparison of the coherency values using : the coherency computed between 1 and 20 Hz (red dots), the maximum coherency obtained using a sliding window on the frequencies (red diamonds), the reference signals (blue dots).
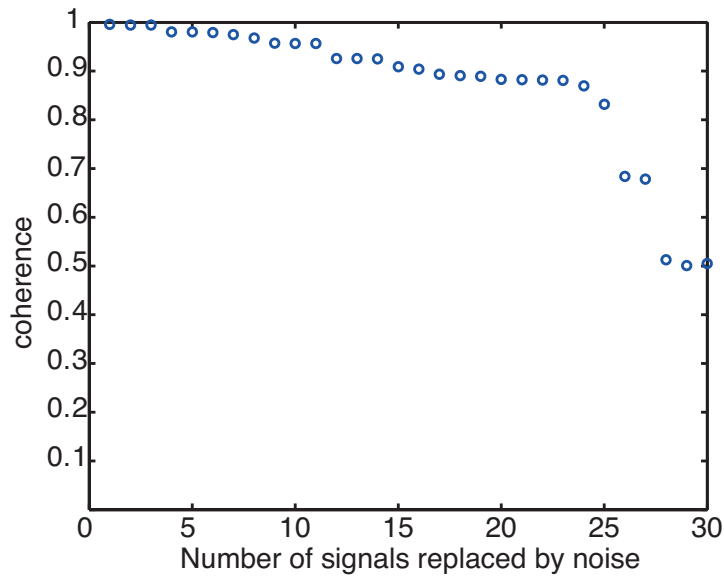

FIGURE 3.8 – Coherency values obtained by replacing template waveforms with noise signal at one or more stations.

three months of continuous data. Thus, we chose to work with a sliding window of 512 samples (around 5 seconds) which might underestimate the coherency value between the reference signals but still allows detection, including all the auto-detections. We also

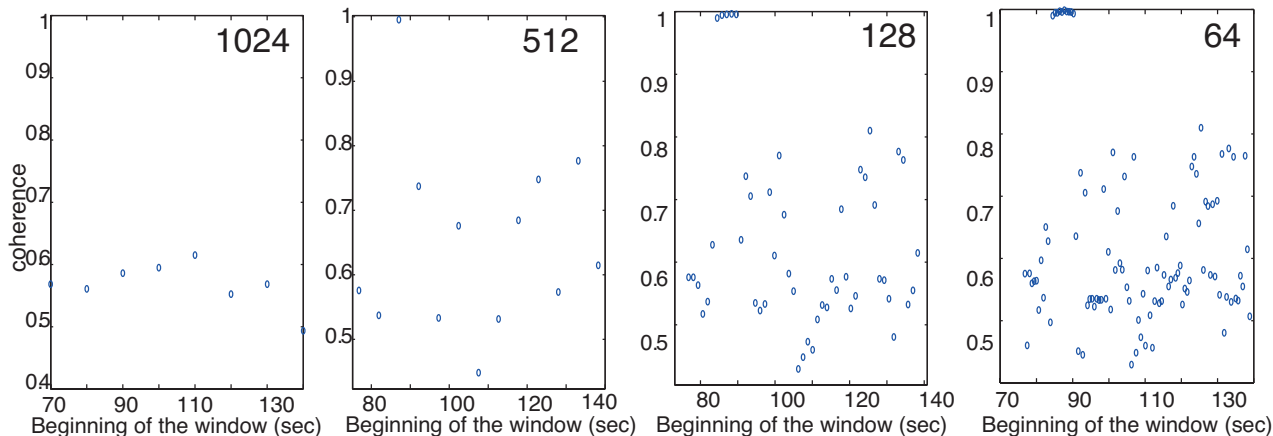tested longer windows (1024 samples) but we missed several auto-detections.

FIGURE 3.9 – Coherency value for different lengths of sliding window (1024, 512, 128, 64 samples) on the continuous signal according to the time of the beginning of the window. There is no detection for a 1024-sliding window. There is a detection at 87 seconds with a sliding window of 512 with a coherency of 0.99. The detection occurs from 84 to 90 sec with a sliding window of 128 samples with a maximum coherency of 0.991. With a sliding window of 64 samples, the detection occurs at 87.3 seconds with a maximum coherency of 0.999.

The MDTM algorithm was classicaly used to separate waveforms by projecting on the eigenvectors of the CSDM or on models (Jensen et al., 2011; Corciulo et al., 2012; Chmiel et al., 2016). In order to separate the waveforms, the CSDM has to be averaged in order to obtain a full-rank matrix. To average the matrix, we can apply an apodization at every frequency. We then perform the projection on the first eigen vector of the CSDM at every frequency. Here, we test the effect of such averaging over a pair of events that are less similar than the previous one. We used the 22 stations that present the higher signal-to-noise ratio (figure 3.10).

The coherency value obtained without projection varies from 0.7 to 0.9. The application of the projection with apodization improves the results at every station (black diamonds) and the computation of the projection without averaging allows to estimate higher coherency values. The two coherency values obtained with the signal reference with and without apodisation are similar, though. The improvement of the coherency computed without averaging is due to the fact that we keep all the coherent information on the first eigenvector and we do not separate the signal into different waveforms. Thus,

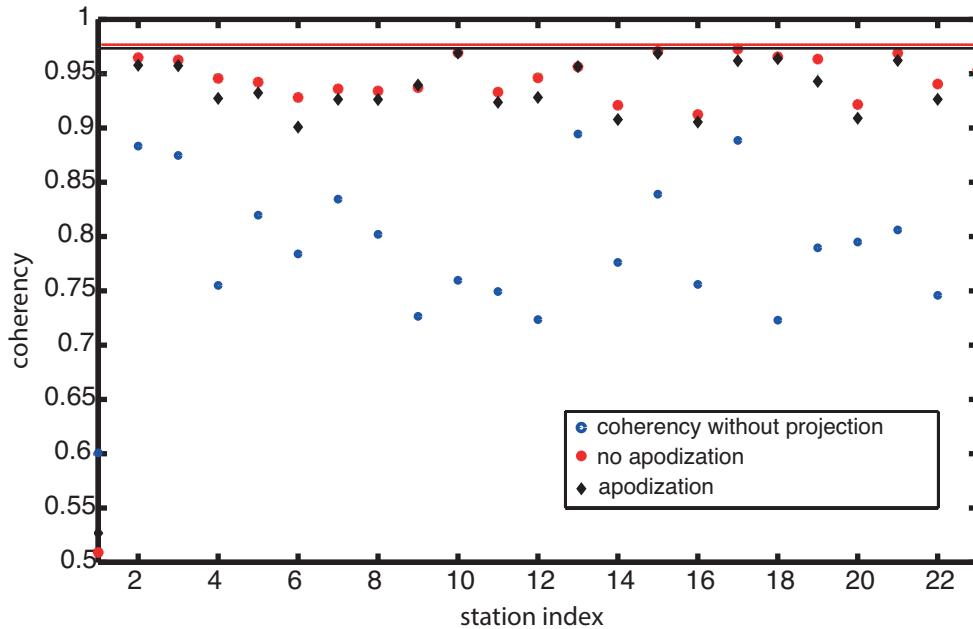in the following, we do not compute the average of the CSDM.

FIGURE 3.10 – Coherency values computed station by station without projection (blue dots) with projection and average over the CSDM (black diamonds), with projection but without averaging the CSDM (red dots). The black and red line indicate the values of the coherency between the reference signals with the projection and with (black) or without (red) the average on the CSDM.

These tests allow to conclude on the robustness of the method obtained by 1) computing the maximum coherency value, 2) using 30 stations, 3) not computing the average over the CSDM.

3.4.4 Spatial Resolution

By using the MDTM algorithm it is possible to detect small earthquakes hidden in low signal-to-noise ratio signals. However, the technique is based on the analysis of the CSDM and on a linear combination between the traces of all the stations used. Therefore, the absolute time and the real signal amplitudes are not conserved after projection, unabling us to obtain the precise time of occurrence nor the magnitude. Since the window of analysis slides over 5 seconds, we do know that the detected events occurred during this time lapse however, it is impossible to relocate the events using methods based on time-delay estimation. The use of the continuous signal could be a solution but it is highly

noisy for most of the detections (cf fig. 3.6, middle) preventing us from calculating a time-delay. To better constrain the distribution of the distance between a template and its detected events, we compute the coherency and the distance for every pair of events used as templates without taking into account the auto-detections (figure 3.11).
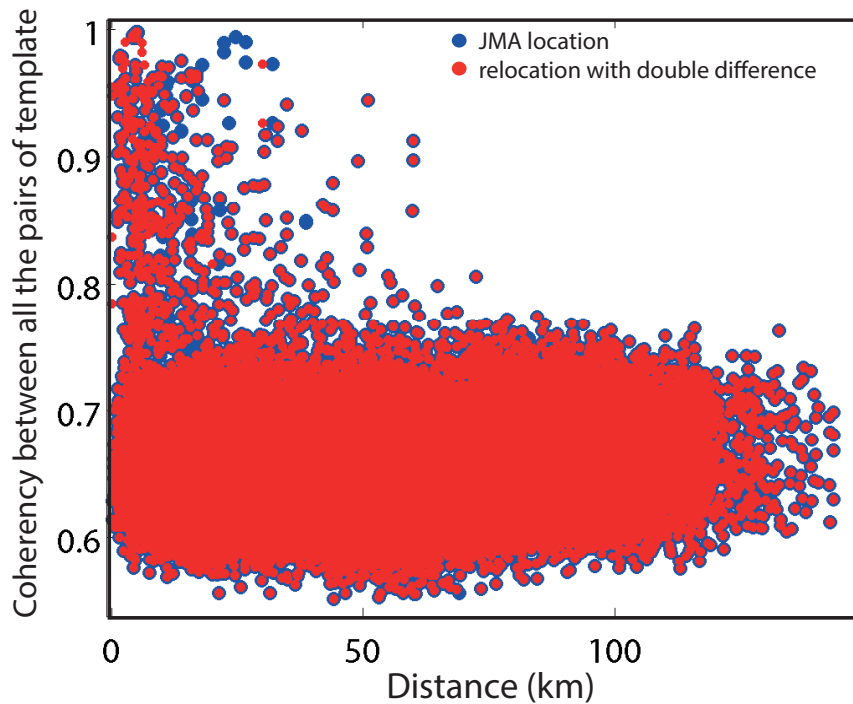

FIGURE 3.11 – Coherency vs distance for every pair of templates used in this study. The blue dots represent the hypocentral distances calculated with the JMA locations, the red dots are the distances after relocation of the templates (cf chapter 4). The black line indicates the coherency threshold of the mean + 5 times the standard deviation.

We calculate the hypocentral distances using the locations of the JMA catalog. The pairs that have a coherency ≥ 0.9 are relocated following the method presented in chapter 4 and plotted in red in figure 3.11. There is a large dispersion when considering the coherencies under the threshold of the mean + 5 times the standard deviation : distance spans from 0 to 180 km. Thus, the threshold gives a first mean to sort the results out. The distribution of the coherency vs distance is widely spread out for coherencies between 0.7 and 0.75 but also between 0.75 and 0.8 (figure 3.12). It is clearly visible that the distribution begins to be more concentrated to small distance values at a coherency threshold of 0.8.

Furthermore, 84% of the pairs of templates are located below 22.6 km for this thre-
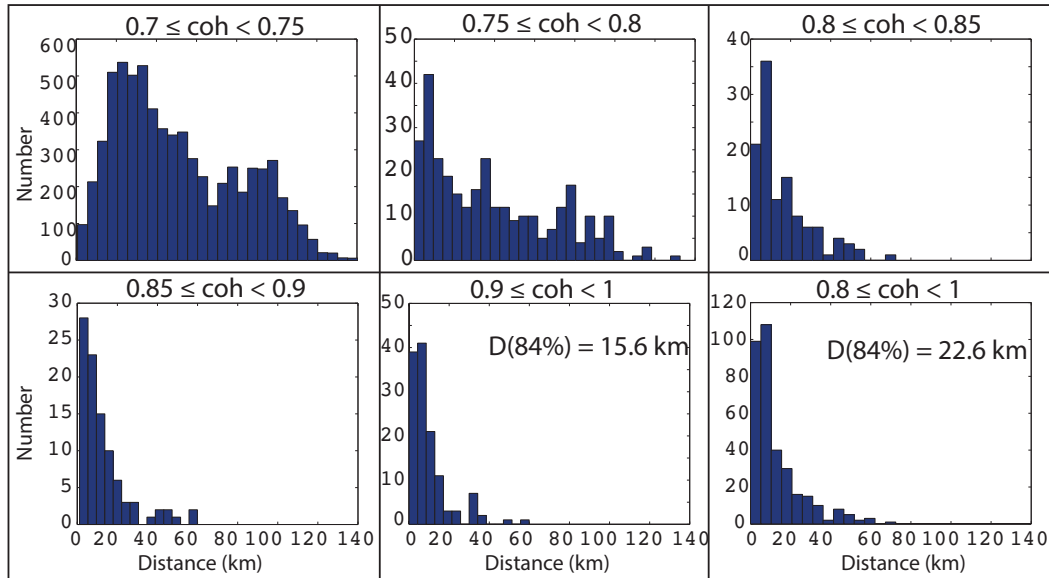
FIGURE 3.12 – Distribution of the number of pairs according to the distance for different values of coherencies indicated at the top of the histograms.

shold and below 15.6 km for coherencies between 0.9 and 1 (figure 3.13). The trend is similar when considering 84% or 95% of the pairs : the distance suddenly increases for values of coherencies smaller than 0.8. Thus, we will consider a threshold of 0.8 thereafter, keeping in mind that the spatial resolution is around 20 km at this value.

FIGURE 3.13 – Distance that contains 84% (in blue) or 95% (in red) of the pairs of template above different coherency thresholds.

To test if the signals detected at this threshold are really physical, we stack the
continuous signal using 30 detections obtained using one single template signal. The
coherency between the projected and the template reference signals range between 0.80
and 0.89 with a mean of 0.84 at high frequencies (between 14 and 20 Hz). As already
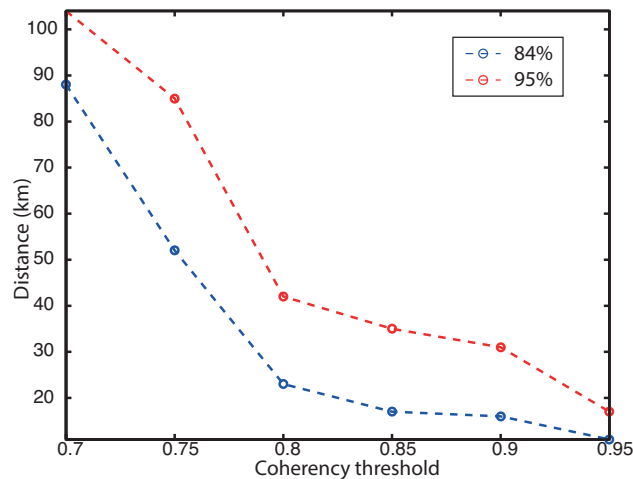mentionned before, we know the time of detections with a precision of 5 seconds. We
computed the coherency between the template and the continuous signal around the
time of the detections between 1 and 20 Hz to align the continuous signals at the time
of the highest coherency value. We filter the signals at low frequencies (between 0.7 and
3 Hz) to select the most coherent part of the signals for stacking.

An example is shown in figure 3.14 for the station N.KAKH. The stack present a
phase coherent with the template from 3 to 10 seconds. This corresponds to the direct
P wave arrivals. The signal between 10 and 20 seconds correspond to the P coda waves.
The S wave arrives at around 22 seconds (not shown in the figure) but is not dominant
at high frequencies so we chose to focus on P waves (figure 3.6, left). The stack indicates
that we detect coherent energetic signals but that the coda are not coherent. Thus, the
method allows to detect resembling earthquakes along with repeating earthquakes that
present similar P waves and codas waves suggesting slightly different source locations.
This implies that the scatterers activated with the P coda wave are distributed over more
than 20 km.

3.5   Earthquake detection.

In order to apply the array-based technique, we use all the 498 $M \geq 2$ earthquakes
that occurred from 2011/2/13, time of the beginning of the study by Kato et al. (2012),
to 2011/3/11, in the JMA catalog, as the template events.

By applying the MDTM method, we detect 465 new additional events from 2011/1/1
to 2011/3/12. For this period of time, the JMA catalog counts 921 earthquakes with a
magnitude $\geq$0 including the 498 templates that we used. 201 events already listed in the
JMA were detected with our method (so these earthquakes have a mgnitude comprised
between 0 and 2) and the rest is too far away (more than 70 km on average) from the
templates to be detected. Thus, by using the MDTM algorithm, we detect 391 new
events. As it is not possible to relocate these events using the time-delay calculation, we
hypothesize that they come from the surrounding of the template location (i.e. within 20
km, the spatial resolution of the method). Thus, the events are mainly located close to
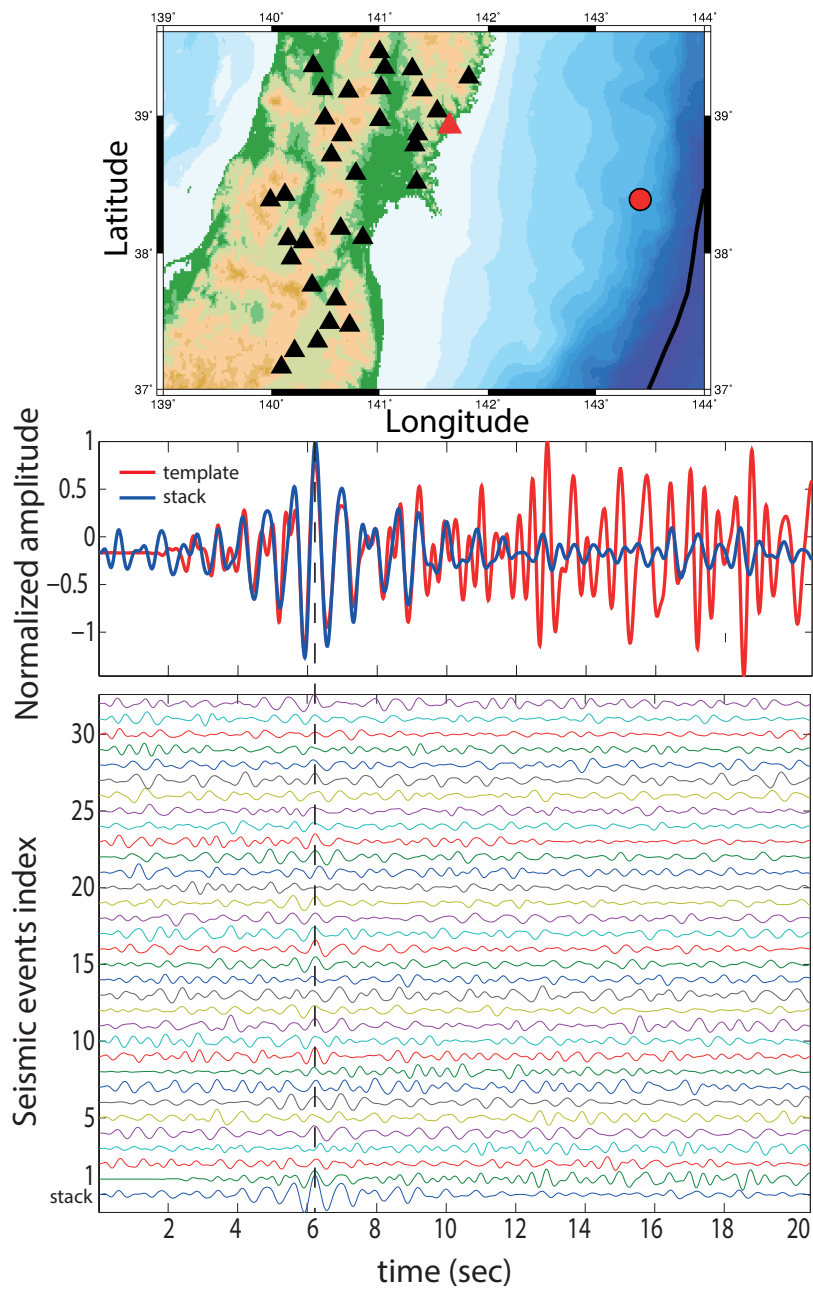
FIGURE 3.14 – Example of a stack calculated on the continuous signal for 30 detections at station N.KAKH. a) location of the template (red dot) and the station used (red triangle). b) template (red) and output of the stack (blue) for this station. c) Normalized traces of the continuous signals for every detection pass-band filtered between 0.7 and 3 Hz. The stack is shown at the bottom.

the Tohoku-oki and its Mw7.3 foreshock where most of the templates are located (figure 3.15).
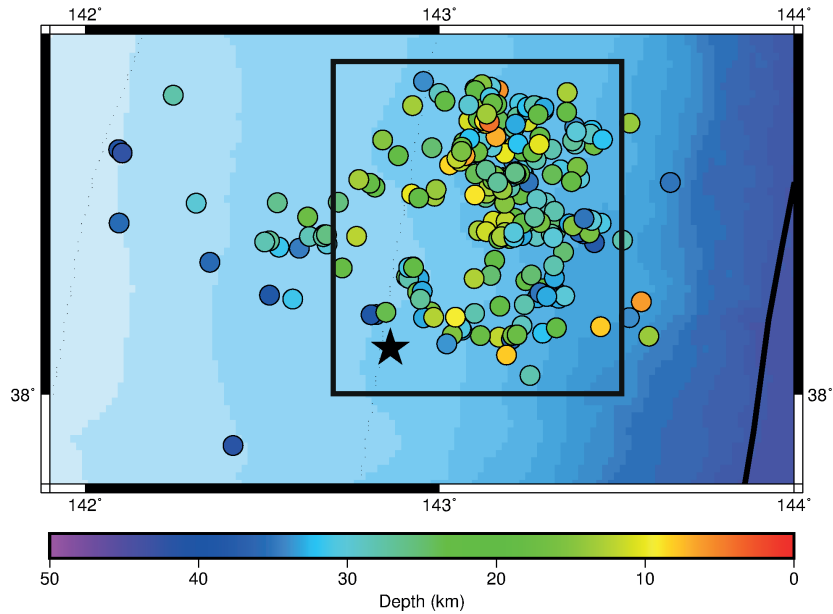
FIGURE 3.15 – Locations of the templates that have at least one detection, other than
their auto-detection, color coded according to their depths. The black rectangle shows
the area studied in figure 3.18.

The analysis of the number of detection according to the template magnitudes indicates that large magnitude template (M5, M6) detects as many times as small magnitudes (M2) even if the distribution of the template magnitudes follows a classical Gutenberg-Richter law (figure 3.16).
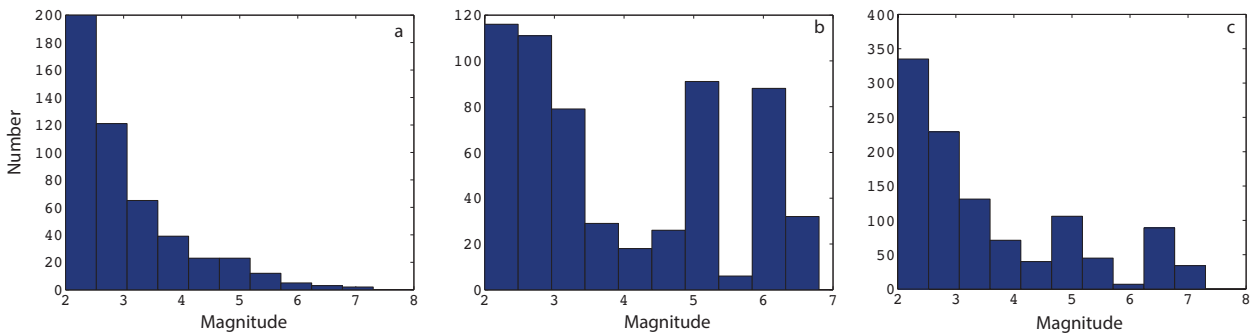
FIGURE 3.16 – Right : number of templates according to their magnitude ; middle :
number of detections according to the template magnitude ; left : number of detections
according to the template magnitude taking into account the auto-detection.

Furthermore, the M2 to M4 templates mainly detect events within a low frequency band, with a mean f1 at 3 Hz (figure 3.17). On the contrary, large magnitude templates

detect at high frequencies (f1 between 10 and 15 Hz). There is also a remarkable gap between these two end-members where only a few detections are found. The corner frequency of a M2 event being around 5 Hz, it is not surprising to detect at low frequencies for small earthquakes. At high frequencies, the signal to noise ratio increases which allows to detect smaller signals. These detections correspond to the high frequency source function radiation of large earthquakes.
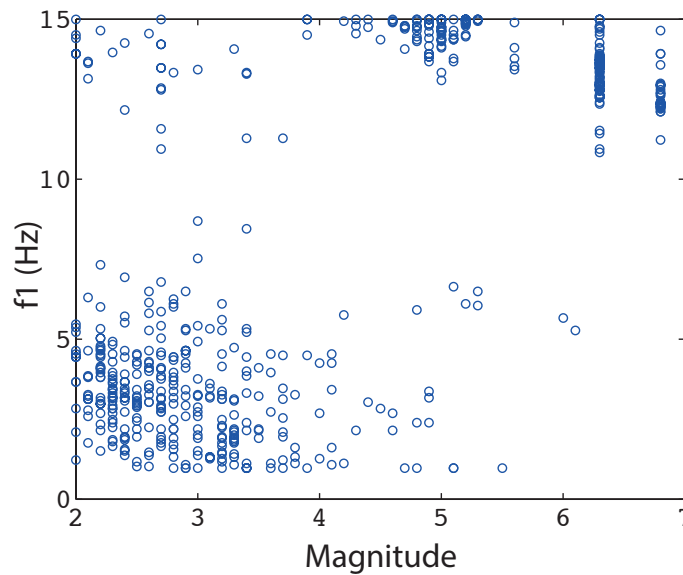

FIGURE 3.17 – Lower frequency (f1) for the frequency window used in the coherency calculation (in Hz) versus the template magnitudes. Note that auto-detections are not shown here.

The preseismic phase of the Tohoku earthquake began in mid-January with burst-like seismicity in the studied area defined by the black rectangle in figure 3.15, that can barely be seen in the JMA catalog (figure 3.18).

It triggered 19 new events and lasted 30 hours. This coincides with a sudden increase of activity at depth (Bouchon et al., 2016). The seismic activity is then rather constant until the second burst that occurred from the 2011/2/13 to the 2011/2/16 when 37 earthquakes occurred over 72 hours. After this burst, the seismic activity is ten times higher than the previous seismic rate until the 2011/2/26 when a third burst similar to the previous one occurs. It also triggers 37 events over 73 hours. After this burst, the activity is almost back to its normal rate and increases one more time during a seismic burst on the 2011/3/7 that lasts 24 hours and triggers 14 earthquakes. After this smaller burst a quiscence settles until the Mw7.3 foreshock rupture.
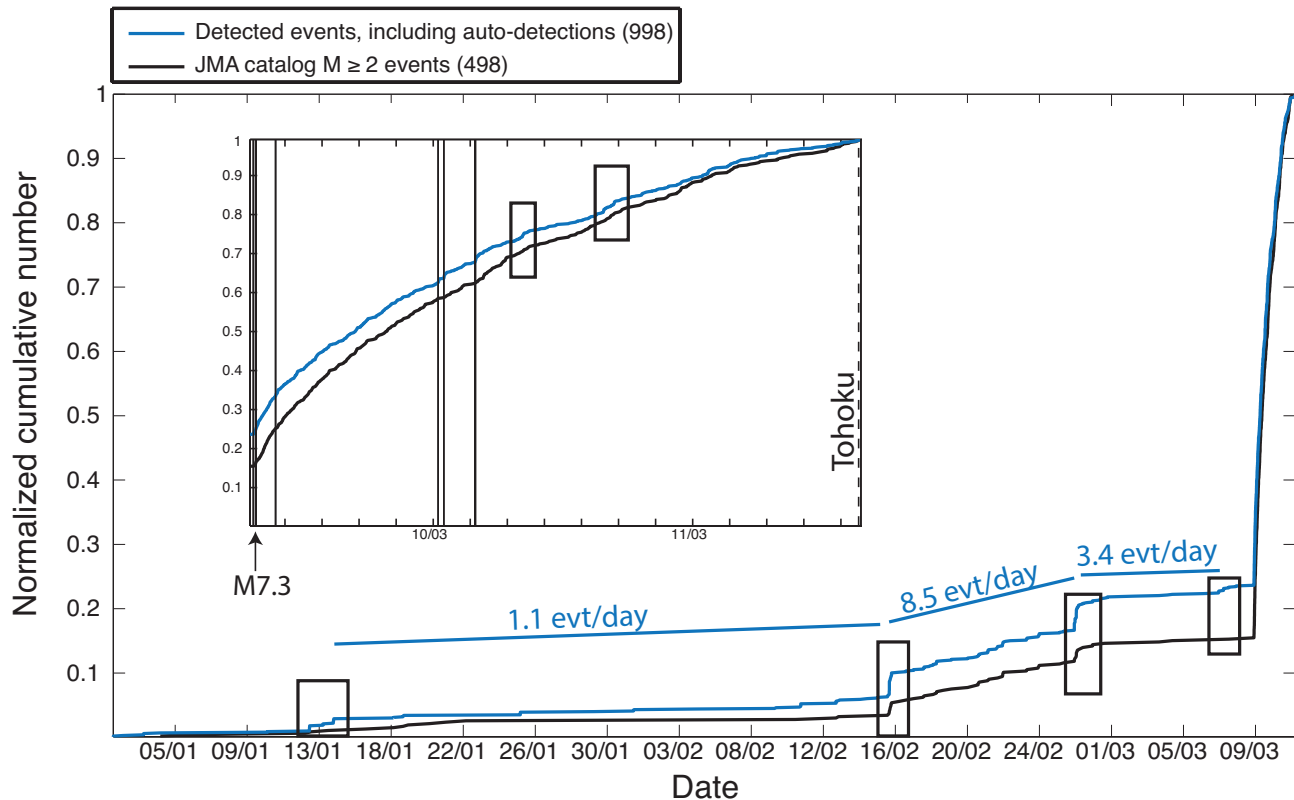
FIGURE 3.18 – Normalized cumulative number of events with time that are detected in the black rectangle of figure 3.15. In blue : all detected events (including the auto-detections) ; in black : all the M≥2 earthquakes in the JMA catalog. The total numbers are given in bracket in the legend. Inset : zoom on the period after the Mw7.3 foreshock. The black lines indicate the time of occurrence of M≥6 earthquakes and the dashed line indicates the Tohoku earthquake.

Other bursts of activity happen between the Mw7.3 foreshock and the Tohoku-oki earthquake. These are mostly due to M≥5 earthquakes that occurred after the foreshock. The small number of detections after the megathrust rupture suggests that coseismic slip was relatively uniform in the area, which is consistent with the lack of aftershocks there (Lengliné et al., 2012).

As already mentionned, the events are detected either at low frequencies ($1 \leq$ f1 $\leq$ 5 Hz) or at high frequencies (f1 $\geq$ 10 Hz). In the following, we study the two groups separately. In the next section, we present the results of the detection without taking into account the auto-detections. We see that we gain information compared to the JMA catalog especially before the Mw7.3 foreshock.

3.5.1 Detections at low frequency.

The low frequency detections present a rather constant seismic rate of 0.63 evt/day until the 02/16 (figure 3.19, in green). After this date, the seismic rate is multiplied by more than 4 until the 02/26 when it gets back to the previous rate. After the Mw7.3 foreschock, there is a rather strong increase of the low frequency detection rate.
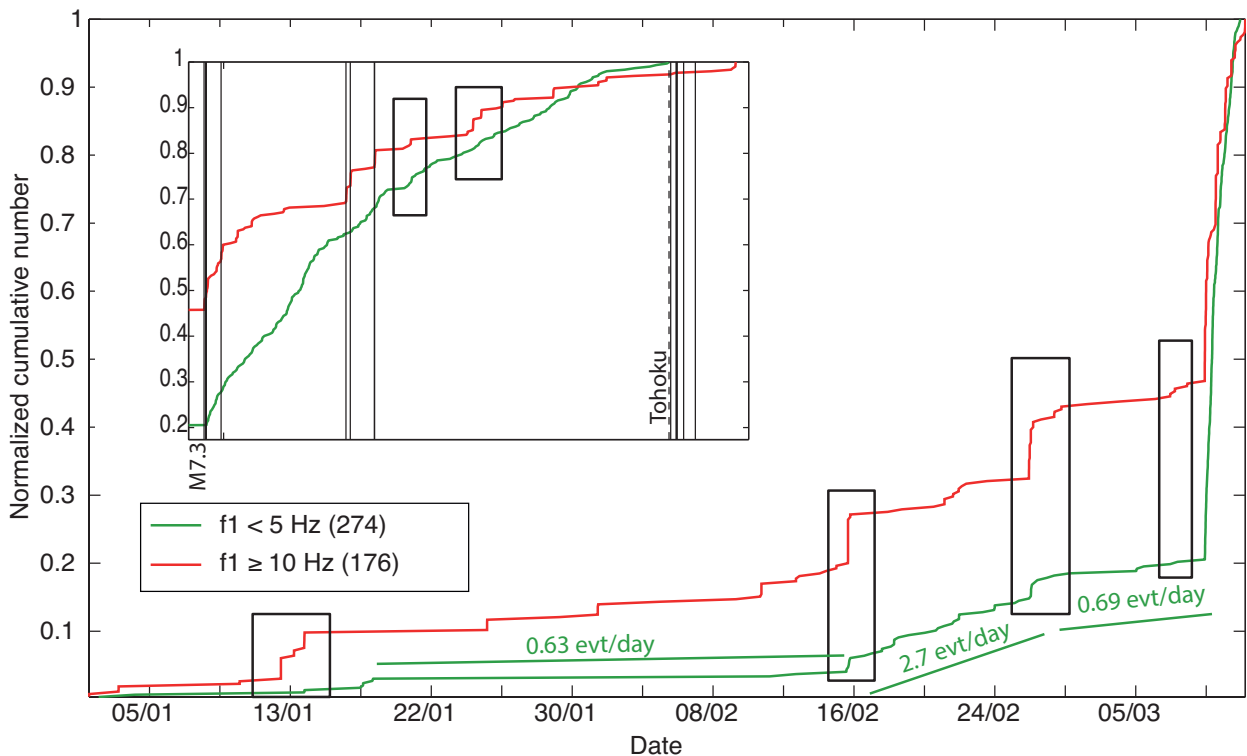
FIGURE 3.19 – Normalized cumulative number of the detected events with time (without auto-detections) separated in two groups : low frequency detections (green) vs high frequency detections (red), 45 detections have $5 < f1 < 10$ Hz and are not shown here. Inset : zoom on the period after the Mw7.3 foreshock. The vertical black lines indicate the time of occurrence of M$\geq$6 earthquakes and the dashed line indicates the Tohoku earthquake.

We computed the probability density function of the time interval seperating two detections of a same template for different bin intervals (figure 3.20). A slope of -1 indicates clustering and short-term correlation between detected events that follows the Omori's law. The events detected at low frequency (in green in figure 3.20) appear to follow a clustered process. Indeed, before the Mw7.3 foreschock, these events occurred

during the migration that takes place from the 2011/2/16 to the 2011/2/26 evidenced
by Kato et al. (2012). During the migration episode, the seismic rate is 4.3 times higher
than the pre- and post-migration rates that are around 0.65 events per day (figure 3.19).
We projected the detected events on a line parallel to the trench that crosses the Tohoku
earthquake epicenter (figure 3.21). This allows to follow the migration in time and space
(dashed line in figure 3.21). Apart from this migration, there is a small increase of seismic
activity on the 2011/1/18 due to a M4.1 earthquake that occurred nearby.
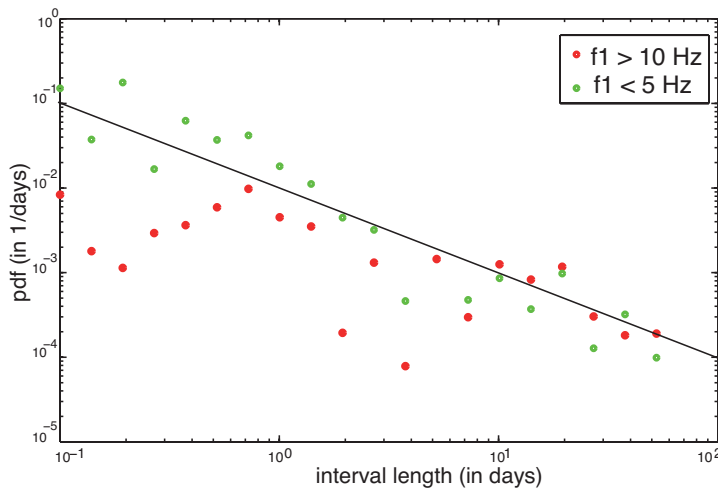
FIGURE 3.20 – Pdf of the time intervals between two detections of the same template
for low frequency detections (in green) and high frequency detections (in red). The black
line indicates a slope of -1.

A possible second migration episode might take place just before the Mw7.3 foreshock.
However, only a few events (5) occurred. This episode appears to stop on the 2011/3/8
and is followed by a quiescence that is ended by the Mw7.3 foreshock rupture.

After this earthquake, the events detected at low frequency present a constant rate
showing a rather smooth behavior only slighlty perturbed by the first burst on the
2011/3/10. The second migration observed by Kato et al. (2012) is indicated and is also
clearly seen by the low frequency detections. The M6 earthquakes do not seem to affect
the activity related to the events detected at low frequency.
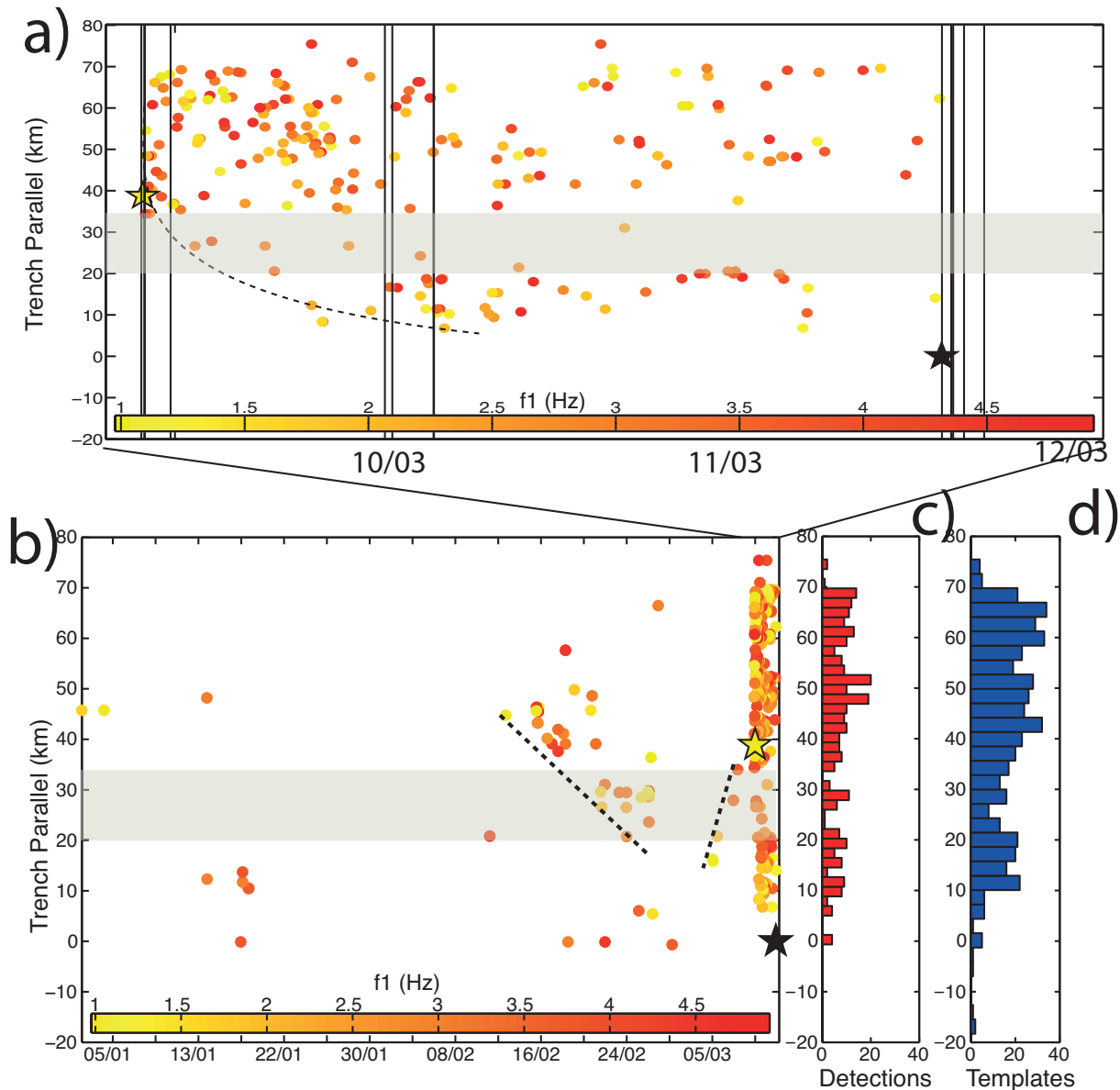
FIGURE 3.21 – Space-time diagram of events detected at low frequencies without the auto-detections. a) Space-time distribution of event detected at low frequencies. The color code gives f1 (in Hz). The earthquakes are located according to their distance along a line parallel to the trench axis. The yellow and black stars indicate the time of occurrence of the Mw7.3 foreshock and the Tohoku-oki earthquake, respectively. The first migration indentified by Kato et al. (2012) is indicated with a dashed line. The vertical black lines indicate the time of occurrence of M≥6 earthquakes and the dashed line indicates the Tohoku earthquake. b) zoom on the space-time diagram between the Mw7.3 foreshock and the 2011/3/12. The second migration indentified by Kato et al. (2012) is indicated with a dashed line. c) Number of detections along the trench parallel line. d) Number of templates along the trench parallel line.

3.5.2 Detections at high frequency.

The events detected at high frequency present a totally different dynamics. They occur during bursts of activity in between which the seismic rate is constant (figure 3.19, in red). The slope of the pdf in loglog scale is close to -1 with a flat first regime for time intervals inferior to one day. This suggests that the processus driving these events is less clustered than for the low frequency detections but non Poissonian. We computed the projection on the same line as we did for the events detected at low frequency and see that each burst extends over the entire zone from 15 to 70 km (figure 3.22). Also, the spatial distribution of events detected at high frequency is much less homogeneous than for events detected at low frequency. Indeed, there are six zones where high frequency detected events are activated several times. They are indicated by the red areas on figure 3.22. They are located in or near the rupture zones of M4.8 to M6.8 earthquakes.

Detections following the M4.8 to M6 earthquakes are spread over all the area, every time an $M \geq 6$ earthquake occurs (figure 3.22). There are also few bursts after the Mw7.3 foreshock that are not due to M6 activity. The main one occurred on the 2011/3/10, lasted 1.5 hours (from 4.26pm to 6pm) and contained 16 events and is concomittent with a magnitude 4.6 event followed by a magnitude 5.9. Since the high frequency events are mainly detected with the M4.8 to M6.8 templates, we ran the MDTM over year 2010 for the six templates that correspond to the six red areas in figure 3.22, to see whether or not the seismic activity did start on the 13 of Janurary 2011. In fact, it appears that a burst occurred on the 2010/11/30 after which there is an increase of high frequency detections until the Tohoku earthquake (figure 3.23). The largest earthquakes at depth (z>80km) between July and December 2010 occurred on the 2010/11/24 (M4.1) and on the 2010/12/31 (M3.5). At shallow (z≤40km) depth, the largest event that occurred in the epicentral area during the entire year of 2010 is on the 2011/12/10 (M3.8), followed in early 2011 by the 2011/1/6 (M3.6). This is consistent with an activation of the seismicity on November 2010.
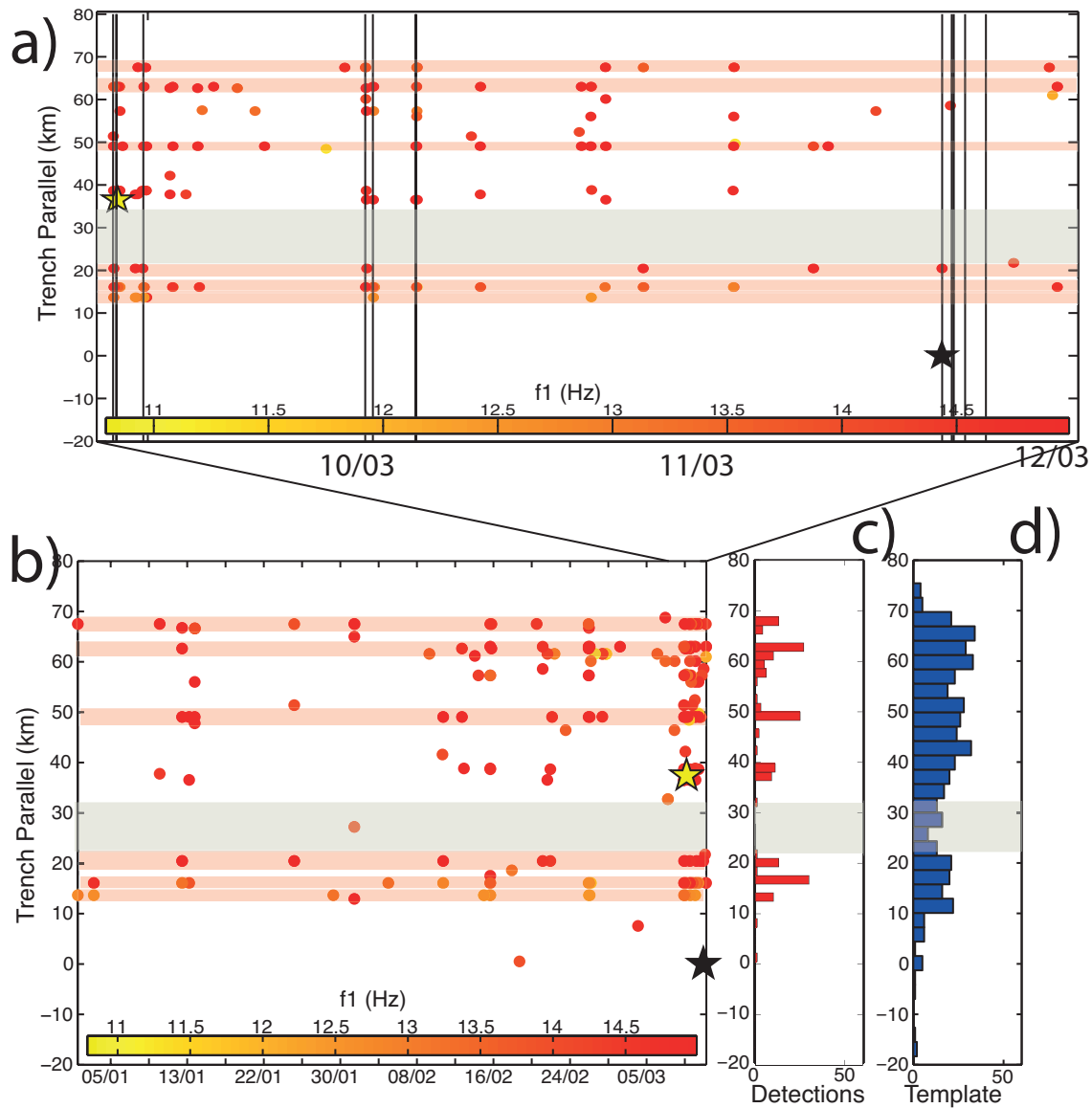
FIGURE 3.22 – Space-time diagram of events detected at high frequencies, without the auto-detections. The red areas locate the zones where high frequency detected events are activated several times and that correspond to the location of M4.8 to M6.8 templates. They are located on or near rupture zone of large events. See caption of figure 3.21 for more details.

The events detected at high frequency before November 2010 are not absent. We can
hypothesize that they are slip markers which implies that their number is proportionnal
to the cumulative slip. In fact, considering that the Mw7.3 foreshock triggered around
35 cm of postseismic slip (Ohta et al., 2012), we can see that 338 events detected at
high frequency were triggered in the meantime which gives a slip rate per event of
around 0.10 cm. Between January and November 2010, 62 events occurred including 45
in the area of maximum postseismic slip located between the Mw7.3 foreshock and the
Tohoku epicenters. This implies that 4.5 cm of slip occurred in the surrounding area.
This reasoning would yield an annual slip value of 4.9 cm/year. Thus, this zone would
not be fully coupled before the Tohoku earthquake. Indeed, with a convergence rate of
8.3 cm/year, we can estimate a coupling coefficient of only 42.5% with this method.
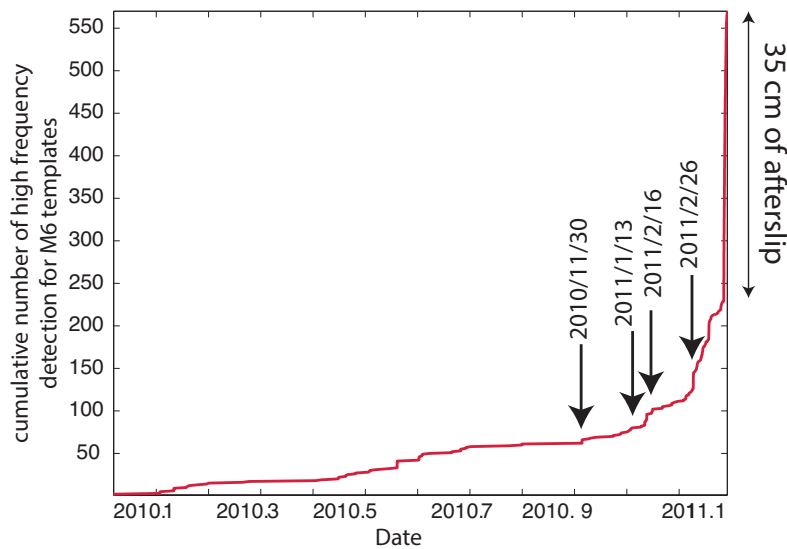
FIGURE 3.23 – Cumulative number of events for the high frequency detections from
2010/1/1 to March 2011 using the six M4.8 to M6 templates only.

With the MDTM algorithm, we detect events at both low and high frequency that
did not follow the same dynamic during the preparatory phase of the Tohoku earth-
quake even if they are located in the rupture area of the megathrust event. This implies
that two situtations occur : detections inside the future rupture zones of M4.8 to M6
earthquakes or outside. These two situations show two different behaviors : a relatively
smooth distribution in time and space using M2-3 templates (events detected at low
frequency) versus the M4.8 to M6 templates that detect at high frequency events that
occur as bursts and that are spatially correlated. However, a common feature to both

events detected at low and high frequency distributions in the space-time diagram is the presence of a weakly active band between 21 and 34 km (gray band on both figures 3.21 and 3.22).

Note that the detections we obtain with the method are dependent on the template locations. It allows to capture the dynamics of the zones where templates are. Here, we thus observe the behavior in the large earthquake rupture zones at ± 20 km from their epicenters, given the resolution of our method, but it is not excluded that other events occurred on the subducting slab.

Next section presents the history of the seismicity in the area before the megathrust event.

3.6 Discussion.

3.6.1 Detailed seismic history in the Tohoku rupture zone.

Three major earthquakes strucked the Tohoku-oki rupture area from the 1920s to
2003 : in 1958 (M6.7), 1978 (M7.4), and the M7.0 1981 earthquake (Sato et al. (2013),
figure 3.24).
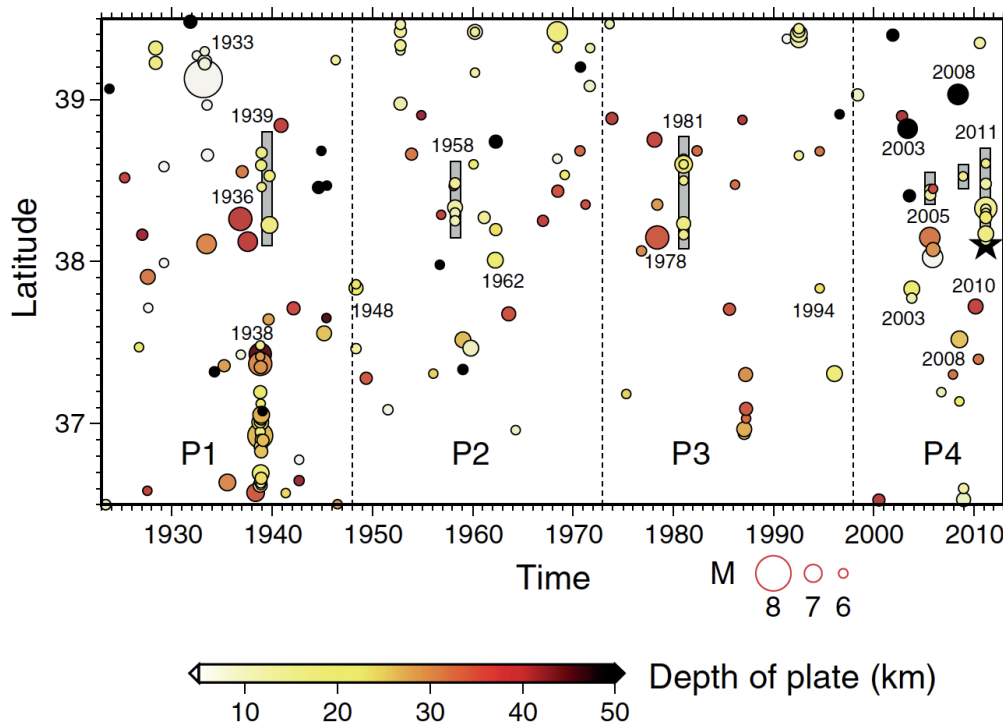
FIGURE 3.24 – Spatiotemporal distribution of events (M≥6.0) in the range of latitude
36.5^o˘39.5^o N and longitude 140.0^{o}145.5^o E. The bars indicate the prominent seismic
activity in the zone of shallow seismic activity. The star indicates the mainshock of the
2011 Tohoku-Oki earthquake. The events are shaded according to the depth of the upper
interface of the subducted Pacific plate beneath the epicenter of an event. The events
located on land are shown by black circles, from (Sato et al., 2013).

Their rupture zone is located in areas surrounding the large slip patch of the Tohoku
earthquake except for the 1981 event whose slip area is located in a region of relatively
slow slip of the Tohoku earthquake (Yamanaka and Kikuchi, 2004; Hasegawa and Yo-
shida, 2015). This suggests that the area that presents high co-seismic slip during the
Tohoku earthquake was locked throughout this period whereas the stress was at least

partially released in the surrounding zones. The seismic activity began to increase after 2003 when several M7 earthquakes occurred. During this period, the seismic coupling was not constant in the eastern Japanese subduction zone (Marsan et al. (2017), submitted). Indeed, inland GPS time series show changes in rate between 1998 and 2011 in the northern Tohoku, where they evidence an increase in slip deficit rate, and in south-central Tohoku, where they show a decrease of slip deficit rate (Mavrommatis et al. (2014); Yokota and Koketsu (2015), figure 3.2).

Postseismic slip of large events, in particular the 1994 Mw7.6 Sanriku and the 2003 Mw8.1 Tokaichi earthquakes, that occurred in the northern zone can explain such increase in slip deficit rate however, no postseismic effects can explain the decrease in the south. This suggests that a long-term aseismic slip of about ten year duration preceded the Tohoku earthquake. Smaller slow slip transient were evidenced using ocean bottom pressure gauges (Ito et al., 2013). Their analysis indicates that a slow slip transient occurred on the plate interface in 2008 with a duration of a week and a magnitude of 6.8.

At the end of 2010, the seismic rate of the events detected at high frequency increases after a burst-like episode on November 30th. The beginning of the preseismic phase at the end of 2010 is consistent with the seismic activity at shallow and greater depths. The future rupture zones of the M4.8 to M6.8 earthquakes are thus active from January 2010 and the seismic activity increases from November 2010 to their ruptures.

In mid-January, the deep seismicity increases, accompanied by a seismic burst at shallower depth (figure 3.25 a). During this period, the events were mainly detected at high frequency and occurred in three of the high frequency patches identified in figure 3.25 by grey diamonds. After this burst, only events detected at high frequencies occurred, mainly on the same patches. The fact that these small patches regularly break and that there is no activity in the grey band indicated in figures 3.21 and 3.22 strongly suggests the presence of an aseismic zone nearby (area delimited with the dashed line in figure 3.25).

The northern high frequency patches are located close to the sources of 5 VLFEs that occurred in 2007, 2009 and 2011 (Matsuzawa et al., 2015). The presence of VLFEs could be linked to the existence of a fluid layer in this area resulting in a high-intensity in seismic reflection (Fujie et al., 2002). These evidences point to a weakly coupled interface area. This is confirmed by the occurrence of a Slow Slip Event that occurred one month before the Tohoku earthquake accompanied by seismic activity and that reactivated the

2008 SSE patch (Ito et al. (2013), figure 3.25 b-f), although the spatial extent of this SSE patch is badly resolved. Note that no VLFEs were found in the aseismic zone delimited in figure 3.25.

Our observations confirm the migration episode of earthquakes from the 2011/2/13 to the 2011/2/16 (figure 3.25 b-f). The activity begins with a burst of events detected at high frequency which is followed by a maintained activity of events detected at low frequency mainly located close to the Mw7.3 foreshock epicenter, first to the north and then migrating to the south. This migration is only seen for the events detected at low frequency and occurs during the SSE. This sequence of events ended with a burst of high frequency detections on the 02/16. No events detected at low frequency occurred after this migrating sequence until another seismic activity increase from the 03/05 to the 07/03 that struck the downdip part of the studied area (figure 3.25 g).

Following this highly active period, the entire area experienced a quiescence that lasted 25 hours. We tested if this quiescence is an unusual feature during the period of study by calculating the number of events during periods of 25 hours chosen randomly from the 2011/1/1 to the 2011/3/6. It appears not unusual to have an absence of seismicity during such a duration. However, it is surprising that after such an intense seismic phase, nothing should happen before the Mw7.3 foreshock that is a major earthquake.

The loading of the area surrounding the Mw7.3 rupture zone by the SSE and recurrent transient slips in the aseismic zone resulted in increasing the stress state on the Mw7.3 asperity that eventually breaks after a quiescence of one day. The Mw7.3 foreshock occurred on the 2011/3/9 and mainly triggered aftershocks north of the epicenter. The postseismic slip is partly located in the south-west area between the epicenters of the foreshock and the Tohoku earthquake (Ohta et al. (2012) and figure 3.5) confirming the presence of an aseismic zone in this location.
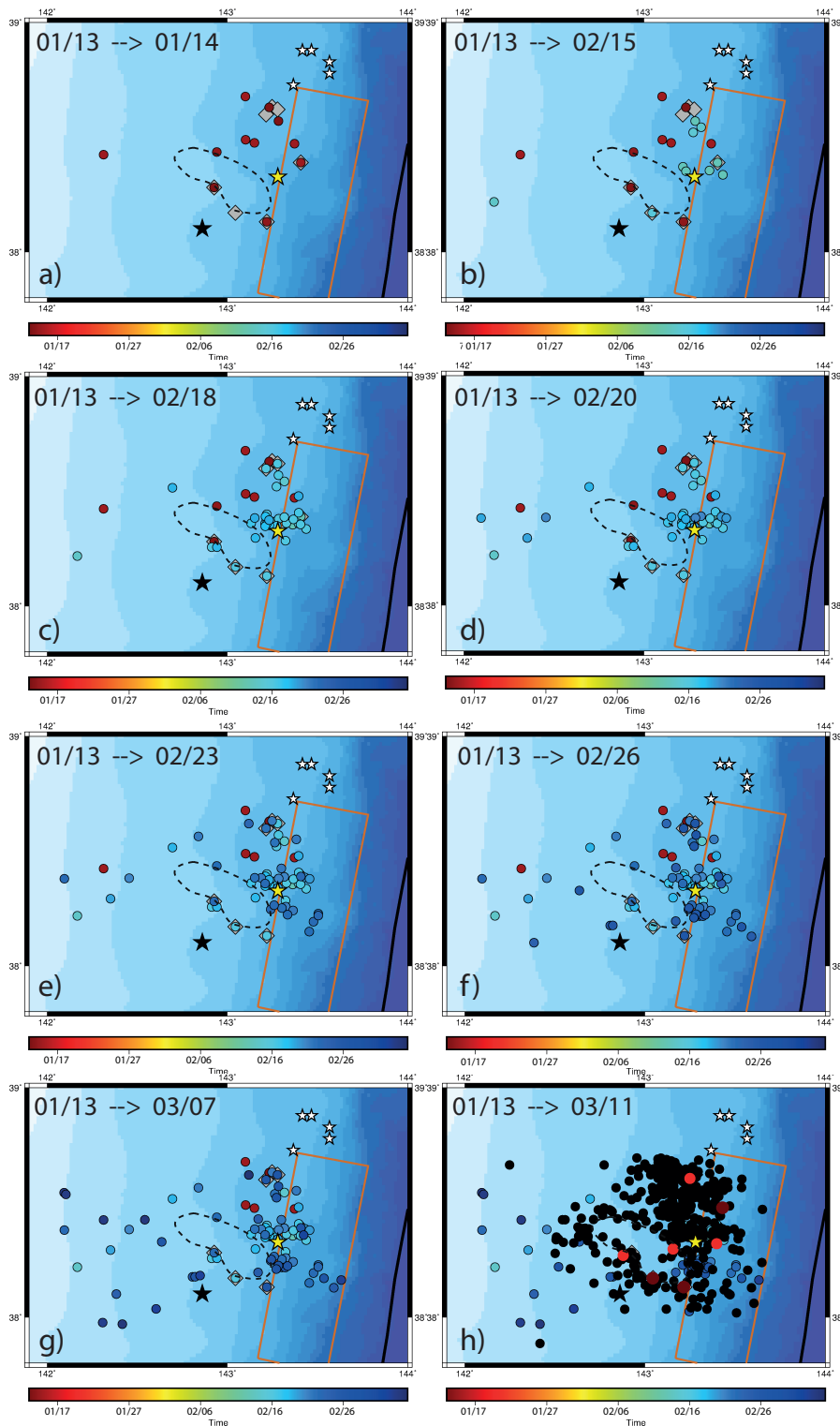
FIGURE 3.25 – Snapshots of the seismicity in the studied area. The slipping patch of the 2011 SSE is shown in orange (Ito et al., 2013). The epicenters of the Mw7.3 foreshock and the Tohoku-Oki earthquake are shown in yellow and black, respectively. White stars indicate the locations of VLFEs (Matsuzawa et al., 2015). The dashed line indicate the aseismic slip zone. The events are color coded according to their time of occurrence. On figure h) the red dots indicate the position of M≥4.8 earthquakes and the brown dots correspond to the templates that detected most of the high frequency events accounting for the detections from the 2010/1/1 to the 2011/3/11.

After its rupture, the main foreshock triggered both aseismic slip and aftershocks (Marsan and Enescu, 2012; Hino et al., 2014). There was a second migration episode to the south-west that started only seven hours after the foreshock. This migration along with the aseismic slip loaded the south-west side of the aseismic slip leading to three M6 aftershocks that occurred 16 and 18 hours after the Mw7.3 foreshock, on the patches of events detected at high frequency. The rupture zone of the M4.8 to M6.8 earthquakes located south to the aseismic patch were particularly active before the Tohoku earthquake (in brown in figure 3.25h). These large events produced their own aftershocks and thus provoked a cascade of ruptures close to the Tohoku earthquake asperity. Eventually, the Tohoku earthquake struck the area triggering numerous aftershocks out of the studied zone.

To sum up, using the MDTM algorithm we detect 465 new events from 2011/1/1 to 2011/3/12. These detected events can be separated in two groups : events detected at low frequency, mainly by small (M2-3) earthquakes, vs events detected at high frequency, mainly by large M4.8-6.8 earthquakes.

These two groups follow different behaviors with time :

- the events detected at low frequency evidence the migration episodes that occurred both before and after the Mw7.3 foreshock and do not present activity before the Mw7.3 apart from the migration.

- on the contrary, the events detected at high frequency occur as bursts and extend over the entire area. Using the M4.8 to M6.8 templates of the most active areas, we see that the events detected at high frequency are active during the entire year 2010 and that their seismic rate increases from November 2010 to the 2011/3/12. The area seems to be only partly coupled before the Tohoku earthquake.

3.6.2   Further improvements of the MDTM algorithm

The use of the MDTM algorithm is a first step towards detecting events well below noise level. Alternatively, the development of other array-based techniques to better characterize the noise sources can help denoising the continuous signal. This is the case for the MRABF (Multirate Adaptive Beamforming) technique developed for underwater acoustics by Cox (2000). This technique locates weak noise sources that are hidden by stronger sources. The method is similar to the one we applied above except that it aims to cancel the wave field of the stronger sources, and thus to focus on smaller (noise)

sources. To do so, we apply an orthogonal projection to the data matrix to cancel the dominant interferences. We apply the projector $I - v_m v_m^*$ to the data $d(\omega)$:

$$Z(\omega) = [I - v_m v_m^*] \, d(\omega), \tag{3.9}$$

where I is the identity matrix and v is the eigenvector as previously defined. The use of the MRABF technique requires phase coherency among the different stations of the network to allow weak source detection. The frequency band of interest depends on the average interstation distance. Thus, this technique can not be used with the Hi-net network as the stations are too far from each other (from 12 to 91 km apart) and the frequency of interest (from 0.2 to 4 Hz) is too small compared to the instrumental frequency cutting which is of 1 Hz (figure 3.26). We therefore tested this method on the Tono array managed by the Tohoku University (Iwasaki et al., 1994). It is located north of the Tohoku prefecture, in a region characterized by granite hard rock and it contains 10 stations with an array aperture of 10 km. The Rayleigh wave speed in this area is about 3 km/s (Takagi et al., 2014). Thus, the wavelength that we want to study is comprised between 70 and 1 300 m.

Between 0.2 and 4 Hz, the coherency between stations is higher for the Tono array than the Hi-net stations selected (figure 3.26). The coherency between the stations in the Tono array is even higher at lower frequency range (between 0.05 and 4 Hz) indicating that its use is better suited to noise analysis. We test the method by applying it on the 21st of February 2011 when we detected 12 events using the MDTM algorithm. We focused on a part of this day, from 10 to 10.30am.

The signals are first whitened, giving the same weight to all the frequencies. We then average the CSDM to obtain a full-rank matrix by modifying equation 3.1 as :

$$K(\omega) = \frac{1}{M} \sum_{i=1}^{M} D_i(\omega) D_i^*(\omega) = \frac{1}{M} \sum_{i=1}^{M} K_i(\omega), \tag{3.10}$$

where $D_i(\omega)$ is the data vector of the different noise subsegments. As presented in Chmiel et al. (2016), several noise segments M are needed, with M equals at least to twice the number of receivers N present in the array. Here, we use windows that have a duration of 20 seconds and an overlap of 3 seconds over the entire day of 2011/2/21, thus 1401 segments. The technique defines the continuous signal in a space (the noise signal) and a subspace signal (the potential seismic events hidden by the noise), corresponding to the
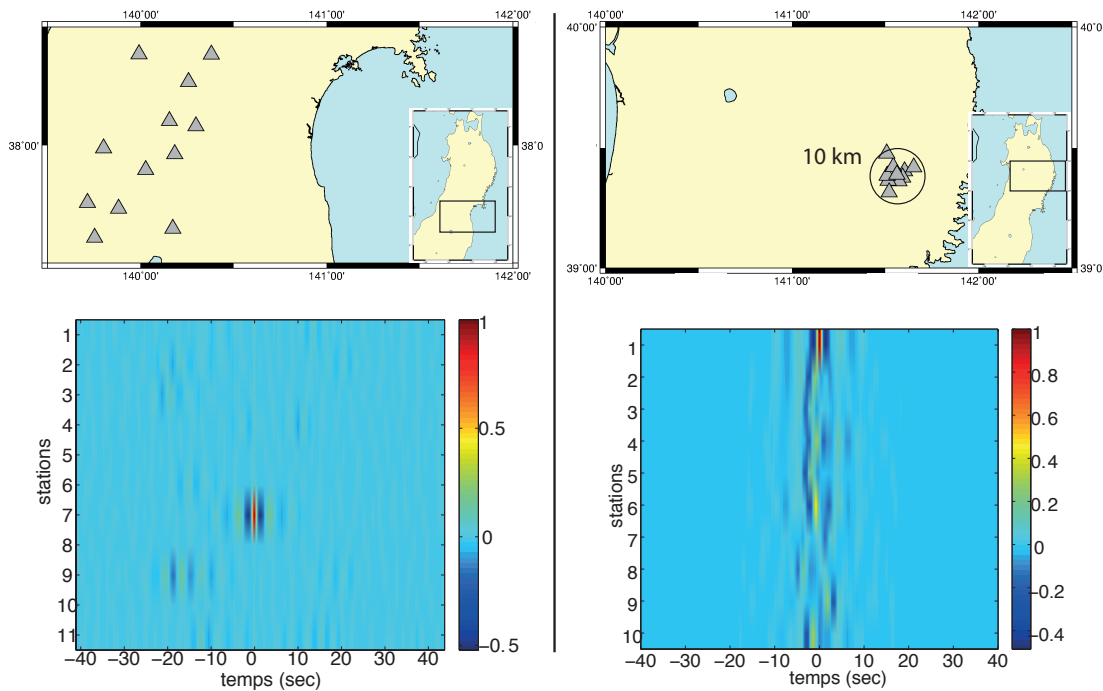
FIGURE 3.26 – Top : Location of the stations used in the MRABF method. On the left,
we map Hi-net stations that we tested as an array. On the right, we map the Tono array.
The black circle has a radius of 10 km. Bottom : coherency between the stations of the
two arrays computed on ambient noise between 0.2 and 4 Hz with station 7 and station
1 as references for the Hi-net and Tono arrays, respectively.

rest of the signal that we want to retrieve (figure 3.27). The signal space corresponds to
the principal components of the matrix K and the subspace is defined by the orthogonal
components of the matrix K.

Then we observe the output signals after removal of either the principal or orthogonal
components (figure 3.28). We see that the method decreases the noise amplitude and that
different arrivals can be detected on the orthogonal components, thus, after denoising.

We can analyze the event in the black rectangle in figure 3.28. We see that the signals
are small and not well recorded at every station (figure 3.29). Contrary to the MDTM
method, here, we keep track of absolute time since we observe eigen vectors of the signal
itself. It is thus possible to propose an order of detection of the source, though the time
of arrival is not clear for certain stations (with an interrogation mark).

The source seems to be located offshore and could thus come from the rupture zone
of the Tohoku earthquake.
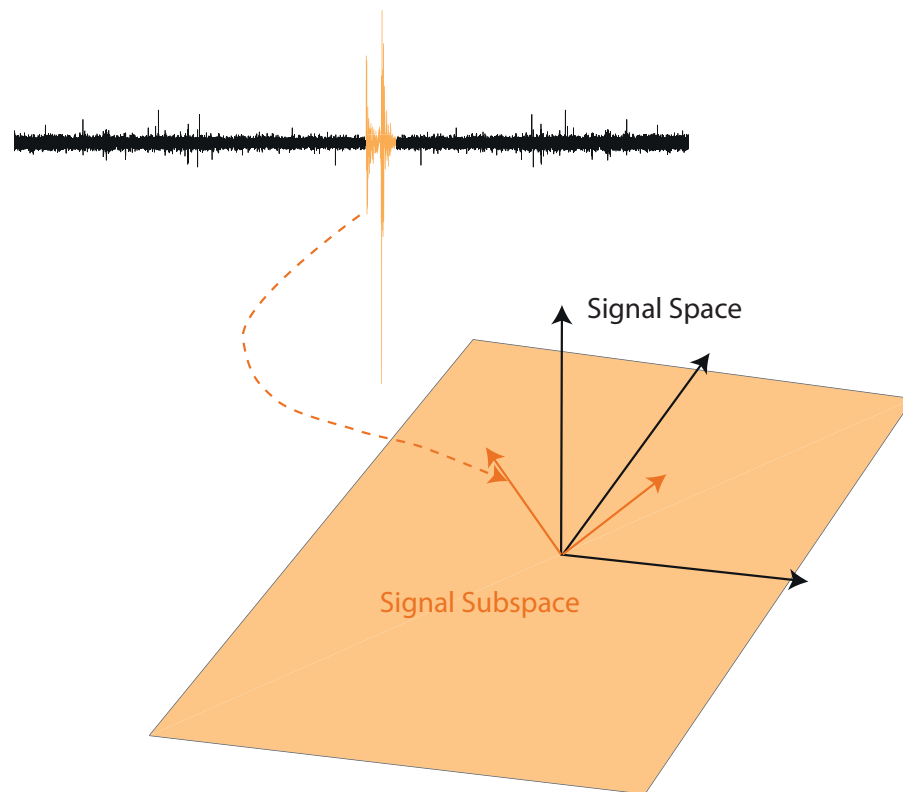
FIGURE 3.27 – The technique used here separates the signal into a signal space (in black) and subspace (in brown). In this study, the signal space corresponds to the principal components of the matrix K which are the noise that is coherent between the stations. The subspace signal corresponds to the orthogonal components of the matrix K and defines the signal after denoising, modified from (Harris, 2006).

Although the method allows to denoise the continuous signal, it needs further tests to be improved especially during other times of detections that we made using the MDTM algorithm, before being applied to the continuous data.

3.7 Conclusion.

The MDTM algorithm detects small events hidden in the noise that might be produced by transient slips. This allows to fully capture details on the seismic activity during the preseismic phase of the Tohoku-Oki earthquake. Two episodes of migration were evidenced by the events detected at low frequency, one from the 02/16 to the 02/26 and the second one after the Mw7.3. The seismic activity of the events detected at low frequency is very low apart from these two episodes. On the contrary, the analysis of the
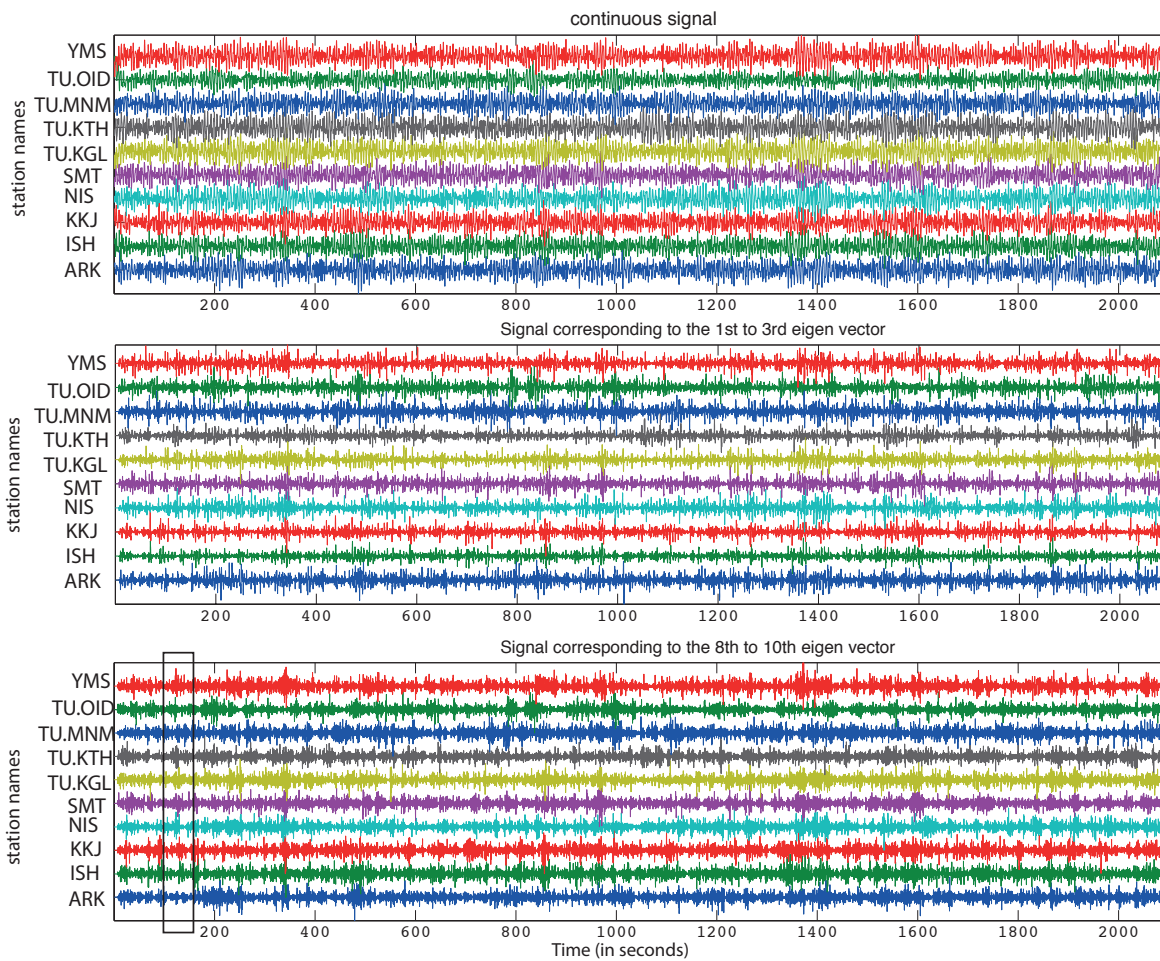
FIGURE 3.28 – Top : Continuous signal, middle : signal corresponding to the first three eigen vectors ; bottom : signal corresponding to the 8th to 10th eigen vectors. All the waveforms are normalized by their maximum amplitude.

events detected at high frequency suggests that the preparatory phase started on the 2010/11/30 with a burst-like seismicity and an increase of the activity until the Tohoku earthquake. The increases of the number of events detected at high frequency is marked by several burst-like episodes. These events are located on the rupture area of the M4.8 to M6.8 earthquakes (especially south to the aseismic zone) that occurred before the Tohoku earthquake. These rupture zones were thus highly active during the entire preseismic phase, especially during burst-like episodes that affected the entire area, likely triggered by aseismic slip. This aseismic slip is located north to the M6 rupture zones and interacted with the seismic migration episode since bursts of events detected at high frequency occurred both at the beginning and at the end of the SSE. We thus evidence
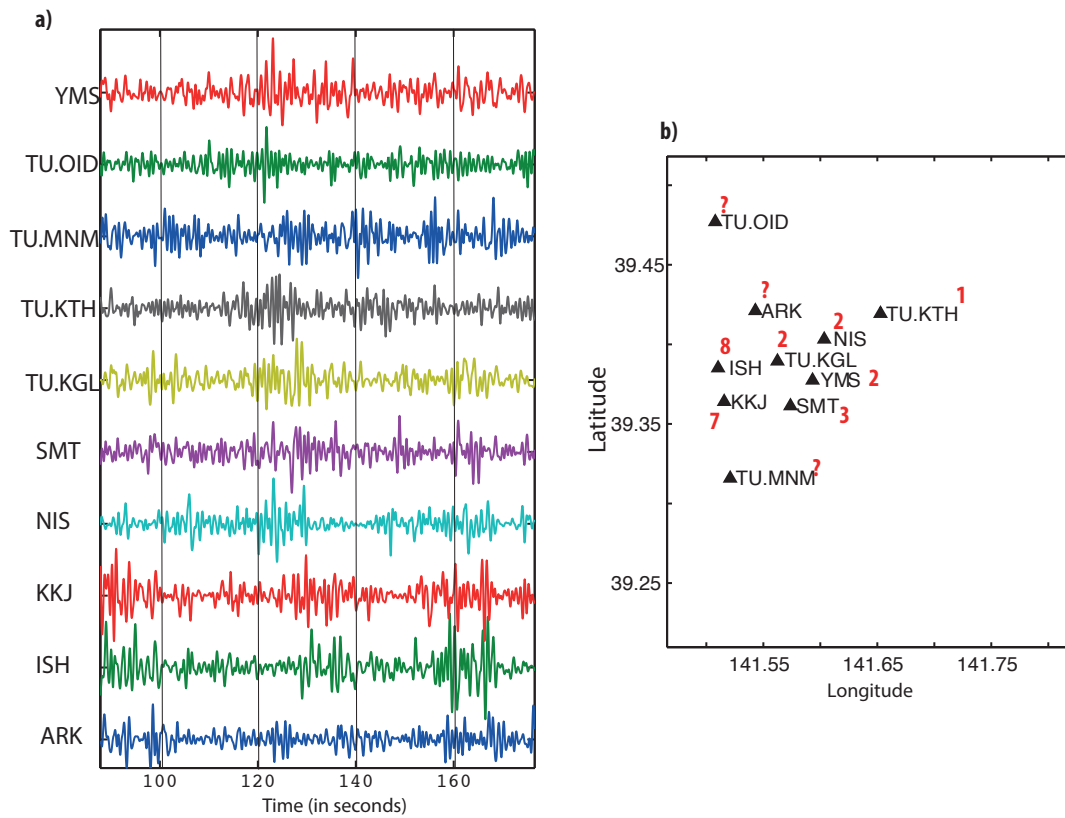
FIGURE 3.29 – a) zoom in the trace corresponding to the 8th to 10th eigen vectors at the time of a detection we made with the MDTM method. The names of the stations in the Tono array are given on the left of the traces. b) Zoom on the location map of the stations in the Tono array. The numbers (or interrogation marks by default) indicate the order of time of arrival for the seismic wave shown in a).

deformations episodes on a wide zone alternating with seismicity before the Tohoku earthquake. The MDTM algorithm could be combined with a denoising preprocessing of the continuous data thus enhancing even more the signal to noise ratio.

Chapitre 4

A new history of Slow Slip Events in Boso Peninsula, Japan.

4.1 Foreword

In this chapter, we focus on the interactions between seismic and aseismic slip during a slow rupture which is a Slow Slip Event. The seismic cycle of such event differs from the one of regular rapid earthquake in the sense that it does not present a nucleation phase nor a postseismic phase (figure 4.1). Furthermore, strain release during such event is much smaller than during regular earthquakes. The Slow Slip Events might be accompanied by burst-like seismic activity (figure 3.1) but it is not always the case. They are well detected by the use of geodetic data since they provoke a displacement at surface opposite to the plate motion direction (figure 4.1 bottom). We present the case of the Boso Slow Slip Event.

This area is well known for the occurrence of several slow slip events (SSE) along the top interface of PHS at shallow depth (between 10 and 30 km), in 1983, 1990 (identified by assuming an earthquake swarm as a proxy for slow slip episode off Boso, Hirose et al. (2012)), 1996, 2002, 2007, October 2011 and 2014 that have a clear signature on geodetic measurements and have a moment magnitude between 6.4 and 6.6 and rupture the same characteristic patch (Ozawa et al., 2003; Sagiya, 2004; Hirose et al., 2012, 2014).

Furthermore, the SSE occur close to the M7.9 Kanto earthquake that struck the area in 1923. This area currently presents high negative deficit rate suggesting an intense coupling of the asperity that broke in 1923 and that lies directly below Tokyo metropolitan
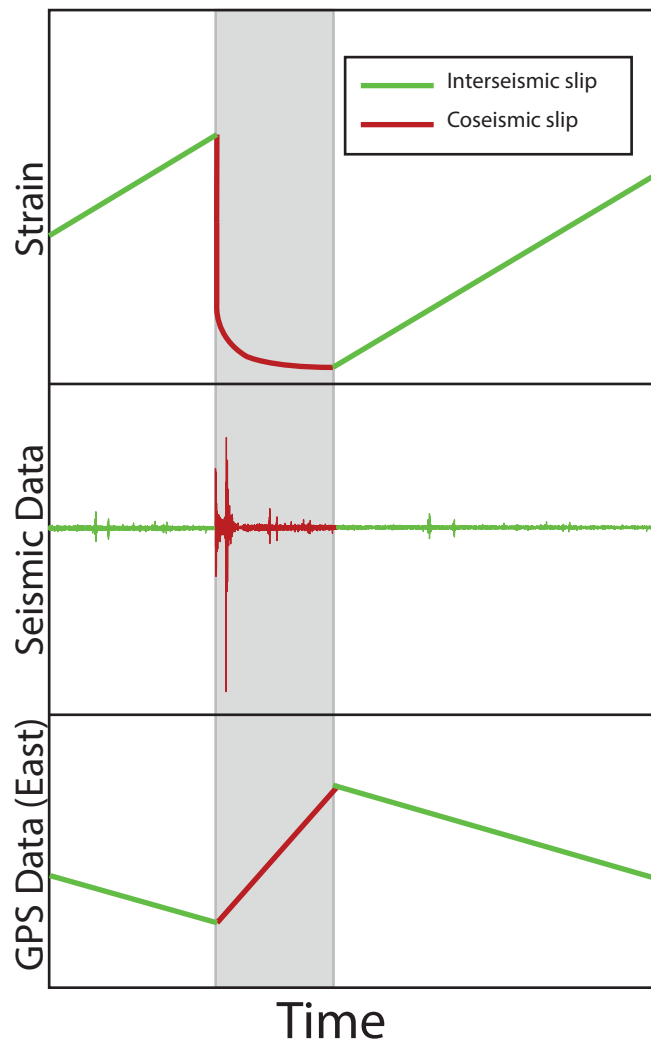
FIGURE 4.1 – The seismic cycle of a slow slip event. Top : evolution of strain with time during the seismic cycle. Middle : example of a seismic waveform that represents events occurring simultaneously to a slow slip events. Bottom : displacement at surface recorded with GPS, along the East component. The direction of the displacement during the SSE is opposite to the interseismic displacement. In this chapter, we focus on the coseismic phase of a SSE that can last several days to several weeks.

area (figure 4.2, Noda et al. (2013)). It is thus vital to fully understand the slip history in this area and the interactions between the SSEs and the surrounding seismicity. The SSEs on Boso Peninsula have always been accompanied by swarm-like seismicity located at the northern downdip edge of the slow slip patch (Ozawa et al., 2007; Hirose et al.,
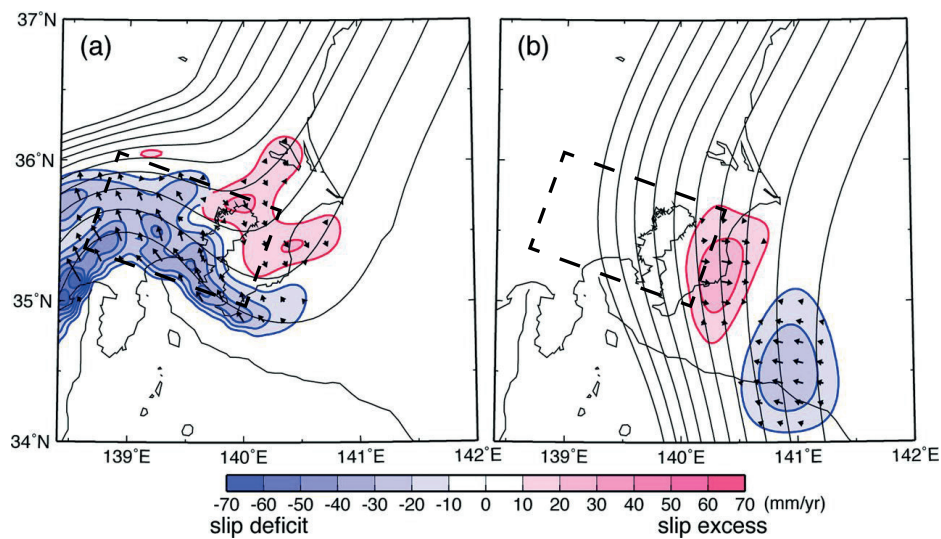
FIGURE 4.2 – The slip-deficit rate distribution inverted from GPS strain rate data. (a) The NAM-PHS plate interface. (b) The PHS-PAC plate interface. The blue and red contours show slip-deficit and -excess rates at intervals of $10\,\text{mm yr}{-1}$, respectively. The thick arrows indicate slip-rate vectors on each plate interface (modified from Noda et al. (2013)). The black rectangle indicates a model source region of the 1923 Kanto earthquake by Wald and Somerville (1995).

2012), triggered by the stress released during the SSEs (Hirose et al., 2014). This indicates the possible presence of Repeating Earthquakes in the area since, as we presented in Chapter 1, the occurrence of a slip event triggers repeating ruptures of the same asperity.

The study of the REs in this area allowed to detect two transient episodes that occurred in 2005 and 2010 and that were not seen in the geodetic data so far. The application of a new method to analyze the GPS data confirmed an event in 2005 seen by only one station and another one in 2010 seen by all 9 studied stations. This work will be submitted to the Journal of Geophysical Research : Solid Earth.

4.2   Abstract

We analyse the seismic waveforms of more than 2,900 events (M$\geq$ 1.0) that occurred in the Boso Peninsula, Japan from 2004/04/01 to 2015/11/04 calculating the correlation and the coherence between each pair of events in order to define groups of repeating earthquakes. Analyzing the cumulative number of repeating earthquakes, we discover two slow slip events that were unkown so far. This result is confirmed by the analysis of GPS data with a new method that allows to see the slight changes present in the time series. We also analyze the interaction of the repeating earthquakes that occurred during one or more SSE(s). This work brings new insights on the plate behavior and demonstrates that the SSEs in Boso area present a more complex history than previously considered.

4.3   Introduction

The Boso Peninsula, Japan, is located on the Okhotsk plate above two subducting slabs : the Pacific (PAC) plate plunges westward at depth, with the Philippine sea plate (PHS) subducting to the west-northwest just above it (Figure 1). This area is well known for the occurrence of several slow slip events (SSE) along the top interface of PHS at shallow depth (between 10 and 30 km), in 1983, 1990, 1996, 2002, 2007, October 2011 and 2014 that have a clear signature on geodetic measurements and have a moment magnitude between 6.4 and 6.6 and rupture the same characteristic patch (Ozawa et al., 2003; Sagiya, 2004; Hirose et al., 2012, 2014). The SSEs on Boso Peninsula have always been accompanied by swarm-like seismicity located at the northern downdip edge of the slow slip patch (Ozawa et al., 2007; Hirose et al., 2012), triggered by the stress released during the SSEs (Hirose et al., 2014).

A first estimation of the recurrence interval of these transients was 4 to 7 years since 1983 (Hirose et al., 2012). However, the recurrence interval tends to decrease from 6.4 to 2.2 years from 1996 to 2014 (Ozawa, 2014). This shortening being possibly a by-product of a long-term acceleration in loading rate (Reverso et al., 2016). Furthermore, Boso area is located at the southern end of the Tohoku-oki rupture and was sensitive to stress perturbation caused by the megathrust earthquake since a SSE occurred only three days (Kato et al., 2014) and few months after it (Hirose et al., 2012).

It is necessary to better constrain the slip history of this area since modelizations show that the recurrence intervals become shorter when closer to a large interplate earthquake

FIGURE 4.3 – Tectonic settings of Boso Peninsula. The brown triangles and red dots give the location of the seismic and GPS stations, respectively, used in this study. We analyse Repeating Earthquakes occuring in the black rectangle, which contains most swarm-like seismicity triggered during known SSEs. The broken lines show the depth contours of the plate interface of the PHS (Ishida, 1992).

nearby (Matsuzawa et al., 2010; Mitsui, 2015). Are there smaller SSEs in Boso area or are the SSEs really characteristic ? Are the SSEs always triggered because of the accumulation of a slip deficit with time (Sagiya, 2004; Nishimura et al., 2007; Reverso et al., 2016) ? To answer these fundamental questions we look at Repeating Earthquakes activity. We analyse their distributions in time and space. We also analyse GPS data removing seasonal signals, the trend and the common mode. The combination of these observations allows to identify two unknown SSEs that are smaller in magnitude and/or lateral extension than the already known ones.

4.4   Data and Methods

4.4.1   GPS data analysis

4.4.1.1   Daily cGPS processing.

The data of the GPS Earth Observation NETwork in Japan (GEONet), together with 44 IGS sites worldwide (International GNSS Service for Geodynamics, `http://igscb.nasa.jpl.org`), were processed over the period 1994-2013 following a double differences approach. Each day, the data set was divided into sub-networks of 40 stations including two tie stations near the middle of each subnetwork and no station used more than twice (for example, for day 365 of year 2009, we have 34 subnetworks for 1385 stations included in the processing). 24-hour sessions were reduced to daily estimates of station positions using the GAMIT 10.6 software (Herring et al., 2015), choosing the ionosphere-free combination, and fixing the ambiguities to integer values. We use precise orbits from the International GNSS Service for Geodynamics, precise EOPs from the IERS bulletin B, IGS tables to describe the phase centers of the antennas, FES2004 ocean-tidal loading corrections, as well as atmospheric loading corrections (tidal and non-tidal). We estimated one tropospheric zenith delay parameter every two hours and one couple of horizontal tropospheric gradients per 24h session, using the Vienna Mapping Function (VMF1, Boehm et al. (2006)), to map the tropospheric delay in zenithal direction, with a priori ZHD evaluated from pressure and temperature values from the VMF1 grids. Daily solutions were combined using the GLOBK software in a "regional stabilization" approach. Coordinate time series were then generated, and mapped into the ITRF2014 reference frame (Altamimi et al., 2016) by applying Helmert transforms to adjust IGS stations coordinates to those defined in the ITRF in a least square iterative process.

4.4.1.2   Time series analysis and identification of transient movements.

To study transient deformation in the area of Boso, in order to avoid major co-seismic offsets in our time series, we selected data from August 9th, 2004 until March 10th, 2011. Annual and semi-annual signals were removed from the time series, as well as the long-term constant deformation associated with interseismic loading, by fitting a linear regression together with a pair of sinusoids terms. Jumps associated with documented equipment changes were also estimated. 46 stable stations (ie. not affected by local transient signal), located within a distance range of 50-150km from the Boso SSEs'

source region, were used to calculate and remove the regional common-mode noise. This procedure reduced significantly the scatter in our time series. In order to image transient signals present in our time series, we computed the average velocity variations of the obtained detrended and de-noised time-series, by fitting a linear regression in a 15-day sliding window.

4.4.2   Repeating Earthquakes analysis

Repeating earthquakes (REs) are earthquakes that break a common asperity with nearly identical rupture lengths. These particular seismic events have been identified in California, most notably on the Parkfield segment of the San Andreas Fault (Nadeau et al., 1995), in Japan (Matsuzawa et al., 2002), including the Kanto region (Kimura et al., 2006; Gardonio et al., 2015), as well as other parts of the world (e.g., Chen et al. (2007); Bouchon et al. (2011)). REs have been hypothesized to be driven by the surrounding aseismic slip (Ellsworth and Beroza, 1995; Nadeau and McEvilly, 1999; Igarashi et al., 2003). Thus, they can be used to assess changes in creeping rate. In Boso, REs have been studied after the Tohoku-oki earthquake to evidence the existence of a SSE in March, two days after the megathrust earthquake (Kato et al., 2014).

We analyze the waveforms of all $M \geq 1.0$, $z < 60$ km earthquakes from April 2004 to November 2015, that are located in the Boso area ($35.51 \geq$ lat ≥ 35.15 and $140.70 \geq$ lon≥ 140.18) as listed in the JMA catalog. In total, we study 2986 earthquakes over 13 stations (figure 4.3), ellaborating on the method developed in Got et al. (1994), Lengliné and Marsan (2009) and applied in Gardonio et al. (2015). We compute both the mean coherency and the cross-correlation between all pairs of earthquakes at common stations for several frequency bands (1-4, 3-12, 5-20, 7-28, 9-36 and 11-44Hz) on a 512 sample-long window initially centered on the P-wave arrival. We keep the frequency band that gives the highest coherence and cross-correlation values. The coherency is defined as the smoothed cross-spectrum normalized by the smoothed autospectra of each signal. Time delays are also computed in the same frequency bands using both coherency and cross-correlation. They are estimated at $\pm$ 0.005 s which corresponds to an error of 35 meters at a wave velocity of 7 km/s. We then select all earthquake pairs characterized by a mean coherency greater than 0.99 for at least one station. In order to remove outliers, we reject time delays that differ by more than 0.01 s (one sample) when comparing time delays based on both coherency and correlation. The time delays are then used to compute the relative coordinates of all the earthquakes within a group of multiplets (Got et al., 1994;

Got and Okubo, 2003). We use the NIED (National Research Institute for Earth Science and Disaster Prevention) velocity model and the NonLinLoc algorithm (Lomax et al., 2009) to compute the P wave arrival time, the azimuth and the take-off angle of every event. For two earthquakes to be repeating instances of a nearly identical rupture, we require $d < \max\{L_1, L_2\}$ with d, the distance between the two events and L_1, L_2 their rupture radii, calculated with $L = (7Mo/16\Delta\sigma)^{1/3}$ (Eshelby, 1957), for a $\Delta\sigma = 30$ bar stress drop. We tested different values of stress drop (0.03, 3 and 300 bars). The stress drop value has a consequence on the total number of REs (608, 461, 159 respectively) which decreases when the stress drop increases (figure 4.4).
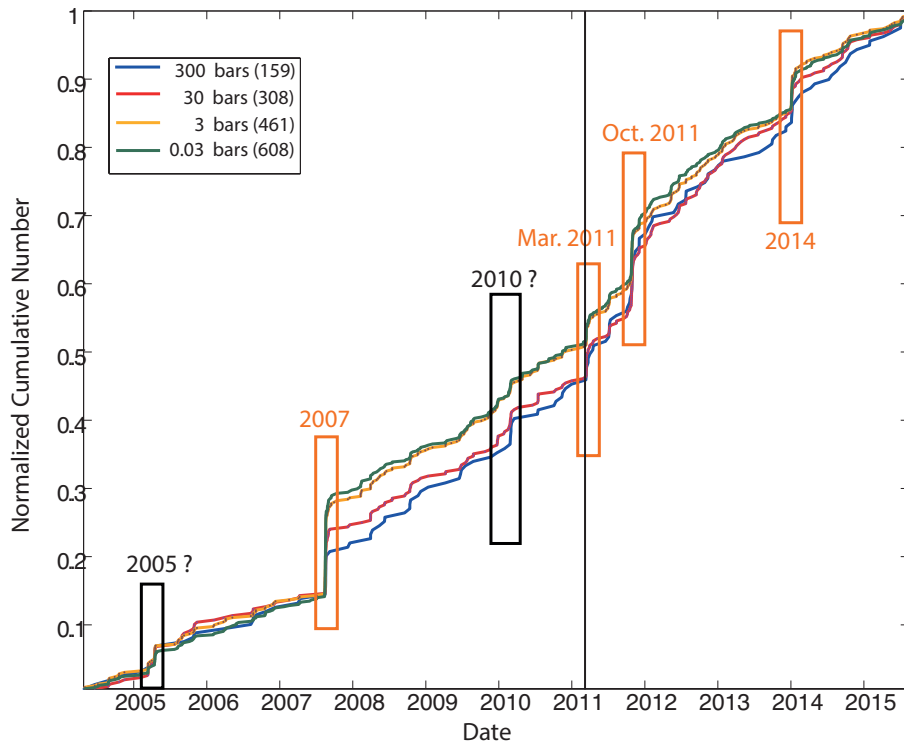
FIGURE 4.4 – Normalized cumulative number of REs on PAC and PHS depending on the stress drop value used to calculate the rupture radii. The total number is given in the brackets in the legend. The trend is independent of the stress drop. Only the number of REs is affected by the value of the stress drop (see text for more details).

At a low stress drop, the rupture areas are large, thus more events are gathered in a group than at a higher stress drop where the rupture size is smaller. The cumulative number of REs are very similar (figure 4.4).

In this study, we do not impose any criterion on magnitude. We finally group together all pairs of REs that share a common earthquake. An example of a group of REs is shown in figure 4.5.
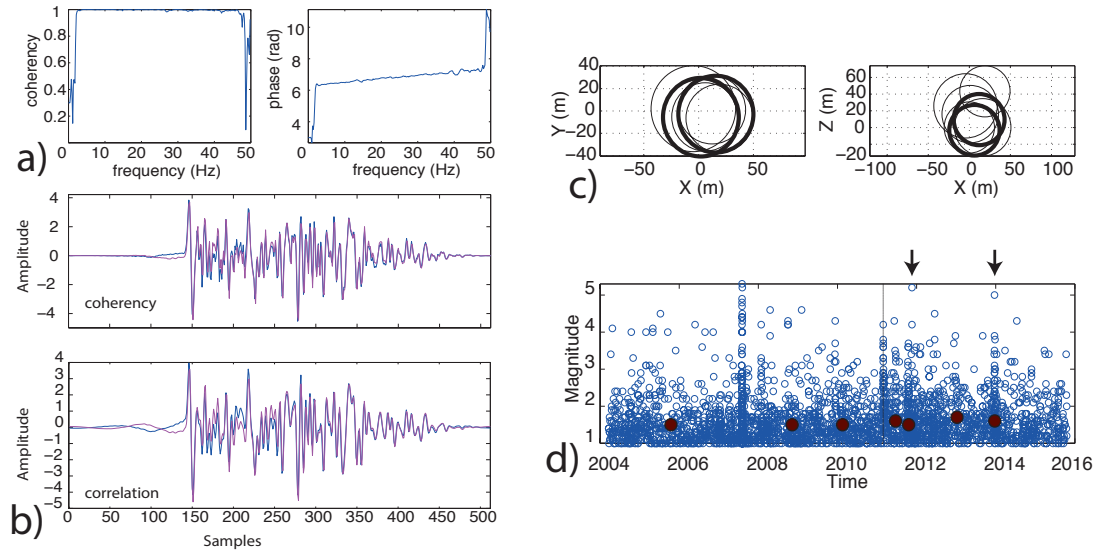
FIGURE 4.5 – Example of the detection of a pair of repeating earthquakes. (a) Coherency and phase vs frequency. b) Comparison of time-shifted waveforms, according to either the coherency or the correlation analysis. c) Relative relocation of the two events in their RE group that counts seven repeats. The two events of (a) and (b) are shown with bold lines d) Time of occurrence of the events in this group, the two events of (a) and (b) are shown with arrows. They occurred during two known SSEs (in 2011 and 2014).

The numbers of earthquakes and of REs increase during known SSEs (figure 4.6), as well as few days after the Tohoku-oki earthquake (Kato et al., 2014). Additionnally, the rate of REs shows two increases in 2005 and 2010. These are suspected, smaller instances of SSEs, that we further investigate now.
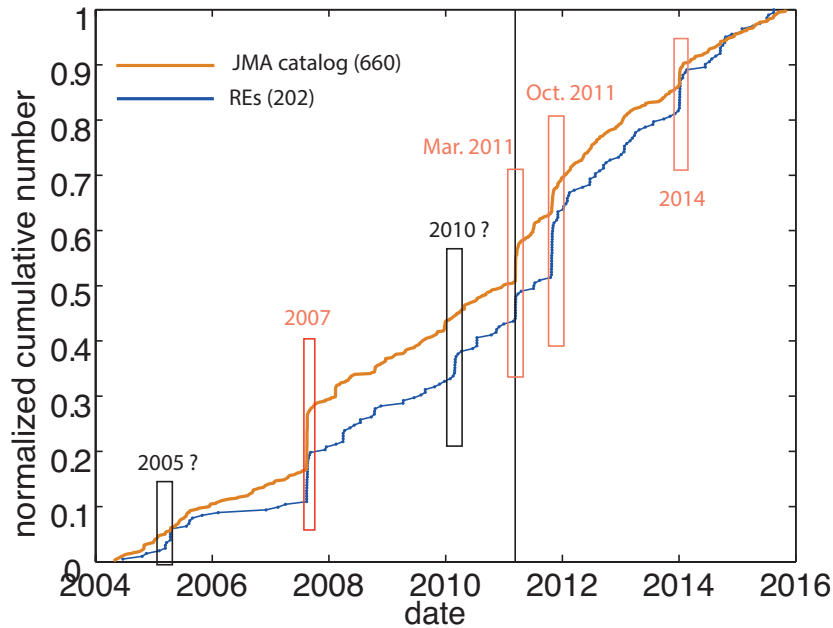
FIGURE 4.6 – Normalized cumulative global seismicity in the Boso area (magnitude 2 and greater, in orange) and normalized cumulative number of REs (in blue). The total number is given in the brackets in the legend. The timing of known SSEs is shown with red rectangles, and can clearly be seen in the raw seismicity and REs data. If an asperity is active several times during a known or suspected SSE, we kept only the biggest event of the group. The suspected SSEs in 2005 and 2010 are outlined with black lines, and can only be seen on the repeating earthquake activity.

4.5 Slip processes and repeating earthquakes analysis.

We separate the groups of REs according to their depths to allocate them to PHS or PAC. For all known SSEs (in 2007, October 2011 and 2014), REs are almost only seen on PHS (figure 4.7).

The time series after the 2011 Tohoku-oki earthquake likely involves also a direct co-seismic effect, as well as post-seismic slip on PAC, so that the March 2011 SSE is mixed with high RE rates caused by more than local slip on the PHS-NAM interface. The episode of high rate in 2005 is made of two short bursts (figure 4.7b), the first on the 2005/3/12 (on PHS only) contains 5 REs and the second in 2005/4/13 that also presents 5 REs and which is rapidly followed by a burst of three REs on PAc on the 2005/4/16.
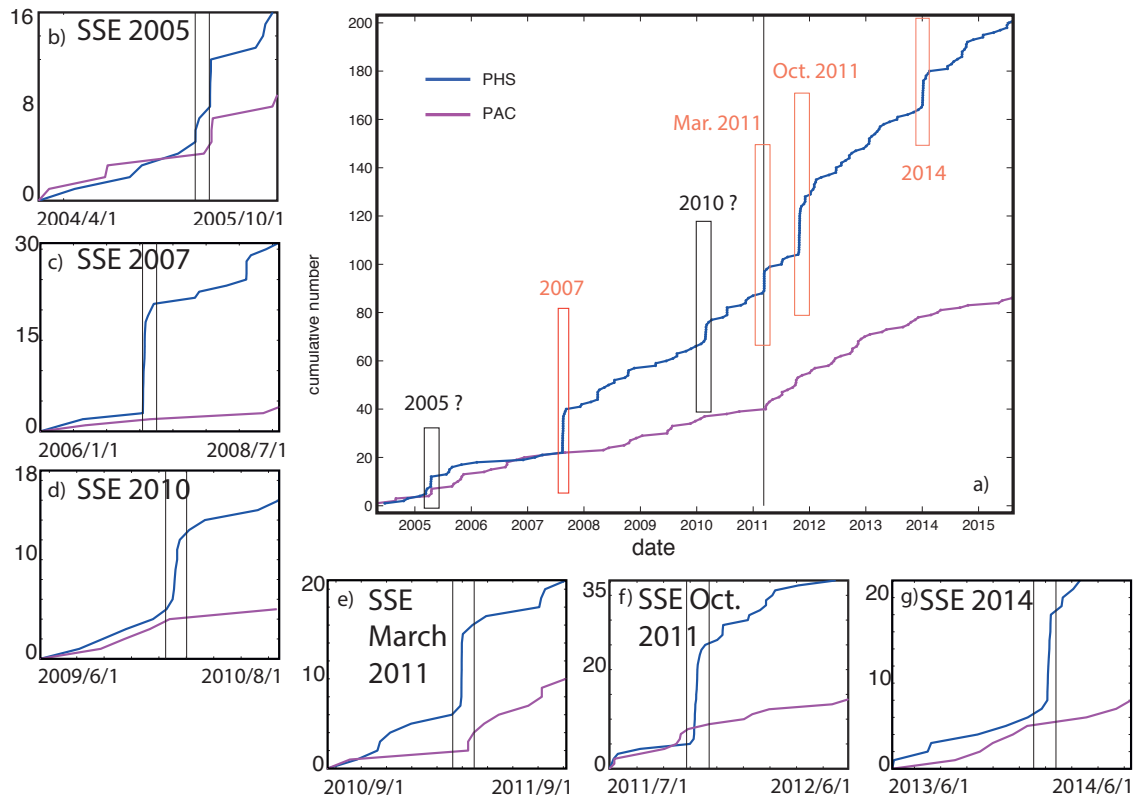
FIGURE 4.7 – Cumulative REs on PHS (blue) and on PAC (pink). Zooms of normalized cumulative number of REs for every SSEs are also displayed (b-g). The beginning and ending dates are given. The time lag between the two vertical black lines corresponds to one month. This shows that the 2005 SSE has a longer duration than the other ones.

A M6.1 earthquake struck on the 2005/4/11 in Choshi, at about 60 km to the north of Boso, on the PAC-NAM interface. This mainschock appears to have generated uplifts several times larger than expected for a normal M6.1 earthquake (Kobayashi and Hirose, 2016). It is therefore uncertain whether the second burst effectively results from slow slip originating from the usual Boso SSE patch. However, other M≥6 earthquakes occured between 2004 and 2015, none of them triggered REs on PHS plate. We furthermore note that a clear change in surface displacement rate concomittent with these 2005 bursts is only observed for station 3033 (figure 4.8) and also that the declustering performed in Reverso et al., (2016) yields an increase in background rate in early 2005 (Figure 2 of Reverso et al., 2016). The REs that occurred from 2005/3/12 to 2005/4/16 are located first at depth and then migrate on both side of the slipping patch (figure 4.10a).
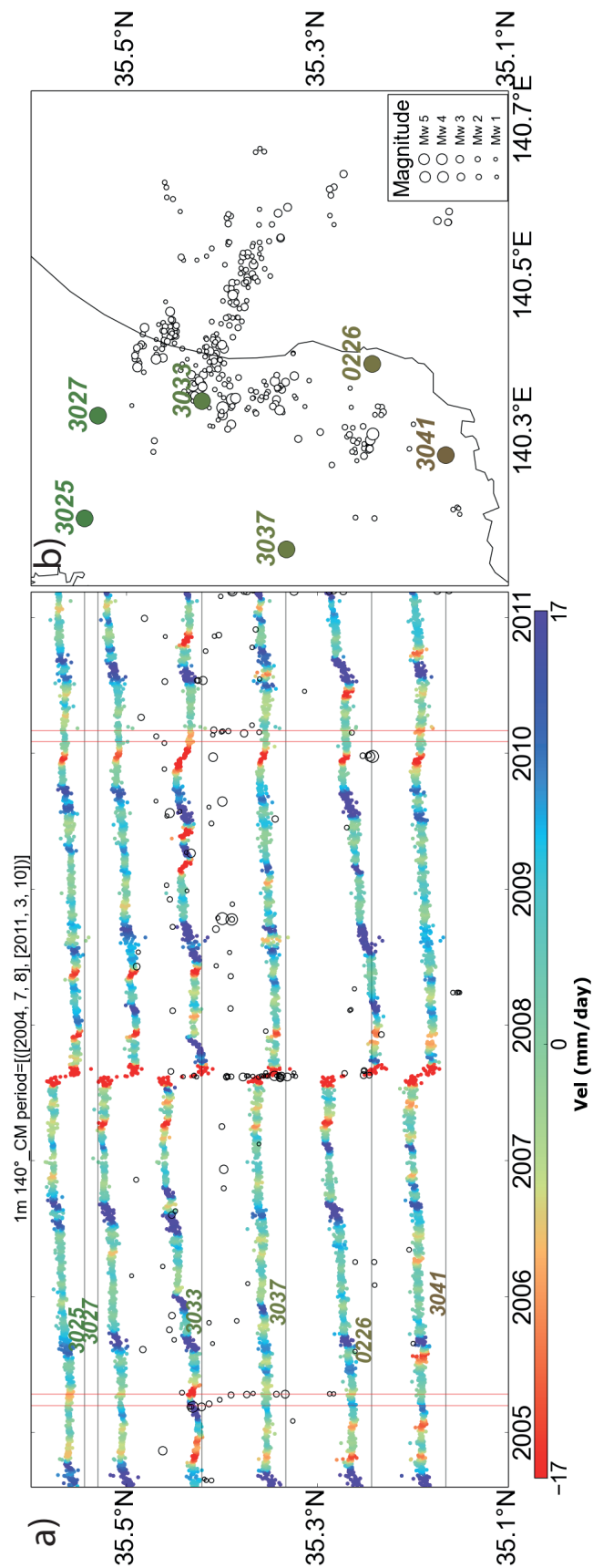
FIGURE 4.8 – a) Velocity variations, averaged over one month (see text for more details) ; The black circles indicate the time of occurence of the REs. b) location of GPS stations and REs.

SSE	cumulative slip (mm)	Mo (N m)	Magnitude	GPS data	reference
2005	8.9	$9.97 * 10^{17}$	5.9	$\sim$5.8	this study
2007	18.4	$2.06 * 10^{18}$	6.1	6.6	Ozawa et al. (2007)
2010	8.6	$9.63 * 10^{17}$	5.9	$\sim$6.1	this study
Mar. 2011	12.9	$1.45 * 10^{18}$	6.0	$<$6.5 ?	Kato et al. (2014)
Oct. 2011	23.7	$2.65 * 10^{18}$	6.2	6.6	Hirose et al. (2012)
2014	10.9	$1.23 * 10^{18}$	6.0	6.5	Ozawa (2014)

TABLE 4.1 – Displacements (in mm), seismic moment and magnitudes estimated for the SSEs using Nadeau and Johnsonś relationship (Nadeau and Johnson, 1998) on REs that occurred during the transient events. These estimated moment magnitude obtained in this study, and only based on REs time series, are compare to estimate from GPS (last two columns).

To estimate the seismic moment of the SSEs, we used the ampirical relationship 4.1 :

$$log(d) = -1.04 + 0.17 log(M_o) \tag{4.1}$$

between the seismic moment (M_o) and the slip (d), already used in Japan (Igarashi et al., 2003; Uchida et al., 2003, 2009). The results are shown in Table 1.

While it is unclear why this law would hold in Boso, as well as the rest of the Japanese subduction zone, we make use of it as a way to estimate the sizes of the 2005 and 2010 SSE relative to the 2007, Oct. 2011 and 2014 SSEs, which moments are directly known from GPS observations.

Although the use of cumulative slip seems to under-estimate M_o compared to previous studies, they yield a first estimation of the maximum value of M_o for the SSEs suggested by our analysis.

The use of Nadeau and Johnson relationship (1998) gives a seismic moment of $9.97 * 10^{17}$ Nm (M_w=5.9) and $9.632 * 10^{17}$ Nm (M_w=5.9) for the 2005 and 2010, respectively.

Another approach to estimate the M_o is the use of the displacement value recorded on GPS data. The directions of displacement at the GPS stations are coherent between the 2007 and the 2010 SSEs (figure 4.12). Thus, we can hypothesize that the slip takes place on the same patch so that the seismic moment is proportionnal to the surface displacement at the stations.

To estimate the magnitude of the 2010 SSE, we thus fit the values of the displacement due to the 2010 SSE vs the displacement due to the 2007 SSE with an affine function :

$d_{2010} = d_{2007} * x$; the least squares estimate gives $x = \overline{d_{2010}d_{2007}}/\overline{d_{2007}^2}$ with $\overline{}$ denoting the mean over the stations (figure 4.9). We first estimate the noise level. To do so, we analyse the GPS signal during 2006, when no SSEs occurred and calculate the covariance of the displacement of the North-South and East-West components. Then, we compute the mean of the eigen values of the covariance to estimate the noise level. We add a gaussian noise to the GPS signal based on the noise level previously computed and estimate the value of x. We find a value of x = 0.26 ± 0.04. This gives a difference in magnitude from -0.44 to -0.5. Thus, according to this computation, the moment magnitude of the 2010 SSE is about 6.1.
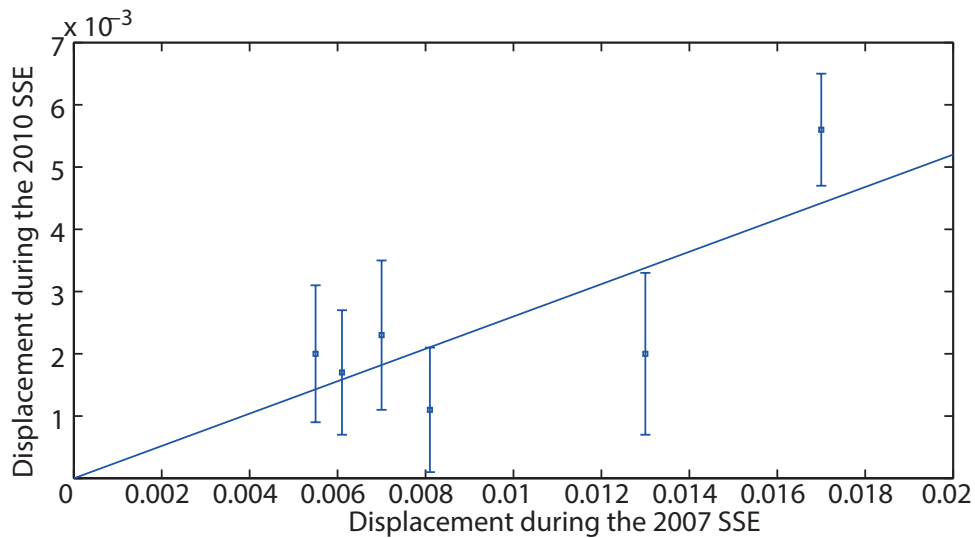
FIGURE 4.9 – Displacement during the 2010 SSE vs displacement during the 2007 SSE. The error bars show the noise level in the data estimated by the analysis of the GPS data in 2006. The line indicates the affine function defined in the text.

We did the same calculation for the 2005 SSE but since the signal is smaller, the relative uncertainty is 50% : x = 0.076 ± 0.04. This gives a moment magnitude of about 5.8.

The 2005 and 2010 SSEs both present smaller magnitudes than the already known SSEs, which explains why they are not as easily observed in geodetic data as the bigger SSEs. Furthermore, they present uncharacteristic behaviors in the timing of activation of the REs compared to the SSEs occurrence time.

REs dynamic confirms previous observations on known SSEs. In 2007, the GPS signal is very strong and sharp. The activated REs occur first on the eastern part of the PHS plate and migrate to the west, along the 56° line (figure 4.10b). It is coherent with the

geodetic inversions calculated by Hirose et al. (2014), where the slip starts in the northeast part of the fault and migrates to the south-west. The maximum slip estimated was 250 mm at lon=140.6 and lat=35.05.

In March 2011, the 11 REs were activated during only three days from the 2011/3/12 to the 2011/3/15. The first REs occured at depth (26 km) and the sequence then migrated towards shallower depths (20 to 5 km) along the eastern part of the fault plane (figure 4.11a). Since this slip event occured only four days after Tohoku-oki earthquake, it is difficult to invert the GPS data. However, the location and migration of the REs indicate that the slip probably had a smaller extension than the 2007 and 2010 SSEs and that it began at depth and migrated towards shallow depth.

In October 2011, the entire area surrounding the fault plane was activated. As for the 2007 SSE, it started on the eastern branch of the fault and migrated to the west while the eastern branch was still activated (figure 4.11b). It is also coherent with the work of Hirose et al. (2014). They estimated a maximum slip of 300 mm located at lon=140.5 and lat=35.05, more to the west than the 2007 SSE.

In 2014, the activation of the REs is delayed compared to the slip which started on the 2013/12/28. The sequence started on the eastern part of the fault and mainly activated REs in this area (figure 4.11c). Two other REs were activated on the western part and the deeper part of the fault and one was activated inside the slipping fault patch. This is in good agreement with the slip distribution assessed by Ozawa (2014). During this SSE, the slip occurred further away from the coast than during the 2007 and October 2011. The total slip amount for this SSE is 10 cm. It had a magnitude of Mw6.5 which is slightly smaller than those of 2007 and October 2011 that had a Mw6.6 (Ozawa et al., 2007; Hirose et al., 2014; Ozawa, 2014). The spatiotemporal evolution of this SSE can be divided in two phases (Fukuda et al., 2014). The first phase (from 2013/12/01 to 2013/12/30) corresponds to a low slow slip event that begins offshore and that slowly migrates to the west. The second phase (from the 2013/12/30 to the 2014/01/09) shows a rapid slip acceleration while the westward migration still continued. The REs that we evidence occured during this second phase.

4.6 Discussion

The combined analysis of GPS data and Repating Earthquakes allows to detect unknwon SSEs. Even though the GPS signal can be weak during these transients, they are
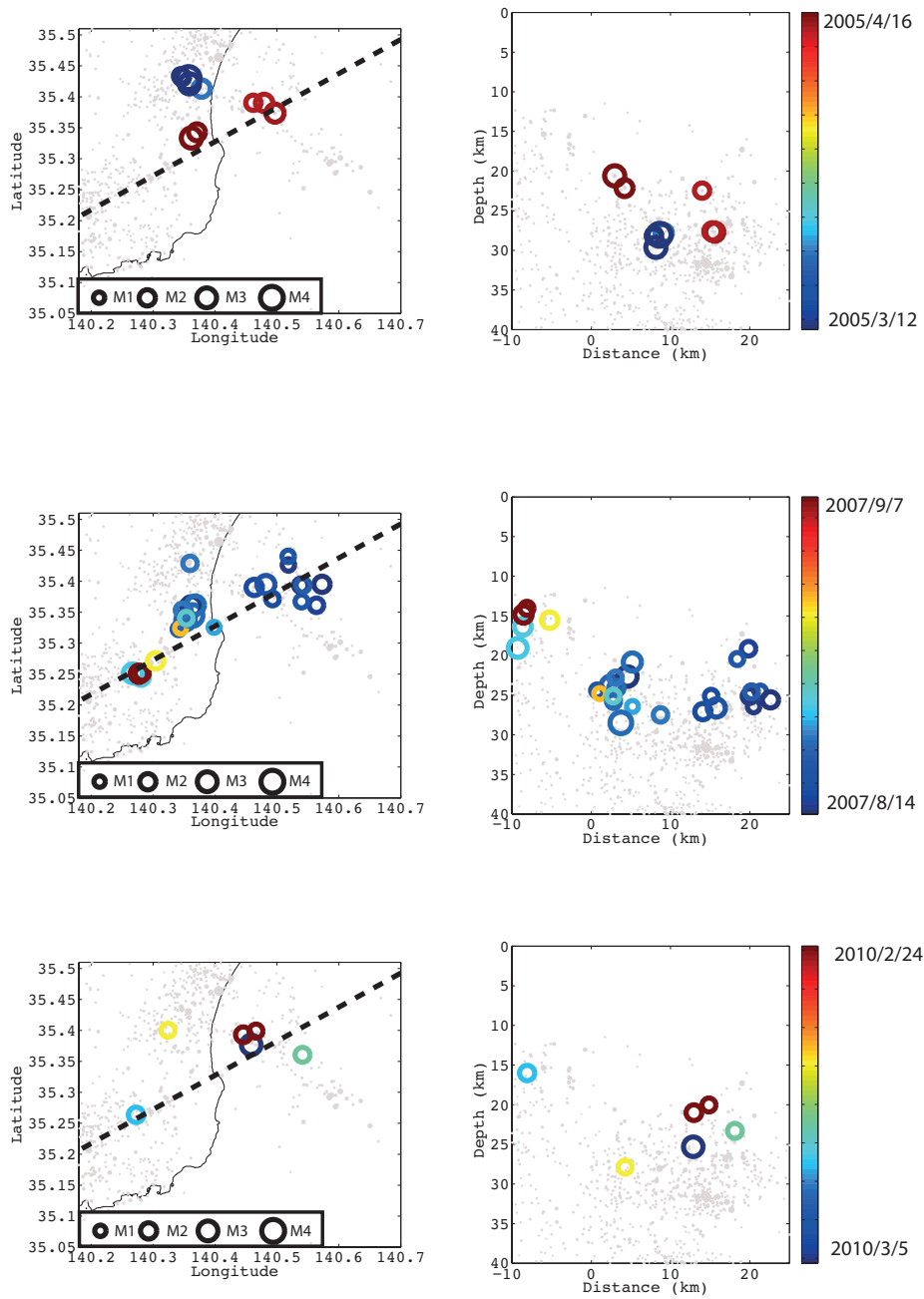
FIGURE 4.10 – Location of the activated REs on a map and on an cross-section of the events projected on the dashed line which has an azimuth of 56°. The color code gives the time of occurrence during the SSEs.
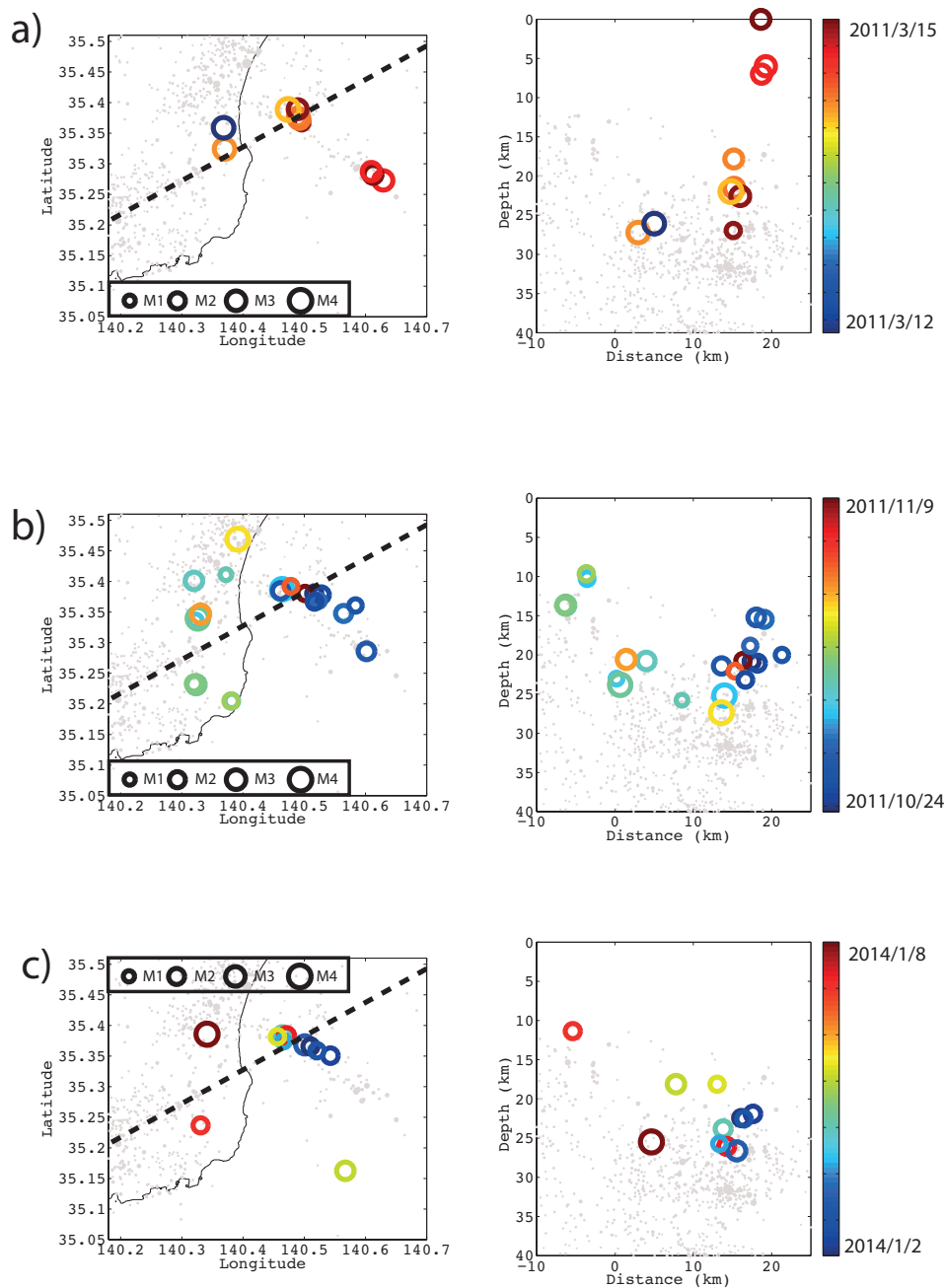
FIGURE 4.11 – Location of the activated REs on a map and on an cross-section of the events projected on the dashed line which has an azimuth of 56°. The color code gives the time of occurrence during the SSEs.
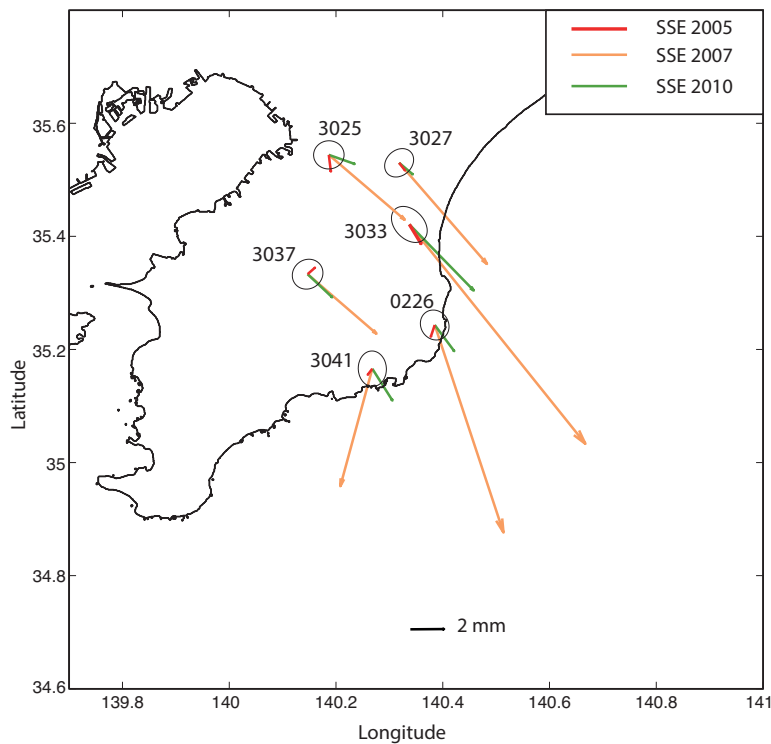
FIGURE 4.12 – Displacements due to the 2005 (red), 2007 (orange) and 2010 (yellow) SSEs in mm. The black ellispoids show the noise level estimated by an analysis on the principal component during the year 2006 when no SSEs occurred.

always accompanied by REs.

The migration of these events indicates different slip processes : east to west (2007, October 2011 and 2014) or west to north (2010, March 2011) or even deep to shallow (2005). The activated REs are different from one SSE to another (figure 4.13).

The REs in 2005 were localized at the downdip tip of the SSE slipping patch. In 2007, they were more REs activated that covered a larger lateral extension and that were also all located downdip, at the edge of the SSE fault plane. This SSE broke three asperities in common with the 2005 SSE. It also has one asperity in common with the 2010 SSE during which there was less activity than in 2007. However, the epicenters distribution covers the same lateral extension. In March 2011, the REs activated were mainly located on the eastern part of the SSE fault plane. The only earthquakes located downdip were also activated during the 2007 SSE. The triggered seismicity during the SSEs of October 2011 and of 2014 have the same lateral extension. No REs were found in the south where

the seismicity concentrated during this SSE (Hirose et al., 2014). The two SSEs also present several asperities in common. Indeed, the asperities activated during the 2014 SSE were all activated during previous SSEs except for one earthquake at shallow depth, in the middle of the slipping patch and another one on the eastern branch.

This analysis shows that there is a long-term migration of the asperity triggered during SSEs : mainly located at the downdip and the western part of the SSE slipping patch first, the activated asperities were then located on the eastern part of the slipping patch where there is a high concentration of REs.

The fact that the 2005 SSE presents a smaller magnitude and/or lateral extension and that the 2010 SSE lasts longer in time than the already known SSE strongly suggest that the fault plane of the Boso SSE has a complex slip history. Furthermore, the 2014 SSE has a nucleation phase (Fukuda et al., 2014) which can also be the case for previous SSEs. Therefore, we must distinguish (i) the 'seismic' duration and (ii) a 'slip' duration. Again, like the 2005 SSE, and dislike the shorter (known) SSEs, the RE activity is more complex, occuring in several brief bursts separated by quiet periods. It is somewhat arbitrary to group those bursts in one single SSE. Instead, slip could be having several phases of acceleration/stopping (or deceleration), equivalent to as many (smaller) SSEs.

Recent laboratory studies on slow earthquakes behaviors show that the duration of such events depends on the effective stiffness of the fault (Leeman et al., 2016) and on the shear strength accumulation variation (Selvadurai and Glaser (2016), submitted). Another explanation of the difference in slipping extension is the variation of stress state with time. The frictional parameters and stress state may vary with time on the SSE fault plane explaining why the extensions can be different from one SSE to another. Also, since the portion at greater depth is at higher temperature, it might be more sensitive to pore fluid pressure variation which directly has an effect on the stress state and the ablity to reach a slip-weakening regime.

We propose the following model as an attempt to explain the differences in slip propagation of the observed SSE. We previously considered that the rupture surface was the same in order to compute the magnitude of the SSEs. Here, we propose a location of the area of maximum slip for the three SSEs based on GPS inversion for the 2007 SSE (Ozawa, 2014) and on REs location for tjhe 2005 and 2010 SSEs. Their location allows to define three area characterized by differences in their friction properties. There is a small area with low friction parameter and a low stiffness value (light grey in figure 4.13) that easily promotes slip. This area is small and slips during the SSEs of 2005, 2007, 2010,

October 2011 and 2014. Its slip might not always been accompanied by seismicity if the magnitude of the SSE is small. This zone is close to the GPS station 3033 and can thus explain the small transients recorded at this station in 2008 without the occurrence of REs. This area is embedded in a larger one with higher friction paramaters and stiffness value (grey in figure 4.13). This area slips during all known SSEs and the 2010 SSE but not during the 2005. Thus, it does rupture only if the stress rate is large enough to overcome the friction parameters. The same processus may take place for the darker grey area that characterizes the rupture zones of the 2007, October 2011 and 2014. This slip extends only if the loading on the fault is high enough to overcome the friction parameter.

This model is theroretical and further observations of SSEs in this area and laboratory experiments are needed to better understand the mechanisms that take place in this zone.

Such variations of slow slip extension was recorded in the Cascadia subduction zone at a greater lateral extension since the Episodic Tremor and Slip events (ETS) cover several hundreds of kilometers (Brudzinski and Allen, 2007; Wech and Bartlow, 2014). On the contrary, in Bungo Channel area, the slip distributions of the three long-term slow slip events of 1997, 2003 and 2010 present a different history but covers the same plate interface (Yoshioka et al., 2015)).

A SSE was detected at very shallow depth in the New-Zealand subduction zone (Wallace et al., 2016). This study along with recent analysis of tremor migration south of Kyushu (Yamashita et al., 2015) suggest that the slip assessed in Boso subduction zone during the SSEs might be underestimated, especially in the eastern part of the slipping fault zone.

In this study, we also analyze the evolution of the REs magnitude with time. We calculate the amplitude ratio between pairs of REs that belong to the same group to assess wether or not the magnitude varies with time especially within a group wich present REs during a SSE and REs during inter-SSE time. There is no clear variation of the magnitude with time, during a SSE.

4.7   Conclusion

The coupled analysis of the REs activity and GPS signals in Boso area allowed to uncover two unknown SSEs that occurred in 2005 and 2010. They show different slip extensions and different magnitudes than the already known SSEs. This leads to a totally
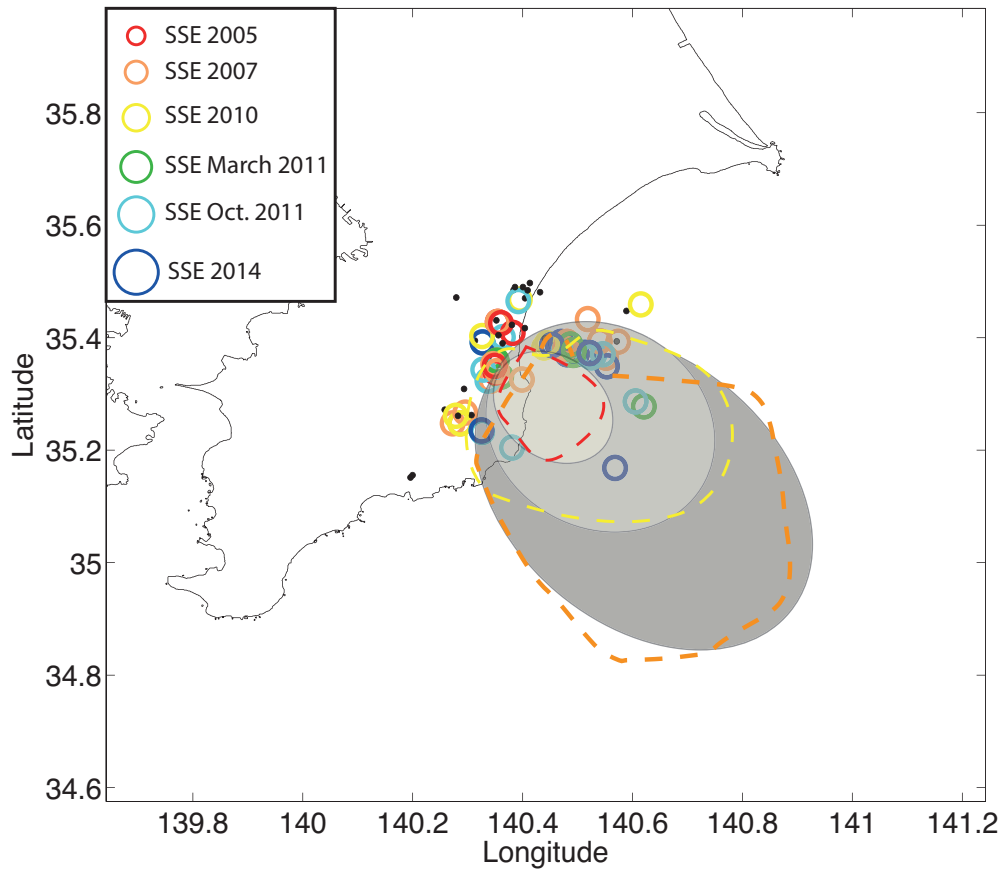
FIGURE 4.13 – Location of the barycenters of the RE groups activated (or not) during the SSEs in color (in black). Location of maximum slip is shown for three SSEs : 2005 (red) and 2010 (yellow) maximum slip zone is deduced from the location of REs ; 2007 (orange) maximum slip zone was inverted from GPS data (Ozawa, 2014).

new history of the slip in the area (figure 4.14). Inbetween 2003 and Tohoku earthquake, the SSEs occured every 2.4 years on a regular basis, instead of the 6-7 years previously estimated. There is no clear evidence of unknown SSE between the March 2011 and the 2014 SSEs which is probably due to the fact that the time interval between SSEs has been decreasing, due to the Tohoku earthquake (Hirose et al., 2012; Kato and Nakagawa, 2014). Without taking the March 2011 into account, we see that the regularity of the time of occurrence is rather well preserved. This might indicate the occurence of a SSE

in the end of 2016- beginning of 2017. In order to properly assess the Boso slip history since the 1990s, the same analysis on REs and GPS data can be done over the period 1990-2004.
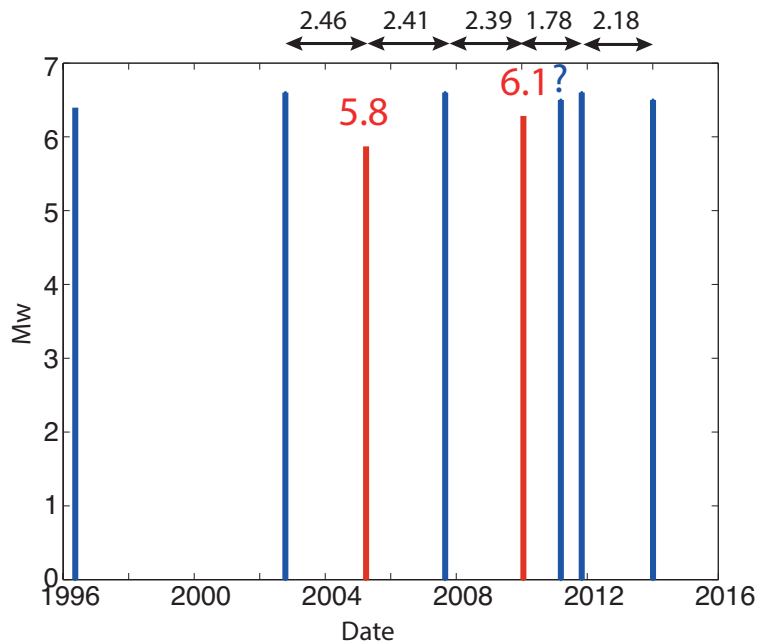
FIGURE 4.14 – Updated history of the Boso SSEs showing the two hidden SSEs that occured in 2005 and 2010. We estimated their magnitude using GPS data. Magnitude of already known SSEs were determined by (Sagiya, 2004; Ozawa et al., 2003, 2007; Hirose et al., 2014; Ozawa, 2014). The magnitude of March 2011 SSE was estimated smaller than 6.5 (Kato and Nakagawa, 2014). Time in years between two successive SSEs is given on the top.

Chapitre 5

Changes in seismicity and stress loading on subduction faults in the Kanto region, Japan, 2011-2014.

5.1 Foreword

The existence of a postseismic phase following a mainshock has been known for decades and consists in the occurrence of postseismic slip and aftershocks. Aftershocks mainly occur soon after the mainshock and they decay with time, following the Omori's law : $n = C/(K + t)^p$ where n is the frequency of aftershocks at a time t after the mainshock, with K, C, and p as fault-dependent constants (p is typically about 1). Most aftershocks occur on or near the mainshock's fault plane. However, only few observations were made on the seismic consequences of a mainshock at its rupture border, outside the aftershocks area. This is what we investigate in this Chapter, analyzing the seismicity in Kanto area during the postseismic phase and the beginning of the interseismic phase (figure 5.1). During the postseismic phase, the strain is at its lower level (figure 5.1 top) and will slowly increase to retrieve the interseismic rate). The postseismic phase is characterized by the presence of many aftershocks in the area surrounding the mainshock rupture (figure 5.1, middle). The GPS data records a postseismic slip that occurs in and around the coseismic rupture zone (figure 5.1, bottom). This postseismic slip can last several years to decade of years.

REs have been identified and studied to define the plate configuration of this area (Kimura et al., 2006). As mentionned in Chapter 2, this area lies close to the triple
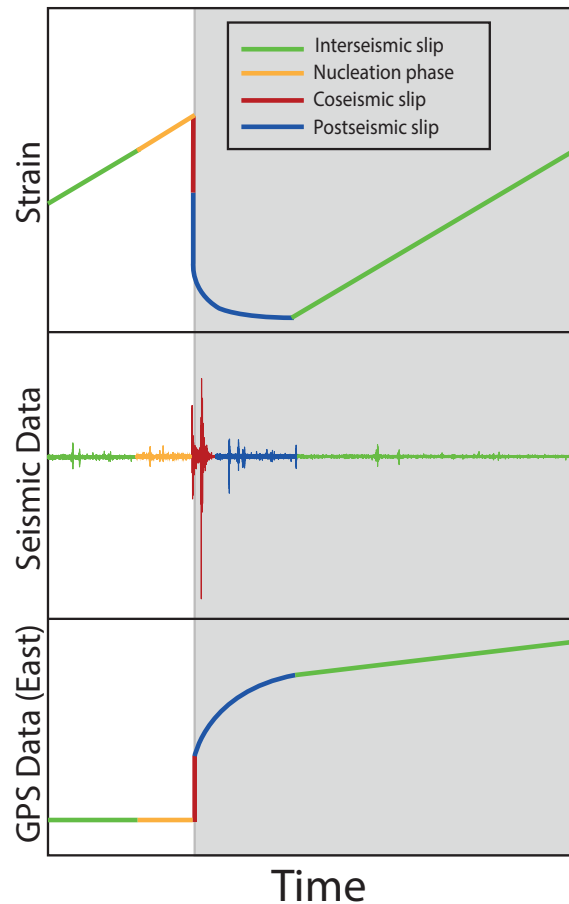
FIGURE 5.1 – The seismic cycle. Top : evolution of strain with time during the seismic cycle. Middle : example of a seismic waveform that represents a sequence with a mainshock (in red) and its foreshocks and aftershocks occurring respectively before (nucleation phase in orange) and after (postseismic phase, in blue). Bottom : displacement at surface recorded with GPS, along the East component. In this chapter, we focus on the postseismic phase in an area at the limit of the mainshock rupture zone.

junction. Furthermore, coupling on the PHS-PAC contact area is weak (Uchida and Matsuzawa, 2011). Coupling is also smaller on the PAC interface in this area compared to the northern part of the plate where the M9.0 Tohoku earthquake struck. The difference in coupling is thought to be one of the reasons why the southern limit of the rupture lies just above Kanto. The area underwent several major earthquakes in the past (Grunewald and Stein, 2006; Nyst et al., 2006). The last one was the Kanto earthquake (M7.9) that struck in 1923 causing the deaths of over 140,000 people (figure 4.2). The mainshock consisted of right-lateral slip with a thrust component on a low-angle fault plane in the

Sagami trough (Nyst et al., 2006). More recently, one of the main aftershocks of the Tohoku earthquake occurred off-coast of Kanto with a magnitude 7.9. Furthermore, an increase in seismic activity in the Kanto region was observed just after the mainshock (Toda and Stein, 2013).

In this chapter, we observe the consequences of the megathrust earthquake on the seismic and aseismic activity in this area and how it affects the rupture zone of the 1923 Kanto earthquake. We also study the behavior of the PAC and PHS plates that are in contact further north. This work was published in the Journal of Geophysical Research : Solid Earth (Gardonio et al., 2015). We extend the analysis to 2015 and focus on the magnitude increase following the Tohoku earthquake and on the lack of periodicity of the REs in Kanto.

5.2 Abstract

Seismic activity has increased in the Kanto region, Japan, following the 2011 M9.0 Tohoku earthquake. We here reassess this increase up to June 2014, to show that normal, Omori-like relaxation characterizes the activity on crustal faults as well as on the Philippine Sea plate, but not on the deeper Pacific plate. There, repeating earthquakes display a two-fold rate of occurrence (still on going in June 2014) as compared to the pre-Tohoku rate, suggesting enhanced creep. We compute the Coulomb stress changes on the upper locked portion of the Philippine Sea plate, which last ruptured in 1923. We find that this fault was little affected by either the co-seismic, the post-seismic, the accelerated creep, or the 2011 Boso silent slip event.

5.3 Introduction

The Kanto region that hosts Tokyo and its 25 million inhabitants is characterized by a double subduction : the Philippine Sea plate (PHS) subducts northward at shallow depth underneath the North American plate (NA) and the Pacific plate (PAC) dives beneath both PHS and NA at greater depth (Ishida, 1992; Wu et al., 2007), cf. Figure 4.3a. The updip portion (depth z less than 20 km) of the PHS plate is known to be locked (Sagiya, 2004; Nishimura et al., 2007) and to accummulate stress ; its failure can cause destructive earthquakes, like the M7.9 Kanto earthquake that stroke the region in 1923. Kanto lies just off the 2011, M9.0 Tohoku rupture, although one of the biggest aftershocks, of magnitude $m = 7.9$, occurred off-coast Kanto, extending the mega-thrust rupture zone more to the south. The question as to whether the 2011 mega-thrust rupture and its aftershocks have hastened or not the future occurrence of a large earthquake in the Kanto region is of paramount importance, given the dense population and potential economic loss that would result from such a catastrophic event. Toda and Stein (2013) observed an increase in seismicity after the 2011 shock, developing into a constant rate of earthquakes 2.9 times higher than the prior rate. This rate increase appears consistent with both positive changes in Coulomb stress resolved on deep portions of their proposed Kanto fragment, in particular, as well as with a clear tendency for Coulomb stress changes to be positive when computed using the focal mechanisms of earthquakes that occurred prior to the mainshock (Ishibe et al., 2011). Uchida and Matsuzawa (2013) likewise document a ×9 increase compared to pre-Tohoku rate, in the rate of repeating earthquakes (their area 16) from April to December 2011, which marks the end of their analysis period.

Also, Hirose et al. (2012) argued that the Tohoku earthquake hastened the occurrence of the recurrent slow slip event (SSE) off Boso, on the PHS plate. All these observations (see also Somerville, 2014) suggest that a significant increase in stress loading was brought up in the Kanto region by the 2011 mainshock.

We here dwell on the study by Toda and Stein (2013) in order (i) to investigate how the change in seismicity has evolved with 18 extra months of data, and (ii) to monitor time variations in creeping rate at depth on the PHS plate as evidenced by repeating earthquake time series and how this change in creep more particularly affected the locked, updip portion of the PHS plate.
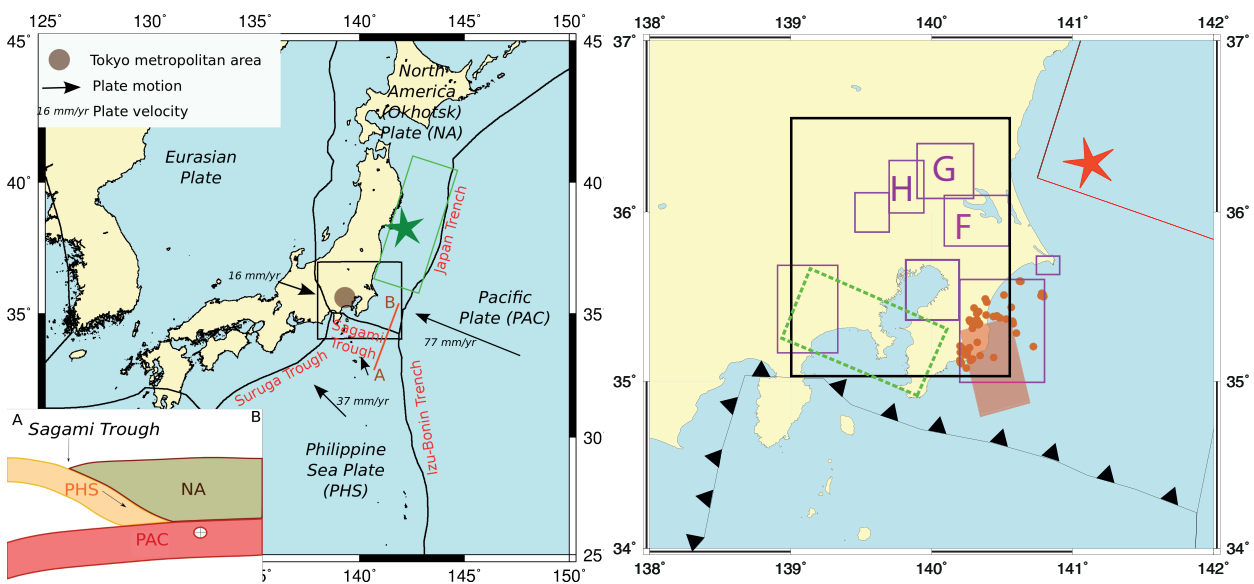
FIGURE 5.2 – Tectonic settings of Japan. (a) The black rectangle shows the Kanto area. Box : Simplified view of the plates interaction with depth along the brown line AB (no scale). (b) Brown rectangle showing the source of the October 2011 slow slip event (SSE) in the Boso area (Hirose et al., 2012), the brown dots representing the swarm earthquakes that accompanied it. The source of the 1923 Kanto earthquake (Matsu'ura and Iwasaki, 1983) is shown in green. The black rectangle delimits the area studied here. The red line shows the southern limit of the 2011 Tohoku rupture based on the locations of its immediate aftershocks ; the red star is the epicenter of the M7.9 aftershock that occurred half an hour after the mainshock. The purple boxes show the areas where repeating earthquakes have been observed for the 1979 - 2003 period (Kimura et al., 2006; Uchida et al., 2009). We here study repeating earthquakes in areas F, G and H of Kimura et al. (2006) only, for the 2004 - 2014 period.

5.4 Changes in seismicity caused by the Mw 9.0 To-hoku earthquake

Toda and Stein (2013) observed changes in seismicity due to the Tohoku earthquake between 2009-2012 in the area delimited by the black rectangle of Figure 5.2b. They found that seismicity remained constant from the end of 2011 throughout the whole of 2012, suggesting that the loading of active portions of the mega-thrust faults in Kanto has reached a new, accelerated, steady rate. They were able to fit the time series with a rate-and-state model driven by Coulomb stress changes brought by both the M9.0 and its M7.9 aftershock, resolved on individual fault planes. To do so, they needed to raise the stress loading rate from 0.25 to 0.7 bar/year, hence a 2.8 times increase. According to this study, this translates into a 2.5 increase of the estimated probability that a $m \geq 7.0$ earthquake will strike the region in the 5 years after the M9.0 mainshock.

We analyze the Japan Meteorological Agency earthquake catalog spanning from January 2009 to June 2014, in the same area (black rectangle of Figure 5.2b), to show that, while the relaxation actually resumed after 2012, hence after the time period analyzed by Toda and Stein (2013), this relaxation is anormally slow in the 30 to 85 km depth interval which characterizes subduction seismicity.

Changes in earthquake rate over time are computed ; in order to make sure that these changes do not come from a bias due to a change in magnitude of completeness m_c, we estimate the latter before and after the Tohoku earthquake, in the Kanto area (Figure 5.3). We find that $m_c = 1.5$ for the 1/1/2009 - 11/3/2011 period, and $m_c = 2.0$ after 11/3/2011. The latter m_c applies shortly after the mainshock : $m \geq 2.0$ earthquakes are complete after 10 days past the mainshock, and this period of completness at $m_c = 2.0$ possibly extends even earlier in time, although the limited number of earthquakes then prevent us from being definite.

The seismicity rate in the area of Kanto is constant during the pre-Tohoku period (2009 to 11/3/2011), and then increases after the Tohoku earthquake until reaching a plateau after 90 days (Figure 5.4). This plateau lasts for about 300 days. This regime is coherent with the analysis of Toda and Stein (2013) and affects the whole of Kanto. However, we find that it did not last past this interval of 300 days ; relaxation then resumed as normally expected. This observation is further confirmed when removing aftershocks from the data and calculating the background seismicity using the method of Marsan et al. (2013), see Figure 5.5.

All depth intervals do not show the same behavior (Figure 5.6). Crustal depths (0-30 km) undergo an increase of seismicity after the Tohoku earthquake that is well fitted by an Omori-Utsu law $\lambda(t) = K/(t + c)^p + \mu$, where λ is the earthquake rate, and μ the pre-Tohoku rate; we find an exponent $p = 1.17$ by maximizing the likelihood for inhomogeneous Poisson statistics (red curve in Figure 5.6a), up to a second rate increase in October 2011 corresponding to the occurrence of a SSE in Boso (Hirose et al., 2012, 2014). The seismicity rate then resumes the pre-Tohoku value about one year after the mainshock. An omori-Utsu decay is only asymptotic; we thus here use the 125% level, i.e., the rate equals 125% of the pre-seismic rate, to arbitrarely fix a characteristic time. We find that the fitted Omori-Utsu law is back to this 125% level after 408 days. Visually, the slope of Figure 5.6a after mid-2012 is indistinguishable from the pre-Tohoku rate. The seismicity then increases again due to a one week-long swarm in the Boso area at the beginning of 2014.

Between 30 and 85 km depth, a low p value of 0.66 is needed to fit the Omori-Utsu law (Figure 5.6b). This points to an anomalously slow relaxation of the stress imparted by the mainshock and its M7.9 aftershock. An anomalously low $p = 0.44 \pm 0.07$ was similarly needed by Toda and Stein (2013) to model the seismicity in Kanto up to 2012 without changing the background rate. However, this slow relaxation is here found to be valid up to June 2014, without any apparent departure from this trend, and to only characterize subduction depths. The relaxation at these depths was still going on by June 2014; if it were to continue unchanged, the seismicity rate would reach 125% of the post-Tohoku rate after 19 years (i.e., in 2030).

To check how peculiar this slow relaxation is, we looked at the cumulative number of earthquakes in the northern part of Honshu for rectangular areas of $1^o \times 1^o$ at subduction depths under the land. The only areas that show an increase in seismicity are the ones closest to the Tohoku earthquake epicenter. The rest of subduction seismicity underneath Honshu resumed the pre-Tohoku rate within less than 2 years, unlike Kanto where one can speculate about on-going creep in the transition zone that potentially affects the loading of the updip PHS interface.

At greater depth ($z > 85$ km), the effect of the Tohoku earthquake is not as strong as for $30 < z < 85$ km (Figure 5.6c), at least for $m \geq 2.0$ earthquakes. We find a +18% increase in rate between the pre and post-Tohoku periods, with both periods characterized by a nearly constant rate. The probability that the observed 357 $m \geq 2.0$ earthquakes after the mainshock could be due to natural fluctuations in an homogeneous Poisson process with rate equal to the pre-Tohoku rate is 2.7×10^{-5}, implying that this

rate change, although very moderate, is statistically significant.

Increased seismic activity in Kanto can be potentially linked to the local maximum in post-seismic slip found from GPS inversion offshore Kanto (Ozawa et al., 2011, 2012; Perfettini and Avouac, 2014). This maximum is well evidenced by a change in direction of the surface displacement vectors between the co and the postseismic phases. Using 512 GPS stations in central and northern Japan, we fit the measured post-seismic displacements as $U(t) = a \times \log(1 + t/\tau) + b \times t$, where U is the displacement component (east, north or up) and t is the time (in days) after the Tohoku earthquake, up to 22/9/2012. A least-square fit is performed from the first sample after Tohoku, accounting for the uncertainties in the displacement increments. We use the best fits to extrapolate the post-seismic displacements up to 1 year after the mainshock, and plot them together with the co-seismic displacements (Figure 5.7). The local slip maximum at depth is evidenced by GPS stations for which postseismic displacement is relatively strong and presents a clockwise rotation from the coseismic displacement direction.

We conclude from this analysis of seismicity that, while crustal activity was only affected for about one year after the mainshock, deep portions of the PAC and PHS subducting slabs exhibit changes that have not, so far, fully relaxed. In fact, the observed relaxation of activity in the 30 - 85 km depth range is anomalously slow (p exponent of 0.66, well below the typical 1.0 value). GPS displacements clearly suggest that off-rupture post-seismic slip developed in Kanto after the Tohoku earthquake. This slip was potentially still going on in June 2014, as evidenced by seismicity. We now further investigate this particular depth range, by analyzing time series of repeating earthquakes occurring on both subducting plates, to resolve variations in creeping rate.

5.5 Repeating earthquakes

Repeating earthquakes (REs) are earthquakes that break a common asperity with nearly identical rupture lengths. REs have been found in California, most notably on the Parkfield segment of the San Andreas Fault (Nadeau et al., 1995), and in Japan (Matsuzawa et al., 2002), including the Kanto region (Kimura et al., 2006), as well as other parts of the world (e.g., Chen et al. (2007); Bouchon et al. (2011)). In order to repeatedly rupture the same fault patch, the stress-bearing asperity must be mechanically isolated to some extent from other, neighboring asperities. The picture according to which these asperities are surrounded by a velocity-strengthening (i.e., creeping) fault zone has
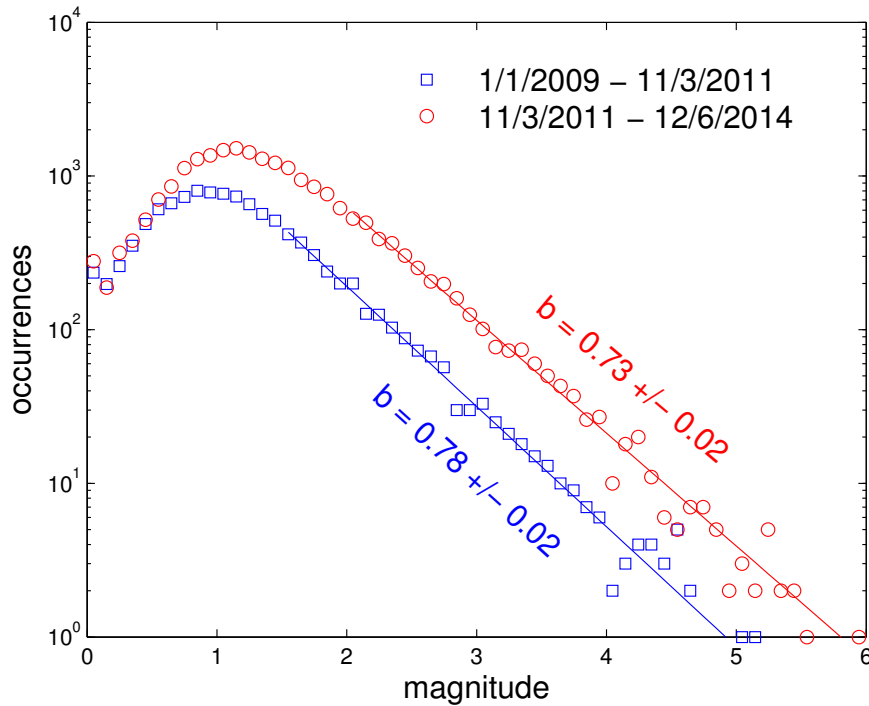
FIGURE 5.3 – Number of earthquakes vs. magnitude in the Kanto region (black box of Figure 4.3b), for the pre and post-Tohoku periods. The magnitude of completness is taken equal to 2.0 for the overall period.

thus emerged. Departure from such a periodic, hence stationnary, regime can reveal either stress interactions between asperities, changes in creeping rate, or complexity in the rupture process (Schaff et al., 1998; Nadeau and McEvilly, 1999; Lengliné and Marsan, 2009; Bouchon et al., 2011).

We here study the occurrence rate of REs in the Kanto region, in order to measure how slow slip at depth has been perturbed by the 2011 M9.0 mainshock, on both subducting plates. Following the work of Kimura et al. (2006), who identified clusters of REs at several locations on the Philippine Sea plate interface, we limit our study to their three areas that contain the most REs for their 1989 - 2003 period (areas F, G and H, see Figure 5.2), but did not consider their area D (see Figure 3 of Kimura et al., (2006)) which hosts the earthquake swarms related to the recurrent Boso slow slip event. REs were found in these three areas at depths greater than 20 km, that are characteristic of the transition zone between the locked portion of the fault updip, and the downdip freely slipping part. At these depths, low seismic coupling is found on the Philippine Sea plate
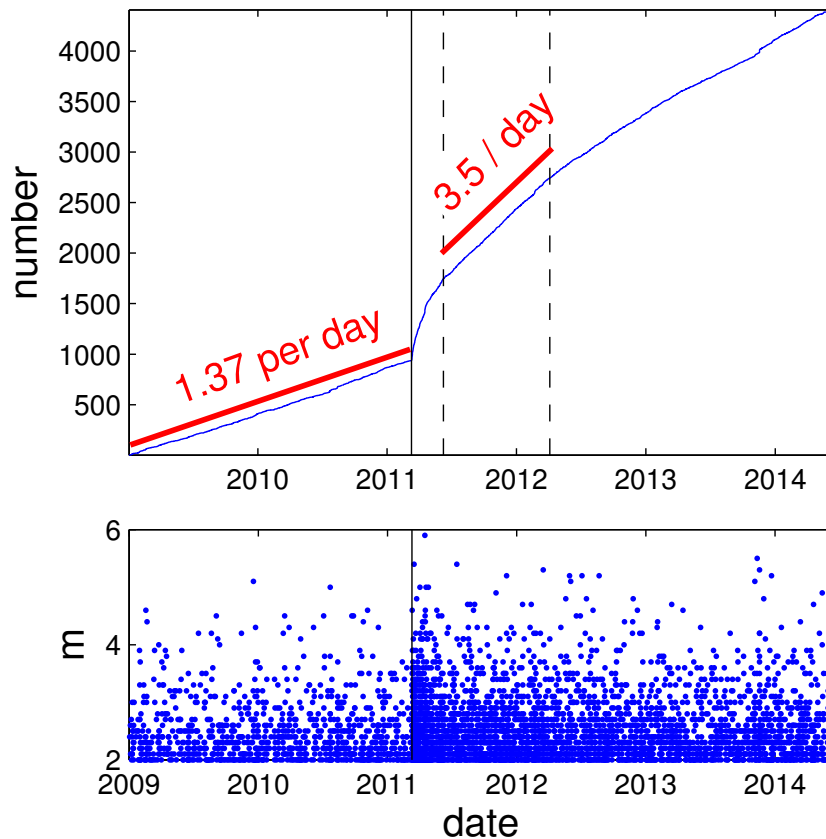
FIGURE 5.4 – Top : Cumulative number of $m \geq 2$ earthquakes in the Kanto area located
at depth between 0 and 100 km. The black line indicates the occurrence of Tohoku.
Bottom : Magnitude vs. time. The period characterized by a constant, increased, rate of
3.5 per day, ended after about 300 days. A slow relaxation then resumed.

(Sagiya, 2004; Nishimura et al., 2007), possibly as a result of the mixture of asperities
and invading creeping patches.

We analyzed the waveforms of all $m \geq 1.0$, $z < 100$ km earthquakes from 2004 to
June 2014, that are located in these three areas, as listed in the JMA dataset, following a
method derived from Got et al. (1994) and Lengliné and Marsan (2009). Two minute-long
records sampled at 100 Hz of the vertical component at the closest 10 Hi-net stations were
processed. For each pair of earthquakes and each recording station, the mean coherency
in the 1.5 Hz - 8 Hz band was computed, for a 512 sample-long window initially centered
on the P-wave arrival. Time delays were also computed in the same frequency band,
by linearly fitting the coherency phase weighted by the coherency squared modulus. An
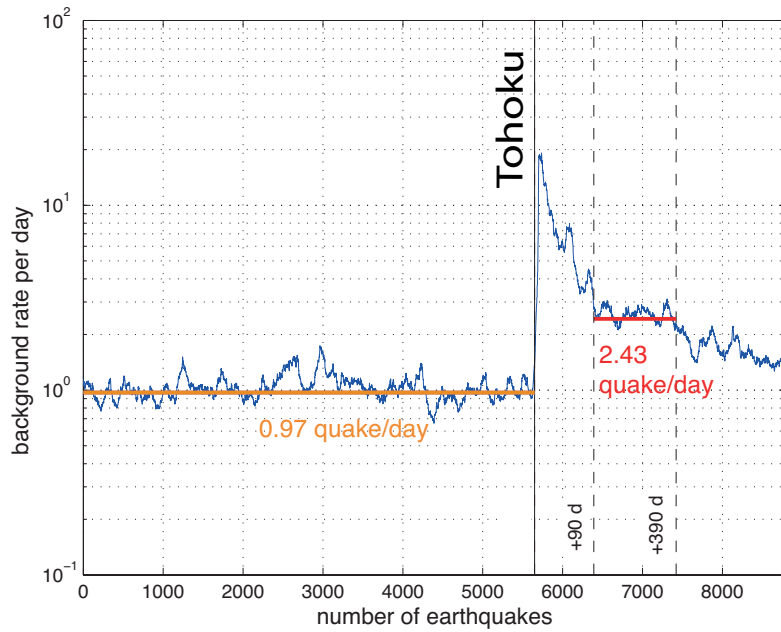
FIGURE 5.5 – Background seismicity rate for $m \geq 2$ earthquakes computed with the method described in Marsan et al. (2013), again showing a transient regime with a constant background rate from +90 to +390 days after Tohoku, followed by further relaxation.
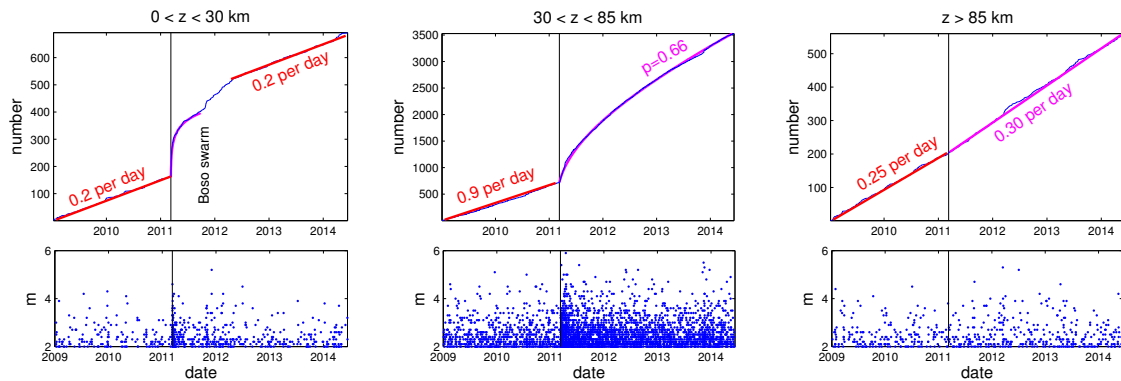
FIGURE 5.6 – Top : Cumulative number of earthquakes for the Kanto area at crustal (0-30 km), intermediate (30-85 km) and greater depths ($z > 85$ km). Fits by a constant occurrence rate in the pre-Tohoku phase, and by an Omori-Utsu law after the Tohoku earthquake, are shown in color. Bottom : Magnitude vs. time.

iterative procedure that aligns the two waveforms, and then recomputes the coherency and time delays on the new 512 sample-long windows, allows to optimize the mean coherency and the accuracy of the estimated delay. We then selected all earthquake pairs
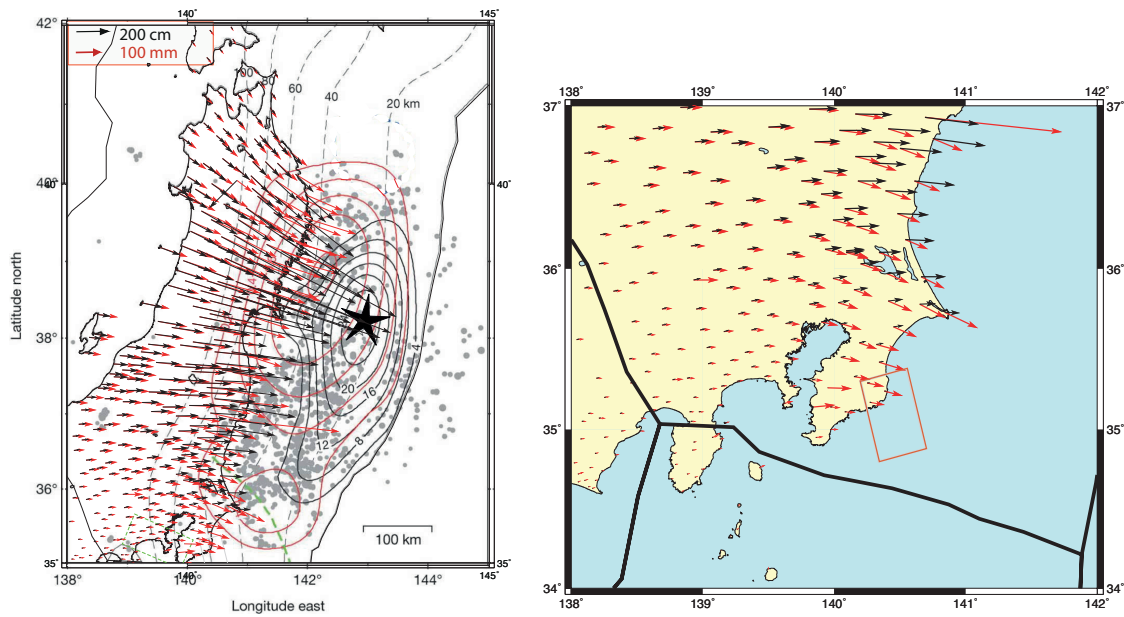
FIGURE 5.7 – Coseismic (black arrows) and postseismic (red arrows) horizontal inland
displacements along with estimated coseismic (black contour with 4 m interval) and
postseismic slip (red contour with 0.2 m interval) on the PAC plate, after Ozawa et al.
(2011) who studied postseismic slip from the 12th to the 25th of March 2011. The black
star is the Tohoku earthquake epicenter, and gray dots are aftershocks. The source of
the October 2011 Boso SSE is shown in red (Hirose et al., 2012). (b) Zoom in on the
Kanto area (black rectangle in (a)). The reference point is the northernmost station in
Hokkaido.

characterized by a mean coherency greater than 0.9 at at least 4 stations, which is the
minimum number in order to resolve the relative locations, by least-square fitting the time
delays. We are here only interested in the distance d between each two earthquakes, for
the pairs that passed the selection criterion. Rupture overlap is calculated by comparing
d with the rupture radii L_1 and L_2 of the two earthquakes, with $L = (7M_o/16\Delta\sigma)^{1/3}$
(Eshelby, 1957), for a $\Delta\sigma = 30$ bar stress drop. For two earthquakes to be repeating
instances of a nearly identical rupture, we require $d < \max\{L_1, L_2\}$, and their magnitudes
to differ by 0.5 or less. We finally group together all pairs of REs that share a common
earthquake, and iterate until no earthquake belongs to distinct groups.

Figure 5.8 shows an example of two earthquakes (2006/4/9 $m = 3.1$ and 2011/4/4
$m = 3.4$) with aligned waveforms at the 7 stations with mean coherency greater than 0.9.
These two earthquakes are found to be distant by 96.5 ± 3.1 m, and thus to have a strong
rupture overlap since $L_1 = 186$ m and $L_2 = 263$ m. An identical method, but based on
the cross-correlation of 1.5 - 8 Hz band-pass filtered waveforms rather than coherency,

gives $d = 132 \pm 18$ m, which still corresponds to a strong overlap. These two earthquakes are part of a RE sequence that counts 8 occurrences, see Figure 5.8. This sequence is clearly not periodic, nor are the large majority of the other sequences. Perturbation by the 2011 M9.0 mainshock can explain this non-periodicity, but asperity interactions are likely to play a role too, as for example evidenced by the first two ruptures in this particular sequence, that occur in the pre-Tohoku period and are separated by only 116 days.

We find 105 RE sequences, grouping 355 earthquakes, with the largest sequence counting as many as 17 earthquakes. The sequences are approximately equally distributed on the two plates, see Figure 5.9. In order to capture a common trend in creeping rate, we tack the occurrence time series of all RE sequences separately for the two plates, cf. Figure 5.10 . We checked that the cumulative slip (instead of cumulative number) time series follow very similar trends to these. Many stations among the 10 in our set were not operationnal before April 2006, which thus marks the beginning of the stable inter-seismic period we were able to resolve.

Following a sudden increase and subsequent relaxation after the M9.0 mainshock, the REs located in the Pacific plate were still occurring in June 2014 at a rate 2.1 higher than the inter-seismic rate. This high rate has remained stationnary for one year prior to this date. The ratio of 2.1 is robust when testing other RE selection criteria (i.e., by changing the minimum degree of rupture overlap, and the magnitude difference).

In contrast, the RE occurrence rate in the Philippine Sea plate exhibits a clear relaxation following the initial increase after 2011/3/11. We fit this rate with an Omori-Utsu law with $\mu = 15.8$ per year for the inter-seismic RE rate. Two fits are computed, (1) the first by taking into account all RE occurrences between 2011/3/11 and June 2014, and (2) by fitting only the REs occurring between 2011/3/11 and 2012/7/1, which marks the beginning of a significant increase in rate, see Figure 5.10. According to these models, the rate increase ranges between +18% and +28% after 3 years, and should decay quickly to a value ranging between +2.6% and +5.7% after 10 years (i.e., in 2021). These estimates indicate that the increase is much less than the current +110% increase experienced by the Pacific plate.

A 80 day-long increase is also observed from July to September 2012 for the Philippine Sea plate, that we could not relate to any evident cause like a strong, local shock, triggering extra seismic activity. During this time interval, only 2 REs occurred in the Pacific plate, which is an anomalously low number. This suggests that an increase in

slip might have taken place on the Philippine Sea plate, with a slip rate 6 times higher than the inter-seismic rate according to our RE time series (hence a total slip of 32 mm, taking the inter-seismic rate of 25 mm/year estimated for segment O in Nishimura et al. (2007)), and that it reduced the stressing rate on the deeper Pacific interface. Coulomb stress was computed with the source (with 32 mm slip) and receiver faults described in the following section. We find a Coulomb stress change of +0.012 bars. This very low stress change implies that direct mechanical interactions between the two plates are insignificant, at least with the small area of the PHS plate imaged by the locations of our REs. Finally, visual inspection of the GPS displacements at stations just above this area do not reveal any obvious sign of accelerated convergence during this period. Our source dislocation would generate a 0.7 mm (horizontal) and 3 mm (vertical) maximum surface displacement, which is about the measurement error of 1 day solution for GPS displacements.
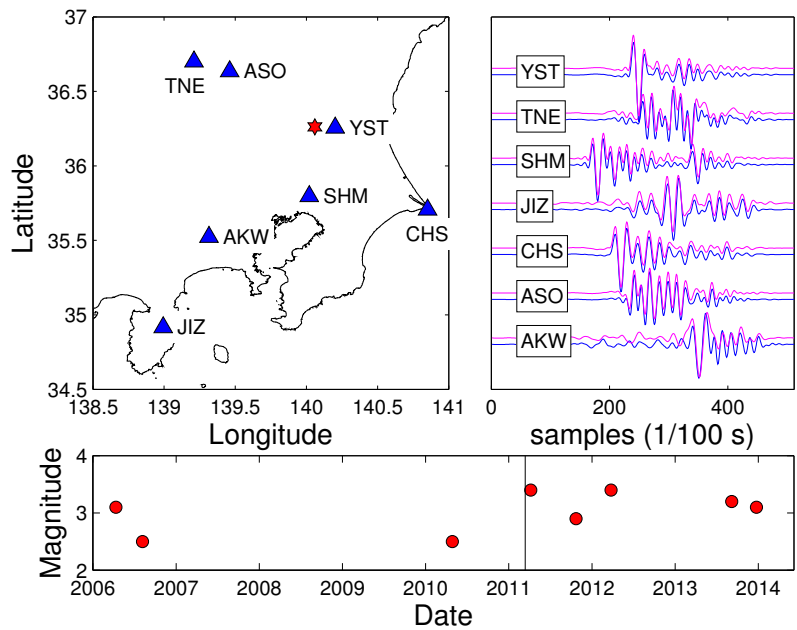
FIGURE 5.8 – An example of two repeating earthquakes (2006/4/9 $m = 3.1$ and 2011/4/4 $m = 3.4$) with coherencies greater than 0.9 at 7 stations. The windowed, 1.5 - 8 Hz band-pass filtered aligned normalized waveforms are shown for all 7 stations. The time axis is arbitrarely offset from one station to the next, for better readability. Bottom graph : occurrence times and magnitudes of the 7 earthquakes forming the sequence which contains the 2006/4/9 and 2011/4/4 earthquakes. The vertical line marks the date of the M9.0 mainshock.
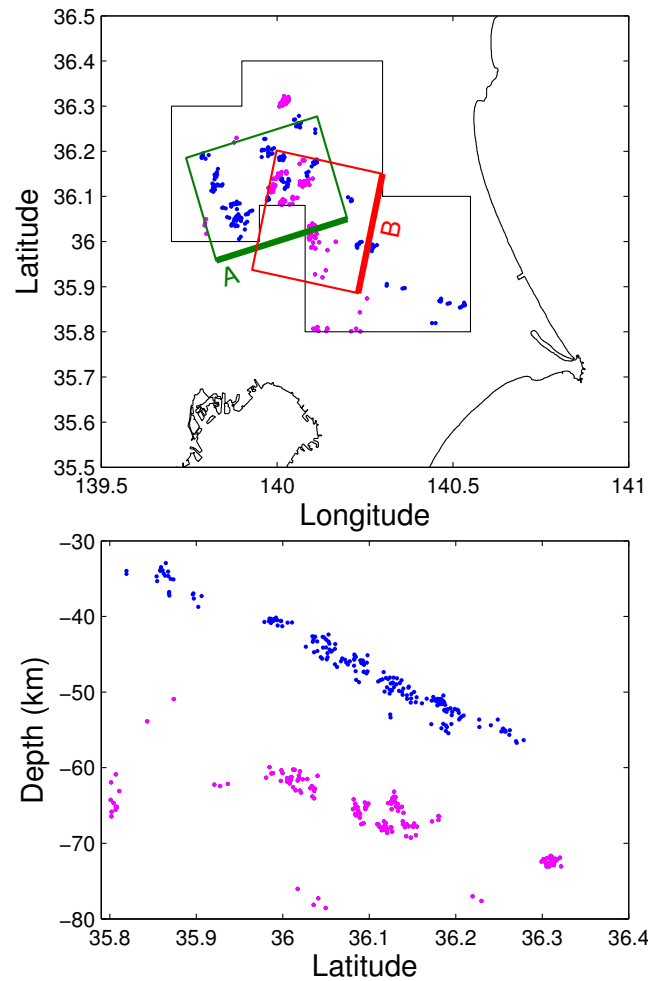
FIGURE 5.9 – Map and cross-section of the repeating earthquakes, color-coded according to the plate they are located in. Only earthquakes within the dashed box are analyzed (areas F, G and H of Kimura et al. (2006)). The two rectangular fault surfaces defined in the Discussion section are shown in green (fault A on PHS) and red (fault B on PAC); their upper limits are at 42 km and 60 km depth, respectively (thick lines).

5.6   Discussion

REs time series indicate that both plates have undergone accelerated creep in their transition zones at depth in the Kanto region. For the Pacific plate, which hosted the M9.0 rupture further up North, this acceleration is still strong in 2014, and does not show any clear sign of relaxation as yet. We investigate whether this observation is consistent
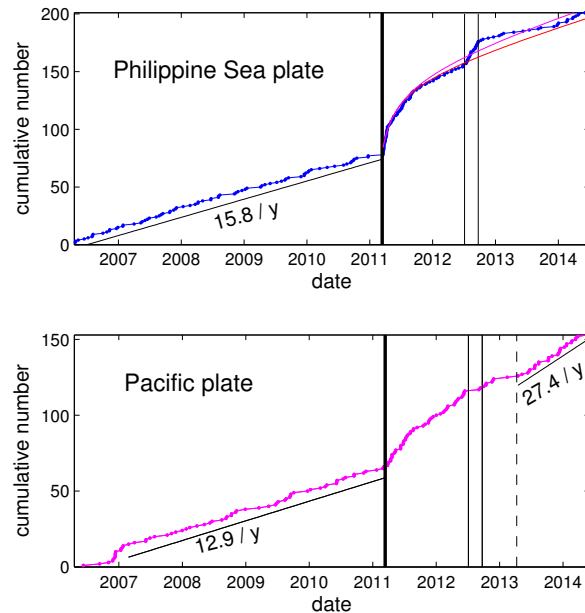
Figure 5.10 – Repeating Earthquake time series, for the two plates taken separately. The occurrence date of the M9.0 Tohoku earthquake is indicated by a thick vertical line. Two Omori-Utsu laws are shown for the Philippine Sea plate when fitting from 2011/3/11 to 2012/7/11 (red) and from 2011/3/11 to June 2014 (purple), see text. The 80 day-long transient in rate (July to September 2012) is delimited for the two plates by the vertical lines.

with static stress triggering. We model the geometry of the two areas in which we find REs : for REs on the PHS interface (fault A of Figure 5.9) we assume a 253° strike and 28.4^o dip (Kimura et al., 2006). The Euler poles of Nishimura et al. (2007) then impose a rake angle of 87° for the 35 km $\times$ 30 km rectangular patch that contains our REs, consistent with the almost pure inverse mechanisms of most REs found in this area by Kimura et al. (2006). For REs on the PAC plate upper surface (fault B of Figure 5.9), we take the strike, dip and rake angles of zone D of Nishimura et al. (2007) , i.e., 192°, 23° and 95° respectively, and define a 30 km $\times$ 30 km fault surface.

We compute the change in Coulomb stress at the center of our two faults, for a friction coefficient of 0.4, that would result from 1 m of pure dip-slip on individual triangular dislocations paving the Pacific plate surface. We used the same dislocations as Perfettini and Avouac (2014), that are based on the modeled plate surface of Hayes et al. (2012). Almost all dislocations contribute positively to an increase in Coulomb stress on fault B (Figure 5.11b), except for two triangles very close to the fault due to errors and mismatch

in geometrical modelling between the paving and our definition of fault B. This positive Coulomb stress changes are expected given the simple and regular geometry of the plate. For fault A located on the Philippine Sea plate, positive contributions are found for a roughly SSW - NNE trending band of the Pacific plate, cf. Figure 5.11a. The accelerated rate of REs on fault A thus implies that the co-seismic slip distributions of the 2011 M9.0 mainshock and of its immediate M7.9 aftershock just offshore Kanto preferentially occupy this band, in the vicinity of fault A.
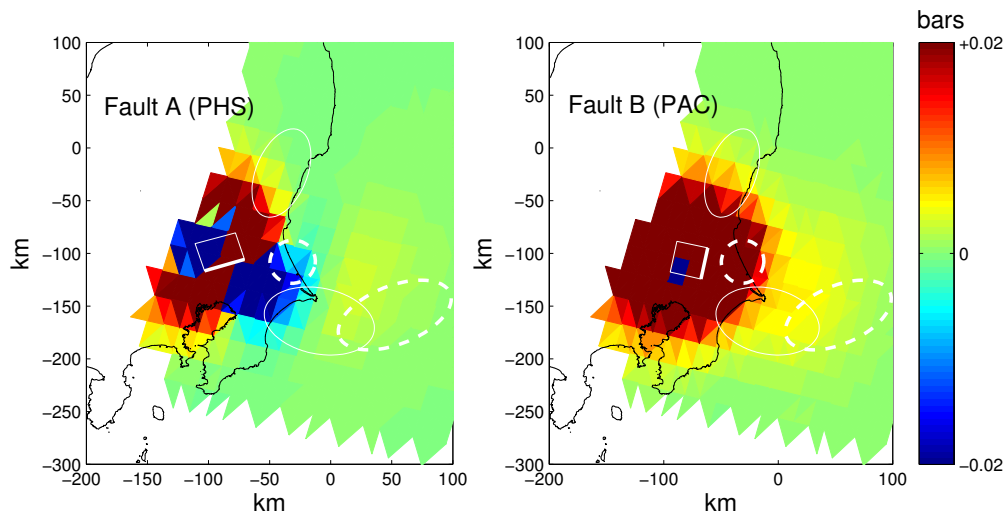
FIGURE 5.11 – Coulomb stress change on fault A (left) and fault B (right) generated by triangular dislocations paving the PAC plate, for 1 m of dip-slip for each dislocation. We map the value of this stress change created by a given triangular dislocation at the location of this triangle. The locations of maxima of afterslip are shown with thin white ellipses (Perfettini and Avouac, 2014) and with thick dashed white ellipses (Ozawa et al., 2012).

We calculated the change in Coulomb stress for three slip models of the 2011 ruptures : (1) the Ide et al. (2011) solution plus the M7.9 tapered slip dislocation of Toda and Stein (2013) ; (2) the variable slip azimuth and (3) the fixed slip azimuth solutions of Perfettini and Avouac (2014). For cases (2) and (3), the slip corresponds to the cumulative slip over 1 day, thus effectively including the M7.9 aftershock. Results are summarized in Table 5.1. The two models of Pefettini and Avouac (2014) are thus coherent with the observed rate increases on both faults A and B.

Afterslip on the Pacific slip interface is found south of the main rupture, as well evidenced by the clockwise rotation of GPS displacements in the Kanto region, compared to the co-seismic displacements (Figure 5.7). Local maxima in the post-seismic slip on PAC are effectively found both by Ozawa et al. (2012) and by Perfettini and Avouac

Model	Fault A	Fault B
1	-0.15	1.42
2	1.02	0.87
3	0.28	1.03

TABLE 5.1 – Co-seismic Coulomb stress changes in bars for a friction coefficient of 0.4, calculated on faults A and B. The three models are described in the text.

(2014), albeit with differences in their exact locations, cf. Figure 5.11. These maxima yield from 0.8 to 1.1 m (Perfettini and Avouac, 2014) and from 1 m to less than 2 m (Ozawa et al., 2012) of slip, for 279 days and 214 days, respectively. On top of this afterslip, slow slip on the Philippine Sea plate off Boso occurred at the end of October 2011 with a maximum slip of 0.3 m over about a week time (Hirose et al., 2014).

Afterslip on PAC acts to further load fault B. On the contrary, fault A is unloaded by -0.43 to -0.13 bars for the variable and fixed slip azimuth solutions of Perfettini and Avouac (2014), and an unknown (but negative) amount for Ozawa et al. (2012) based on the location of the closest maximum in a strong negative contribution lobe, see Figure 5.11. This can explain why the rate of REs on fault A has decayed at a faster pace than on fault B. We moreover note that the RE time series on fault A exhibit, from the end of 2012 to the end of 2013, a rate lower than the pre-Tohoku rate, consistent with the unloading by afterslip (Figure 5.10).

We estimate how co and post-seismic slip, including accelerated creep on faults A and B, have affected stress on the locked portion of the Philippine Sea plate in Kanto. We compute the individual changes in Coulomb stress on the source of the 1923 M7.9 Kanto earthquake of Matsu'ura and Iwasaki (Matsu'ura and Iwasaki, 1983), for 1 m of dip slip on each triangular dislocation of the modeled PAC upper surface, see Figure 5.12. Co-seismic slip acted to decrease failure stress on the fault by -0.005 bars for all three co-seismic models, while post-seismic slip, including accelerated creep on faults A and B, has the opposite effect of positively loading this fault : +0.019 bars (post-seismic), +0.002 bars (creep on A after 1 year), and less than 0.001 bars (creep on B after 1 year). Moreover, the October 2011 off-Boso SSE also contributed to add +0.014 bars of Coulomb stress on this fault. These changes are all small, and are averaged over the 95 km × 54 km fault surface. Larger changes are thus expected locally on the fault, although they remain modest ; for example, the 2011 Boso SSE generated a maximum of +0.06 bars at the eastern tip of the fault. The stress changes on the 1923 Kanto earthquake fault caused by the 2011 mainshock and subsequent slip events, are thus barely significant. They can for example be compared to the stressing rate corresponding to an earthquake

cycle with 30 bars of stress drop and 500 years of return time, hence 0.06 bars / year. The stress perturbations thus amount to less than a year of inter-seismic loading. This estimation however relies on the limited spatial extents of our faults A and B. Accelerated creep on much larger surfaces would have a stronger impact in these stress calculations.
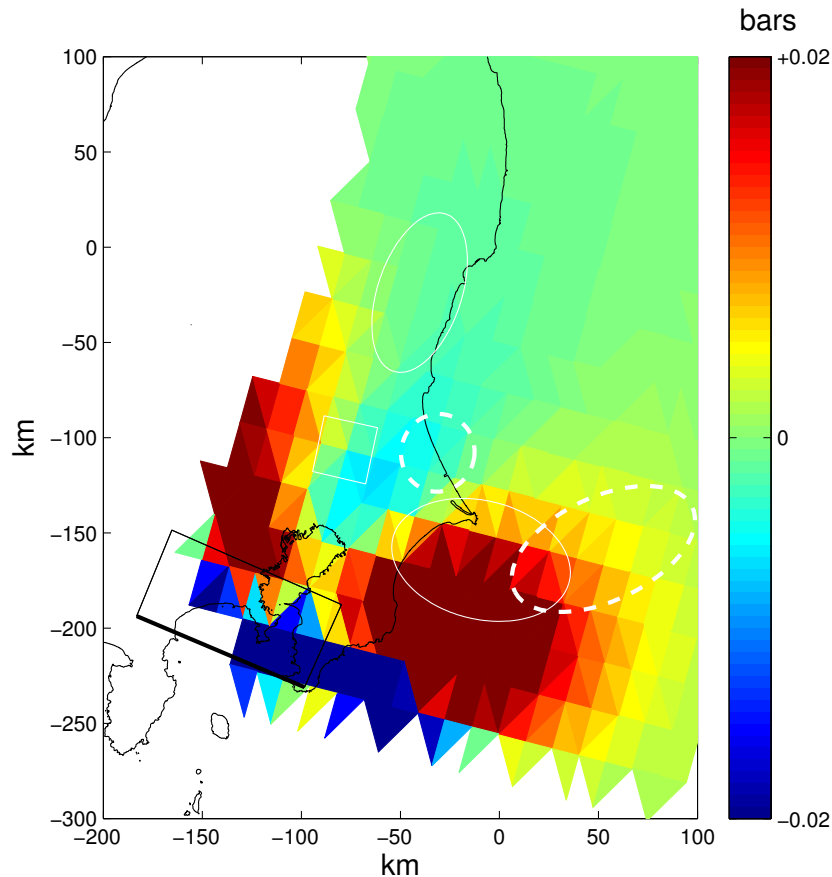
FIGURE 5.12 – Same as Figure 5.11, but for the updip locked portion of the Phillipine Sea plate that ruptured during the 1923 M7.9 earthquake (25° dip, 294° strike, and 144° rake ; Matsu'ura and Iwasaki (1983)).

5.7   Conclusions

Following the 2011 M9.0 Tohoku earthquake, a remarkable increase in seismicity has affected the Kanto region. However, this increased activity has relaxed to pre-Tohoku rates on crustal faults, and is in process of doing so (as of June 2014) on deep sections of the Philippine Sea plate characterized by creep and repeating earthquakes. On the

contrary, very little relaxation is observed on creeping portions of the Pacific plate ; also, GPS inversions find secondary maxima of afterslip on this plate in the Kanto region. However, this acceleration of creep and silent slip, as well as direct co-seismic effects, only little affect the stress state of the hypothesized source fault of the 1923 Kanto earthquake, that correspond to the strongly locked up dip portion of the Philippine Sea plate in this region.

5.8 New observations

In order to study the behavior of the seismic rate following June 2014, we extended the analysis up to November 2015. We applied the same method than presented in Chapter 4 in order to detect new REs.

5.8.1 Evolution of seismicity from 2004 to 2015.

We separated the ouput catalog into REs on PHS and on PAC according to the group barycenter depths and calculated the cumulative number of events for both plates (figure 5.13). By the end of 2015, both plates still present a seismic rate higher than before the Tohoku earthquake.
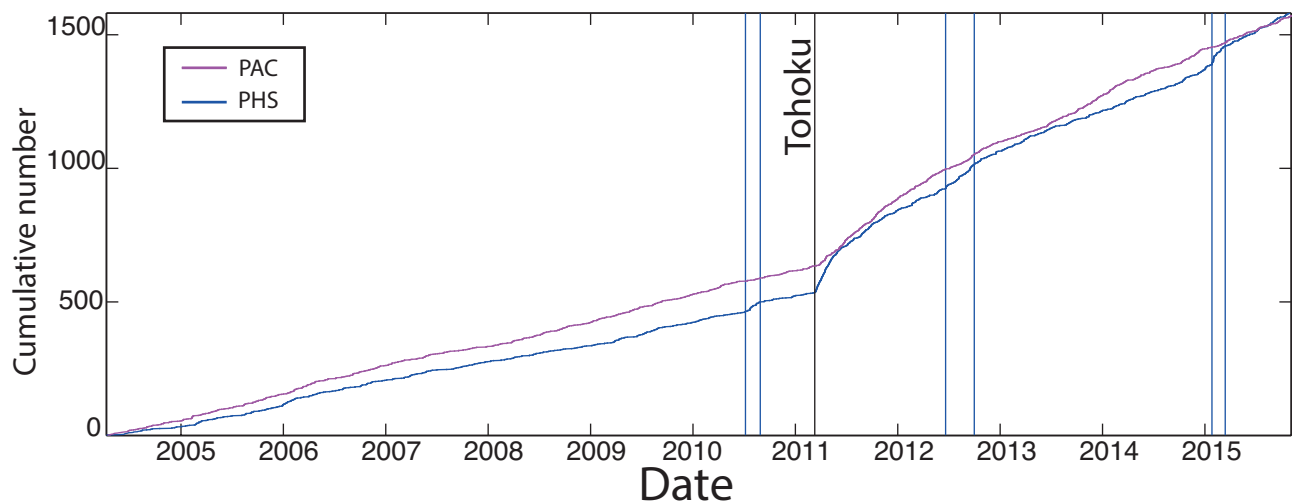
FIGURE 5.13 – Cumulative number of REs on PAC (pink) and PHS (blue) from April 2004 to November 2015. The black line indicates the occurrence of the Tohoku earthquake. The blue vertical lines indicate the time of a seismic rate increase on PHS.

Furthermore, three accelerations of the seismic rate occurred on PHS concomitant with decelerations on PAC. The seismicity activated during these increases is located in the entire studied area where the majority of REs occur (figure 5.14).
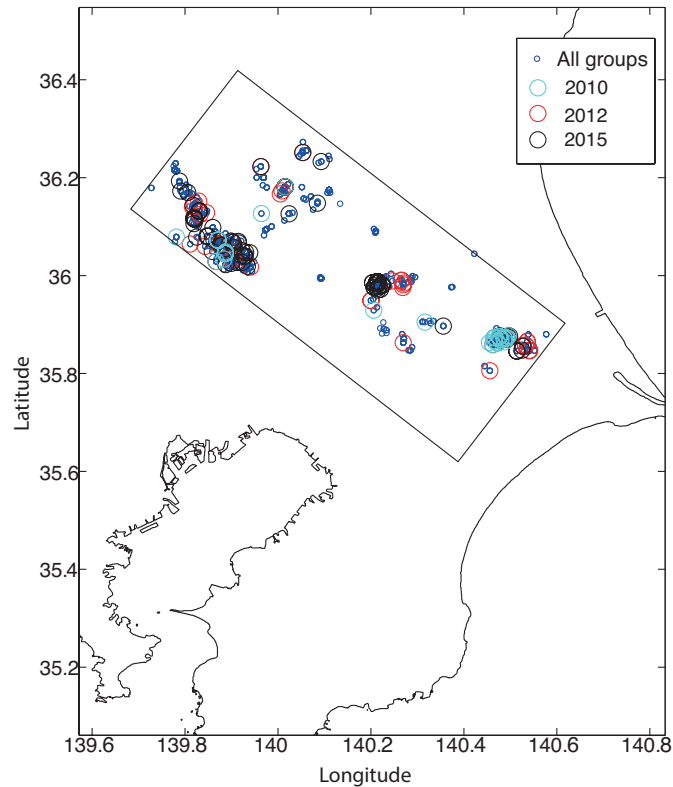
FIGURE 5.14 – Localisation of the groups affected by the increases in seismicity on PHS in 2010 (cyan), 2012 (red) and 2015 (black). The blue dots indicate the location of all the groups of REs.

We compute the change in Coulomb stress at the center of a fault located on PAC for a friction coefficient of 0.4, that would result from 1 m of pure dip-slip on individual triangular dislocations paving the rectangular area of figure 5.14. As previously, we used the same triangular meshes as as Perfettini and Avouac (2014), that are based on the modeled plate surface of Hayes et al. (2012). We find a negative Coulomb stress change of -0.083 bars which is too small to explain such a quiescence of PAC. In any case, transient slip on the northwestward-dipping PHS would put the westward-dipping PAC into more compression, increasing friction on the interface between the bottom of PHS and the top of PAC. This would inhibit slip on PAC locally, in the same way that PAC is

expected to inhibit PHS, as shown in figure 5.11. It is thus likely that both plates locally
screen each other, due to their respective geometries.

5.8.2 Magnitude increase after the Tohoku earthquake.

As REs occur on repeatedly rupturing fault patches, they provide useful informations
about the nature of the earthquake cycle and on the variation of the fault rheology with
time.

Laboratory experiments evidenced that strength on a fault plane increases during
the inter-seismic period (Dietrich, 1972; Beeler et al., 1994). This gain in static friction
implies larger stress drops and thus, larger seismic moment for longer stationary contact.

Several studies observed the link between the seismic moment (Mo) and the recur-
rence time (Tr) of REs. Vidale et al (1994) analysed 18 REs that occurred on the Calave-
ras fault and found that the event with the longest Tr tend to have about 15%. This was
further supported by the work of Marone et al., (1995) who found that the stress drop
increases of 1 to 3MPa per decade increase of Tr. The analysis of Nadeau and McEvilly
(1999) found an 18% increase in Mo for a 10-fold increase in the preceding Tr during
a transient slip in the Parkfield segment of the San Andreas fault that lasted about 10
years.

The analysis of 194 groups of REs on the Calaveras fault evidenced that the trend
between Mo and Tr varies with depth (Peng and Ben-Zion, 2005). More specifically, they
found a negative trend between Mo and Tr for the deeper REs that were close to a
large slip patch that broke during the 1984 M6.2 Morgan Hill earthquake. The authors
hypothesized that higher strain rates are responsible for transient embrittlement and
strengthening of the fault patches close to the mainshock rupture zone, leading to higher
Mo for shorter Tr in the early postseismic period.

Detailed observation of the trend between Tr and Mo was made after the 2004 Park-
field earthquake by Chen et al., (2010). They found both positive and negative trends in
this area and compared them with the behavior of REs in rate-and-state fault models of
Chen and Lapusta (2009). They conclude that, in their model, the Mo vs Tr trend is not
controlled by the increase of static friction but rather by the friction properties of the
patch and the interactions between seismic and aseismic slip. Only a few studies focus on
the trend between Mo and the loading rate on an asperity. Uchida et al., (2015) analysed
the behaviors of REs in northeastern Japan subduction zone for the period from July
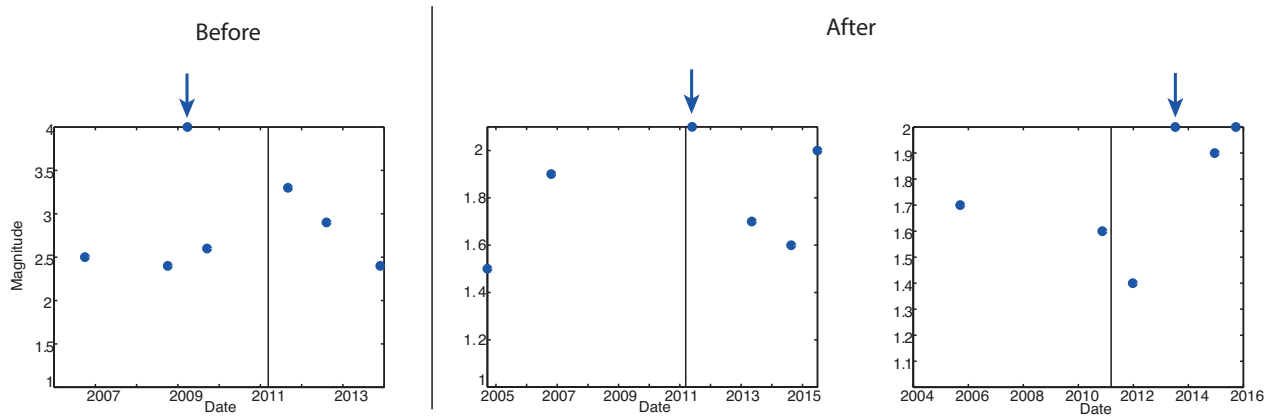
FIGURE 5.15 – Definition of the maximum magnitude of the groups of REs before (left), right after (middle) and after the Tohoku earthquake (both middle and right).

1984 to the end of 2011 and found that the magnitudes of REs increased by an average of about 0.3 after the Tohoku earthquake. They also focused on a the Kamaishi repeating sequence which magnitude also increased after the megathrust earthquake.

In this section, we examine the time of occurrence of the maximum magnitude of the groups of REs both on PAC and PHS in the Kanto region in order to analyse the earthquake size variations of asperities that lie in the limit of a megathrust rupture zone.

First, we define the maximum magnitude according to the JMA catalog for all the groups of that had at least 3 REs as defined in figure 5.15.

The majority of groups present their maximum magnitude after the Tohoku earthquake for both plates and the maximum occurs roght after the Tohoku earthquake for both PAC and PHS (red circle in figures 5.16 and 5.17).

However, the dynamics on PAC is different than on PHS : the maximum magnitudes tend to be clustered on PAC, with clusters separated by periods where no maxima are present. On the contrary, the maximum magnitudes appear less clustered on PHS and the number of maximum magnitudes increases more rapidly after the Tohoku earthquake than on PAC. Interestingly, the periods of seismic acceleration and quiescence on PHS and PAC respectively, correspond to times when less maxima occur on PAC and more maxima occur on PHS. In total (PAC+PHS), 116 groups have their maximum magnitude before the Tohoku earthquake and 219 after it, including 76 that had their maximum on their first occurrence after the megathrust event.

We test the null hypothesis that maximum magnitude occur more frequently just after the Tohoku mainshock by calculating the number of groups that had their maximum,

FIGURE 5.16 – Top : Cumulative number of the event with a maxmimum magnitude
of the groups of REs on PAC. The black line indicates the occurrence of the Tohoku
earthquake. The blue vertical lines indicate the time of a seismic rate increase on PHS.
Bottom : time of occurrence of maximum magnitude of the groups of REs on PAC. The
red circle indicates the maximum of the magnitude maxima.

before, after and on their first occurrence after the megathrust earthquake for 1000
trials and randomly reshuffling the magnitude values among each group (figure 5.18).
Acccording to these distributions, we should see more maximum magnitudes before the
Tohoku earthquake than after. The observed numbers (triangle on figure 5.18) are clearly
off the expected distributions of our null hypothesis, proving that the tendency of the
maximum magnitude to occur after the mainshock is significant.

We also test the probability for the maximum magnitude event to occur within a
certain time window, for our null hypothesis. For every group, we count the number of
events that occur in the window (N_{in}) and out (N_{out}), keeping only the groups for which
$N_{in} \geq 1$ and $N_{out} \geq 1$. For G groups, G_{in} have their maximum inside the window and
G_{out}. If there are several events of a group with the same maximum magnitude inside and
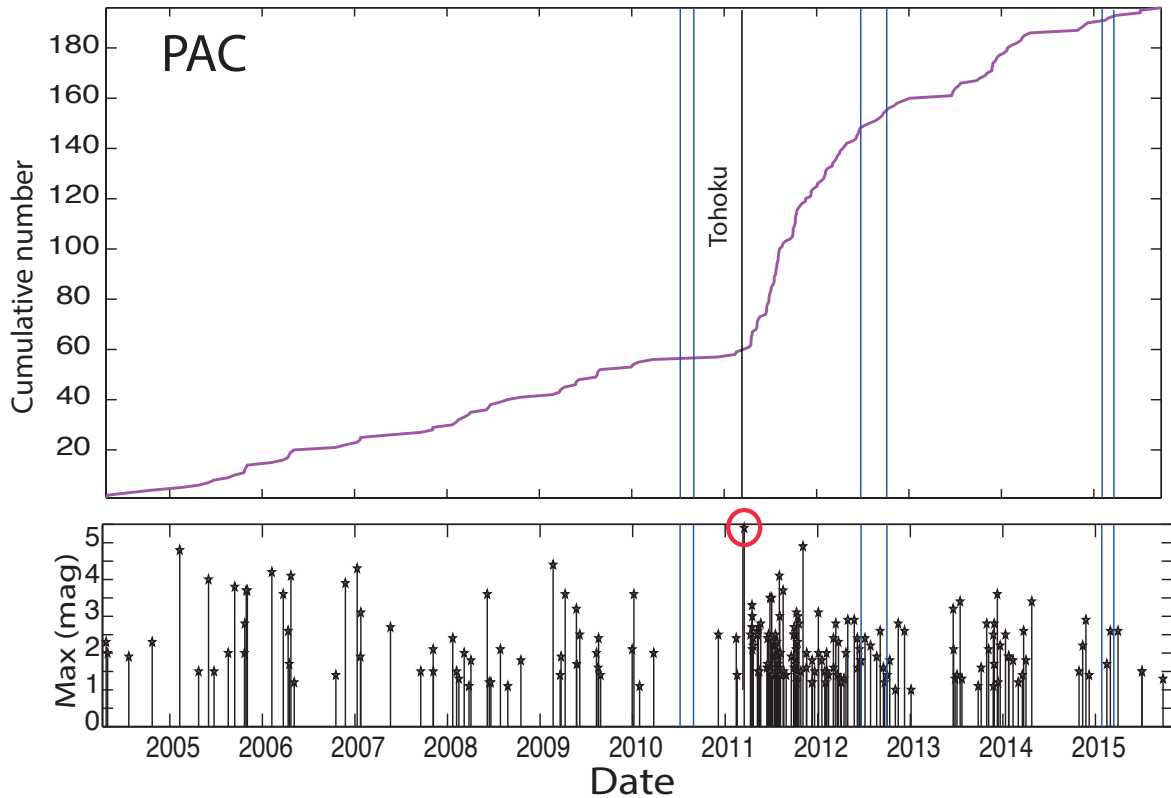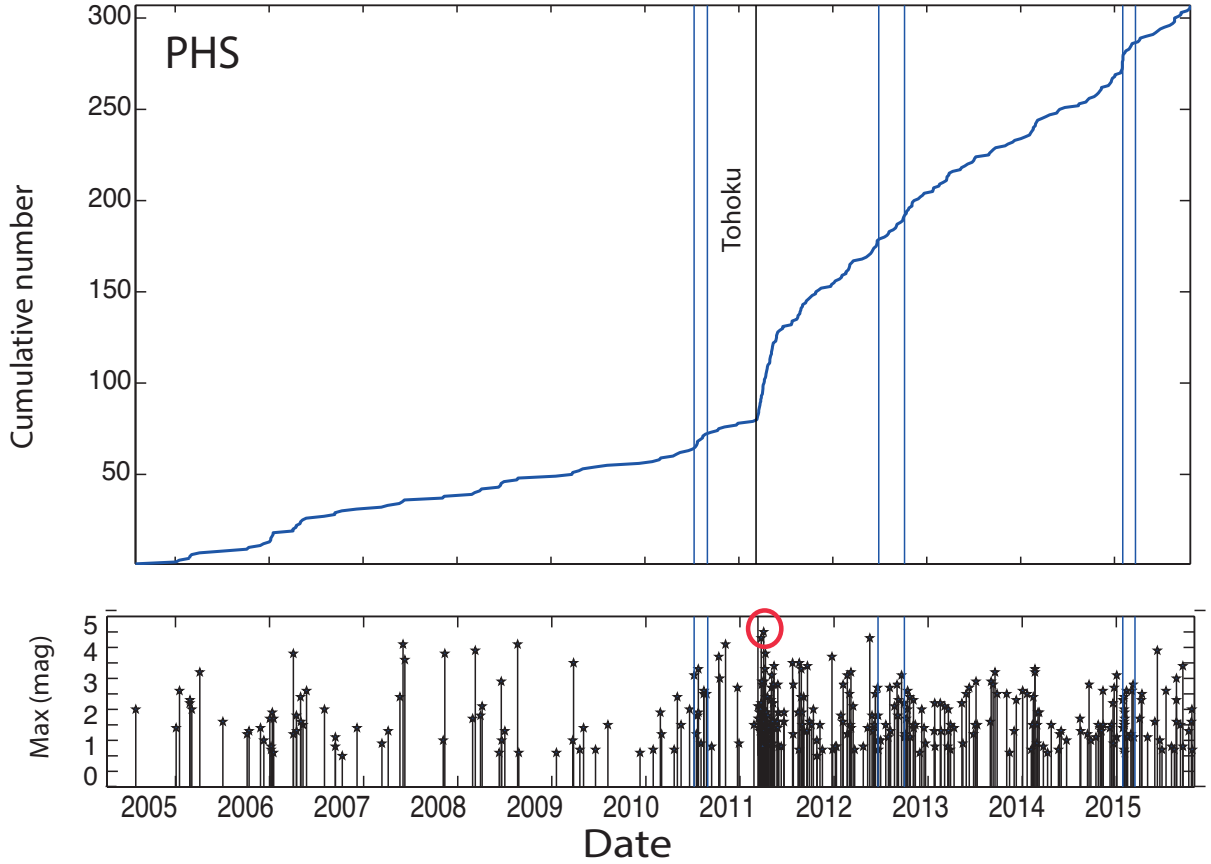
FIGURE 5.17 – Top : Cumulative number of the event with a maxmimum magnitude of the groups of REs on PHS. The black line indicates the occurrence of the Tohoku earthquake. The blue vertical lines indicate the time of a seismic rate increase on PHS. Bottom : time of occurrence of maximum magnitude of the groups of REs on PHS. The red circle indicates the maximum of the magnitude maxima.

outside the window we do not keep the group. It is then possible to compare G_{in} with G_{in}^0, the expected number if, for every group, the maximum magnitude occurs at random (within the N events of the group), i.e, our previous null hypothesis. The probability that, for a group with N_{in} and N_{out} events, the maximum magnitude occurs during the time window is : $N_{in}/(N_{in}+N_{out})$. For G groups, the number G_{in}^0 follow a Poisson distriution of mean $\Lambda = \sum_{i=1}^{G} N_{in}/(N_{in}+N_{out})$. We can compute the probability P that the number G_{in} can be random by summing : $P = P(G_{in} \mid \Lambda) + P(G_{in} + 1 \mid \Lambda) + ...$, with $P(n \mid \Lambda)$ given by the Poisson distribution.

We compute the probability to have the maximum magnitude during a time window from the Tohoku earthquake to the end of the catalog and obtain $P = 6.6 * 10^{-3}$ and
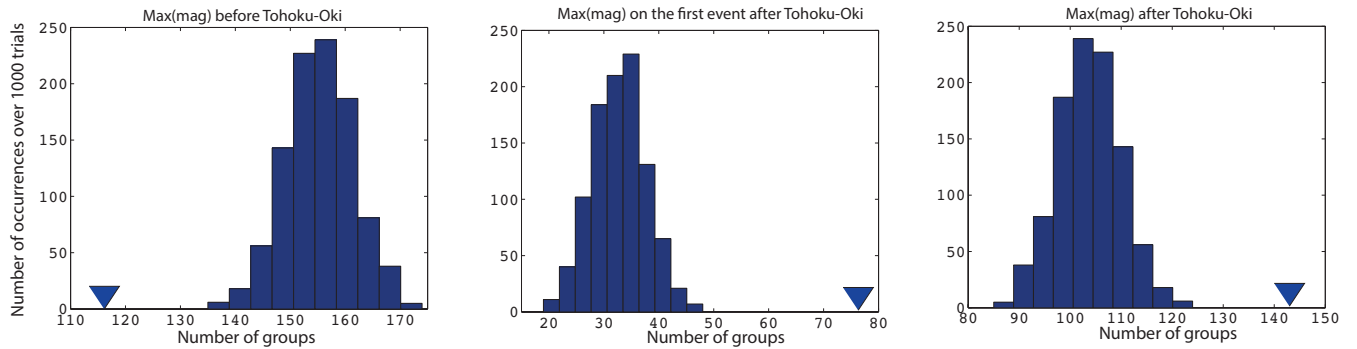
FIGURE 5.18 – Number of groups with their maximum magnitude occurring before (left), with the first occurrence after the Tohoku earthquake (middle), after the Tohoku earthquake (right) over 1000 trials, after randomly reshuffling the magnitude for each group.

$\Lambda = 117.7$. We do the same calculation with a sliding window of 60 days (two months, figure 5.19). The probability to obtain the maximum magnitude by chance is smallest just after the Tohoku earthquake (figure 5.19). We also observe that N_{in} is greater than Λ after the Tohoku earthquake. Thus, the observation of maximum magnitudes after the Tohoku earthquake is very unlikely due to chance.
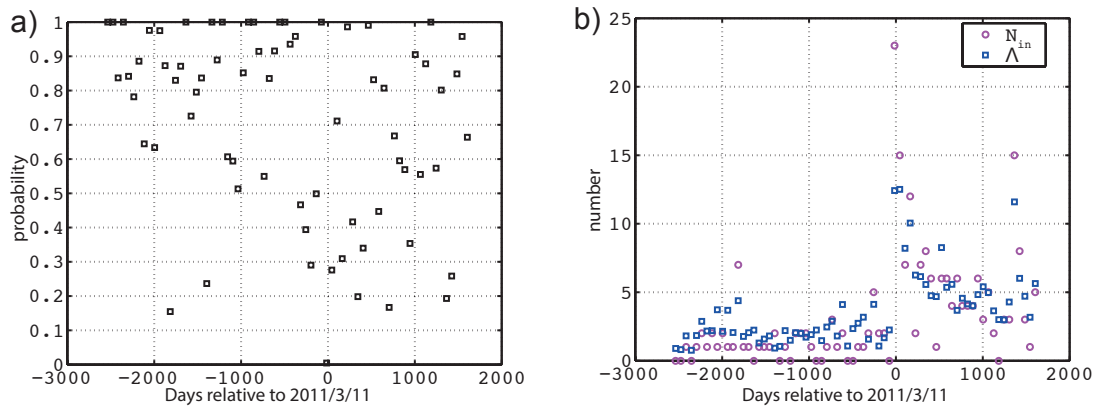
FIGURE 5.19 – Analysis over a sliding window of 60 days ; a) Probability P to observe at least N_{in} by chance, b) N_{in} and Λ.

We thus conclude that anomalously large magnitude characterize the occurrences of REs after the M9.0, the more so just after it (for the first two months).

We analyse the behavior of each group of REs individually after the Tohoku earthquake and calculated whether or not their time of recurrence shortened after the megathrust event. According to the hypothesis that an asperity records the surrounding

	PAC	PHS
deceleration and max(mag) before the Tohoku earthquake	2	3
deceleration and max(mag) after the Tohoku earthquake	1	3
acceleration and max(mag) before the Tohoku earthquake	32	30
acceleration and max(mag) after the Tohoku earthquake	2	6

TABLE 5.2 – Different behaviors of the groups with more than 3 REs that passed the selection of equation 5.1.

slip, shortening (lengthening) of the recurrence time indicates a slip rate acceleration (deceleration).

We do the analysis of acceleration or declaration for the groups that contain more than 3 events and which satisfy the following criterion :

$$\frac{N_{after}}{\Delta t_{after}} > 2 * \frac{N_{before}}{\Delta t_{before}}, \tag{5.1}$$

with N, the number of events and Δt, the time of interval between two successive events of a same group.

In total, we keep 38 and 42 groups on PAC and PHS, respectively which behaviors are listed in table 5.2.

We show the locations of the different groups and behaviors in figure 5.21 and 5.20. On PHS, groups that present a shortening of their time interval are mainly located near top interface of the slab, compared with the groups that are characterized by a lengthening of their time interval. Furthermore, the groups presenting a shortening of their time interval are found throughout the entire surface of the slab from 35 to 55 km except for a patch at about 40 km that is less seismic.

The groups that present a lengthening of their time interval are mainly located at a latitude of 36.05^o and depth of around 47 km. The fact that the acceleration of slip is mainly seen at the surface of the slab might indicate that the postseismic slip does not affect the slab at depth.

On PAC, the majority of REs are clustered between 65 and 70 km depth, and between longitude of 140 and 140.1^o indicating the presence of an aseismic zone updip coherent with the low coupling in this area (Uchida et al., 2009). Only three groups present a lengthening of their time interval and they are found more to the south and at shallow depth compare to the cluster of accelerating REs.
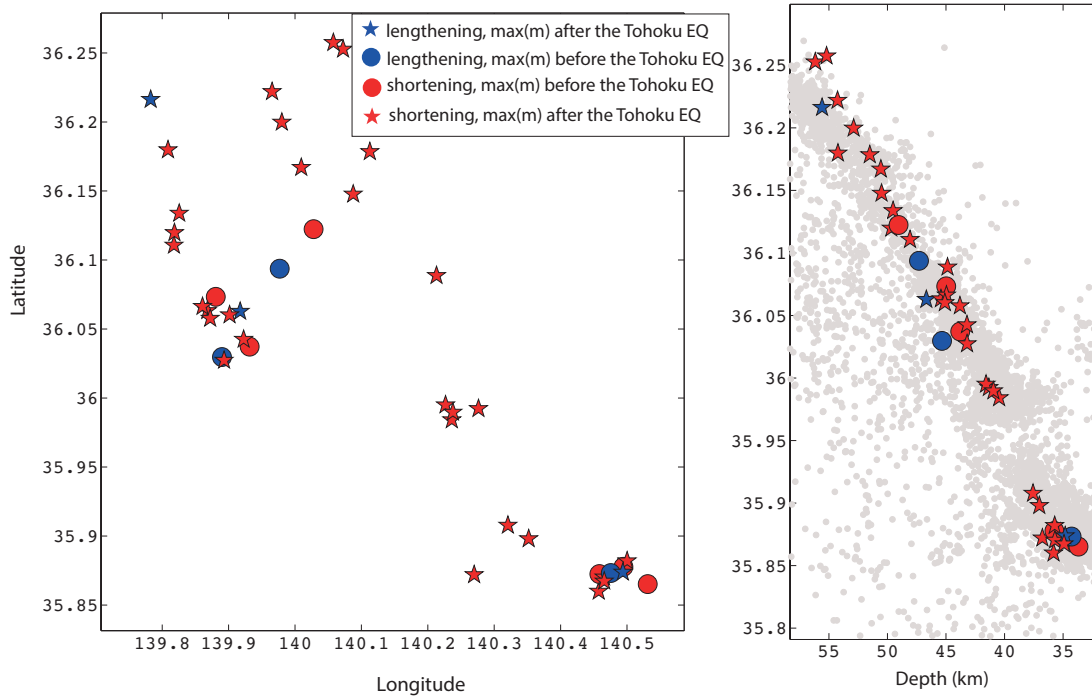
FIGURE 5.20 – Location of the groups of REs on PHS a) on a map and b) on a cross section. The star indicates that the maximum magnitude occurs after Tohoku earthquake. Blue and red dots/stars indicate a lengthening and shortening of the recurrence time, respectively.

Two phenomena are coincident here : 1) the aseismic slips present on both plates that provoke a shortening of recurrence time of most of the groups of REs, 2) the increase of magnitude after a megathrust event that is due to an aseismic-to-seismic transition.

The critical fault length was defined by Dieterich (1986) as :

$$l_c = \nu \frac{GL}{(b-a)\sigma_n} \tag{5.2}$$

With G the shear modulus of the media and ν a nondimensional parameter that depends on the shape of the fault. If the asperity length is smaller than l_c, rupture cannot take place. Uchida et al., (2015) proposed a model where an unstable medium is surrounded by a conditionally stable field and they both are contained in a compliant zone (a - b slightly positive). Under large loading rate, such as the one caused by the postseismic slip of the Tohoku earthquake, the unstable zone breaks along with the conditionally stable and the compliant field leading to a bigger rupture length that is
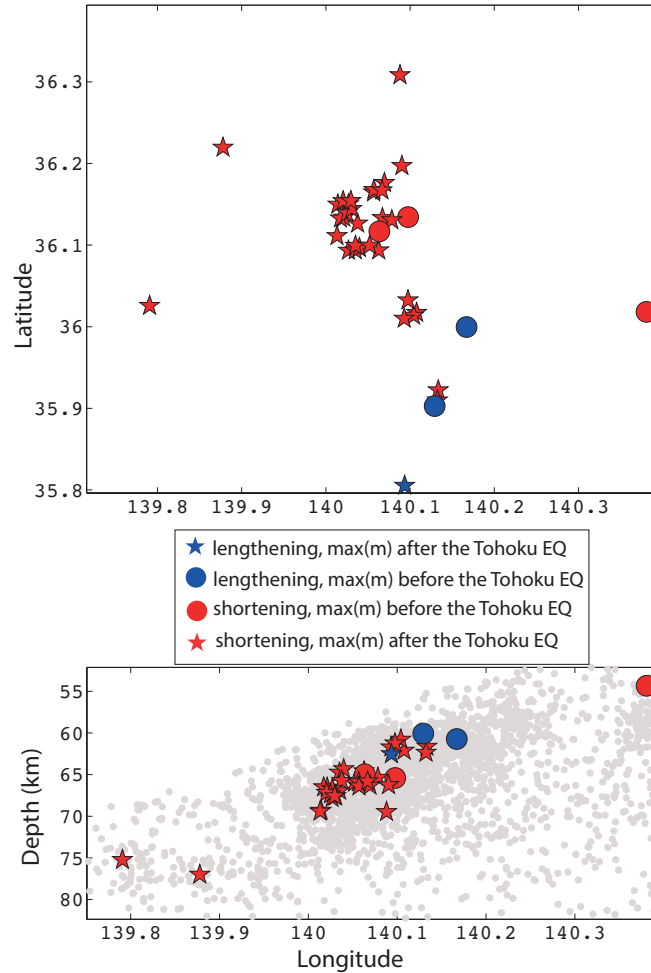
FIGURE 5.21 – Same as figure 5.20 on PAC.

usually characterized by an aseismic slip behavior. Indeed, in the Tohoku rupture zone, locked asperities might correspond to only 25% of the size of the rupture zone as inferred from the comparison between GPS data and earthquake simulations (Johnson et al., 2015).

The presence of fast loading rates can perturbate the earthquake sizes. This observation implies that the conditionally stable fields surrounding an asperity is important when regarding the transition aseismic-to-seismic slip. Furthermore, Kanto subduction zone is located at around 330 km from the Tohoku hypocenter which confirms the observation of Uchida et al., (2015) of the wide distribution of magnitude-increased repeaters after the Tohoku earthquake. The occurrence of a postseismic slip on both plates and the

fact that the coupling in this area is low indicates that the plates present large aseismic patches. The presence of such patches might explain why the rupture of the Tohoku earthquake stopped propagating in this zone. Furthermore, the PHS might have played the role of a barrier to prevent the northeast viscoelastic material flow in the mantle wedge induced by the Tohoku earthquake (Hu et al., 2016).

5.8.3 The lack of periodicity of the REs in Kanto.

The REs in Kanto area do not show period occurrences either before or after the Tohoku earthquake. This is quite surprising since REs are believed to record the tectonic loading, we should expect period time interval. This periodicity was observed for some REs in Japan (Igarashi et al., 2003; Kimura et al., 2006). However, the authors defined the REs by using a cross-correlation threshold of 0.95 and without taking into account rupture overlap. REs were first and largely studied in Parkfield area (Nadeau et al., 1995; Nadeau and McEvilly, 1997; Nadeau and Johnson, 1998; Nadeau and McEvilly, 1999). In 2009, Lengliné and Marsan showed that only 5% of the RE groups presented non periodic behavior explained by a dominance of interactions between the studied asperities. They computed the Coefficient of Variation (COV) for their groups of REs, defined as the ration, for a repating sequence, of the standard deviation of the intervent time over the mean intervent time. A COV of 0 characterizes a perfectly periodic sequence whereas a COV of 1 implies a Poisson sequence. They found COV values ranging from 0.48 to 0.52 (according to their REs selection criterion) for 95% of their RE groups. In Kanto, we obtain a mean COV of 0.65 considering all the groups with at least 3 REs that occurred before and after the Tohoku earthquake (figure 5.22). We also compute the COV for events that occurred only before or only after the Tohoku earthquake and obtain a mean COV of 0.61 and 0.62, respectively, which indicates that the Tohoku earthquake did not affect the REs periodicity in Kanto area.

Lengliné and Marsan (2009) analyzed the spatial densities of periodic and non-periodic earthquakes. The periodic groups were thighlty clustered at the barycenter of the asperity whereas the non-periodic earthquakes occurred randomly in the source area of the repeating sequence. This was also observed in Taiwan where two groups of REs were analysed (Chen et al., 2016). One group was periodic and presented rupture overlap. On the contrary, the group characterized by non-periodic behavior revealed distinct rupture characteristic and ruptures that did not overlap. These observations of different rupture location for non-periodic groups of REs suggests that the strength of the asperity was
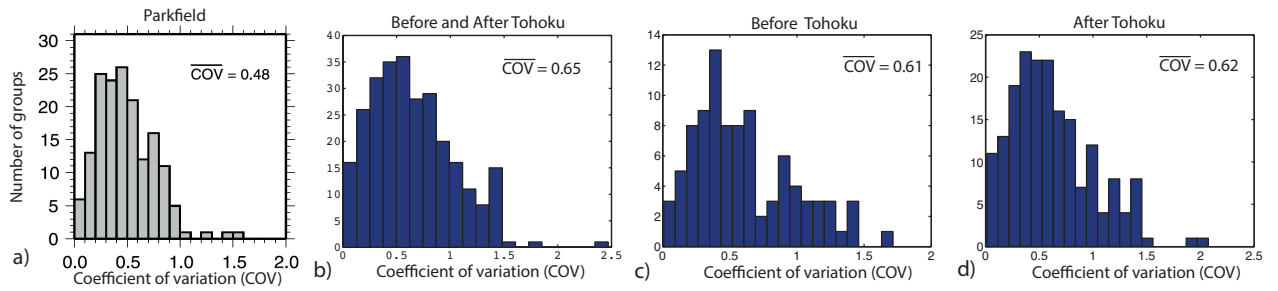
FIGURE 5.22 – a) COV distribution for Parkfield REs (from Lengliné and Marsan (2009), b) COV distribution for REs in Kanto that occurred before and after the Tohoku earthquake, c) COV distribution for REs in Kanto that occurred only before the Tohoku earthquake, d) COV distribution for REs in Kanto that occurred only after the Tohoku earthquake. The mean COV is given in every histogram.

not fully recovered between two following events. Thus the irregularity of earthquake recurrence would be linked to stress and strength heterogeneity. Another explanation of such different behavior between the crustal REs in Parkfield and in the subduction zone can also come from the difference in temperature and rheology. The medium surrounding the asperities in the subduction zone might be less slip-strengthening than the medium surrounding the asperities in Parkfield, facilitating the loading of an asperity on its neighbours, thus promoting interactions between asperities. Another difference can be that the asperities might be less isolated in Kanto than in Parkfield. Finally, episodes of transient slip might also occur locally which load only some asperities.

To conclude, the seismic activity is still high in Kanto area 4 years after the Tohoku earthquake. Even if far from the hypocenter, two aseismic slip occurred and were still going on during these four years. Furthermore, this intense slip affected the conditionally stable zones which led to an increase in magnitude of REs after the Tohoku earthquake. The two plates seem to be anti-correlated even though the physical reason remains unclear. The complexity of the area and the interactions between asperities lead to a lack of periodicity of REs.

Chapitre 6

Discussion and Perspectives

The aim of the study is the analysis of the interactions between seismic and aseismic slip during the entire seismic cycle. The Japanese subduction zone is one of the most instumented area in the world. However, the location of the earthquakes far from the coast in the Tohoku area and the double subduction zone in Kanto and Boso make the analysis of geodetic inland signals difficult.

The use of seismic signal can thus bring new insights on the interactions between seismic and aseismic slip by analyzing repeating and/or resembling earthquakes.

In this dissertation, we used two methods to detect 1) resembling and/or repeating earthquakes, based on the analysis of the cross-spectral density matrix using the network as an array, 2) repeating earthquakes based on the cross-correlation of the seismic signals between pairs of stations. Both methods can be improved by a thorough analysis of the noise signal as presented in section 3.6.2.

6.1   Interactions before a megathrust event.

We saw that the first method allows to detect small events hidden in a noise level up to twice the signal amplitude. Specifically, we detect events at both low (below 10 Hz) and high frequency (above 14 Hz). The events detected at high frequency were mainly detected using the M4.8 to M6 Tohoku foreshock. Furthermore, we were able to see that the area was not fully coupled from Janurary 2010 to March 2011. The burst-like seismicity of events detected at high frequency and the migration episodes of events

detected at low frequency in a zone that was not fully coupled can evidence several slip transients and/or a casca ding rupture phenomenon.

If we focus on slip transient, we can wonder what role did it played in the triggering of the Tohoku earthquake ? More generally, is it possible to relate the size of the transient slip that precede a large event with its future rupture zone ? To answer these questions, we need to estimate the spatial extension of the transient slip and its amplitude. As mentionned in Chapter 3, the method is based on the analysis of templates present in a given area. Thus, we can observe the seismic history in a given zone only, especially in the rupture zone of the M4.8 to M6 events that occurred before the Tohoku earthquake. The aseismic slip that we evidence with our observations might thus have a larger extension than what we see in this study.

Thus, using this detection method, it is possible to characterize the seismicity that occurs on the future rupture zone of large events. However, this technique does not allow to relocate the detected events because of the linear combination applied on the continuous signals. We can only obtain precisions on the timing of the seismicity and observe if several sources are activated at the same time as it is the case for the events detected at high frequency.

Multiple slow-slip events up-dip from the mainshock area occurred before the 2014 Iquique, Chile Mw8.1 earthquake (Ruiz et al., 2014; Kato and Nakagawa, 2014). A Slow-Slip Event also occurred in the Mexican subduction zone before the 2014 Papanoa earthquake and was observed in the GPS data (Radiguet et al., 2016). What about the crustal faults ? The 1999 Izmit, Turkey earthquake was preceded by a slip transient episode (Bouchon et al., 2011).

In Italy, the long foreshock sequence which led to the 2009 L'Aquila earthquake became a subject of heated national debate (Chiaraluce, 2012; Valoroso et al., 2013). More recently the damaging 2016 Kumamoto earthquake which struck inland Japan was also preceded by a foreshock sequence (Kato et al., 2016).

What controls the foreshocks sequence ? Cascading rupture or transient slip episodes or both ? Is the occurrence of such slip transients systematic before large subduction events ? It has been shown that intraplates events present less seismic increase before their occurrence than interplates earthquakes (Bouchon et al., 2013). This also applies to continental faults as in Parkfield case where no preseismic phase was observed before the 2004 earthquake. This might be due to the fact that Parkfield is not as large as the subduction earthquakes that present a preseismic phase or maybe because a part of

the segment which broke was already in continuous creep. Thus, the presence of such a preseismic phase appears not systematic. This can be due to the lack of detection prior large events, although Parkfield area is very well instrumented. Also, it is not clear if the seismicity increase is always followed by a large event. The use of the network as an array would help in detecting small events and thus capture the history of seismic and aseismic slip before large events and to see if they are always followed by large earthquake. However, this is quite challenging given that it requires continuous data and large computing power.

The second technique we used did not allow to detect new events since we only used waveforms of already known earthquakes. Furthermore, it does not allow to detect small events in the noise as the MDTM algorithm does. However, with this method, we can keep track of the arrival times and relocate the events in a relative way.

6.2 Interactions during a SSE.

Boso area is well-known for its recurrent SSEs that are always accompanied by a swarm-like seismicity. This gives the opportunity to search for REs that are concomittent with these transient slip episodes. The analysis of REs allowed to detect two unknown SSEs that occurred in 2005 and 2010. The observation with seismic data is confirmed by the processing of GPS records. The discovery of unknown SSEs changes the slip history in this area which is important since it has been hypothezised that the apparent reduction of time occurrence of the SSEs indicates the soon occurrence of a large event.

The burst-like seismicity that accompanies the newly detected events occurs at the end of the slip on the subduction zone and not during the slip as it was the case for the 2007 SSE. This indicates that the size and/or duration is different than the already known SSEs. Furthermore, the two detected SSEs present lower magnitudes than the already known ones (around 5.8 and 6.1, respectively). In this study, we show that the slip history is more complex than previously thought. Experimental study on the distribution of the slip between successive SSEs can bring new insights on the differences between successive SSEs observed in this study.

The detection of SSEs using REs appears to work well but one may wonder about the limit of resolution we can obtain with this technique. We see that, for Boso subduction zone, we identified a SSE in 2005 that appears smaller than the 2010 one. The displacement due to the 2005 SSE is smaller than the noise level of GPS data. Thus,

this event is in the resolution limit and it might not be possible to detect SSEs with a magnitude lower than 5.7 using both GPS and seismic data, at least with the seismic and GPS signal processing we applied in this study.

Also, this method is not applicable to all regions that undergo SSEs. For example, in Bungo Channel, short-term SSEs occur and last around one week but only tremors were detected there. This might be due to the fact that the SSEs in Bungo Channel occur at greater depth than the ones in Boso (40 km and 15 km, respectively) so the plates have different temperatures. Specifically, the average geothermal gradient beneath the Boso Peninsula is 20ºC/km and 40ºC/km in Bungo Channel (Tanaka et al., 2004).

Another place where we can use the REs as a detection technique for SSEs is New-Zealand at the Gisborne and Hawke's Bay area where SSEs occur at shallow depth (Wallace and Beavan, 2010; Wallace et al., 2016).

6.3   Interactions after a megathrust event.

The analysis of REs in Kanto area allowed to see that the Tohoku earthquake increased the seismicity on both PHS and PAC plates and that this increase was still going on by the end of 2015. The increase of the number of REs is accompanied by an increase of their magnitudes which suggests that aseismic slips take place on both plates. Three episodes of increase of REs activity on PHS are concomittent with a quiescence on PAC in 2010, 2012 and 2015 that can not be explained by a change in stress only. We also find that the periodicity of REs is rare in both PHS and PAC as opposed to REs in Parkfield area.

The cross-correlation technique allows to analyse with a certain subtlety the changes of time of occurrence and magnitude of REs after a megathrust event. Since it is possible to relocate the events that belong to the same group of REs, it is possible to make sure that the ruptures overlap in a same group. Besides, it is possible to analyse areas where groups of REs present the same behavior (shortening of interevent time, maximum magnitude occurring after the Tohoku earthquake). We analysed only waveforms of M≥1 earthquakes and the application of this technique on the entire continuous signal should help us in detecting more REs and get a detailed history of the seismicity in Kanto area from 2004 to 2016.

6.4   Conclusion.

The use of resembling and/or repeating earthquakes allowed to see in details the interactions between seismic and aseismic slip that occur during the entire seismic cycle. Specifically, these particular types of events were used to 1) estimate the preseismic slip before a megathrust event, 2) detect SSEs, 3) characterize the changes in seismicity after a megathrust event, in a off-rupture zone. The methods we present here are at the top of the detection techniques. Their use varies according to what one is looking for : new detected events to better capture the seismic history of a zone or observe in detail the spatial and temporal behaviors of the asperities in the subduction zone due to loading increase. Both techniques can be improved either by applying a denoising algorithm or by analyzing the continous signal when applying the cross-correlation technique. We strongly believe that the seismic signals have not revealed all their secrets yet and that the use and improvement of array-based methods is an avenue to a better understanding of the deformation mechanisms at stake on faults.

Bibliographie

Aizawa, K., Sumino, H., Uyeshima, M., Yamaya, Y., Hase, H., Takahashi, H., Takahashi, M., Kazahaya, K., Ohno, M., Rung-Arunwan, T., and Ogawa, Y. (2016). Gas pathways and remotely triggered earthquakes beneath Mount Fuji, Japan. *Geology*, 44(2) :127–130.

Altamimi, Z., Rebischung, P., Métivier, L., and Collilieux, X. (2016). Itrf2014 : A new release of the international terrestrial reference frame modeling nonlinear station motions. *Journal of Geophysical Research : Solid Earth*, 121.

Ando, R. and Imanishi, K. (2011). Possibility of Mw 9.0 mainshock triggered by diffusional propagation of after-slip from Mw 7.3 foreshock. *Earth, Planets and Space*, 63(47).

Aso, N., Ohta, K., and Ide, S. (2011). Volcanic-like low-frequency earthquakes beneath Osaka Bay in the absence of a volcano. *Geophys. Res. Lett.*, 38 :doi :10.1029/2011GL046935.

Bakun, W. H. and Lindh, A. (1985). The Parkfield, California, earthquake prediction experiment. *Science*, 229 :619–624.

Bakun, W. H. and McEvilly, T. V. (1984). Recurrence models and Parkfield, California, earthquakes. *Journal of Geophysical Research : Solid Earth*, 89(B5) :3051–3058.

Beeler, N., Tullis, T. E., and Weeks, J. D. (1994). The roles of time and displacement in the evolution effect in rock friction. *Geophys. Res. Lett.*, 21 :1987–1990.

Bienvenu, G. and Kopp, L. (1983). Optimality of high resolution array processing using the eigensystem approach. *IEEE*, 31(5) :1235–1248.

Boehm, J., Werl, B., and Schuh, H. (2006). Troposphere mapping functions for GPS and very long baseline interferometry from European Centre for Medium-Range Weather Forecasts operational analysis data. *Journal Geophys. Res.*, 111(B02406).

Bouchon, M., Durand, V., Marsan, D., Karabulut, H., and Schmittbuhl, J. (2013). The long precursory phase of most large interplate earthquakes. *Nature Geoscience*, 6 :299–302.

Bouchon, M., Karabulut, H., Aktar, M., Ozalaybey, S., Schmittbuhl, J., and Bouin, M. (2011). Extended nucleation of the 1999 Mw 7.6 Izmit earthquake. *Science*, 331.

Bouchon, M., Marsan, D., Durand, V., Campillo, M., Perfettini, H., Madariaga, R., and Gardonio, B. (2016). Potential slab deformation and plunge prior to the Tohoku, Iquique and Maule earthquakes. *Nature Geoscience*, 9 :DOI : 10.1038/NGEO2701.

Brace, W. F. and Byerlee, J. D. (1966). Stick-slip as a mechanism for earthquakes. *Science*, 153 :990–992.

Brace, W. F. and Byerlee, J. D. (1968). Stick slip, stable sliding, and earthquakes—effect of rock type, pressure, strain rate, and stiffness. *Journal Geophys. Res.*, 73(18) :6031–6037.

Brudzinski, M. and Allen, R. (2007). Segmentation in episodic tremor and slip all along Cascadia. *Geology*, 35 :907–910.

Bürgmann, R., Schmidt, D., Nadeau, R. M., d'Alessio, M., Fielding, E., Manaker, D., McEvilly, T. V., and Murray, M. H. (2000). Earthquake Potential Along the Northern Hayward fault, California. *Science*, 289(5482) :1178–1182.

Campillo, M. and Ionescu, I. R. (1997). Initiation of antiplane shear instability under slip dependent friction. *Journal of Geophysical Research*, 102(B9) :20363–20371.

Chen, K., Bürgmann, R., Nadeau, R., Chen, T., and Lapusta, N. (2010). Postseismic variations in seismic moment and recurrence interval of repeating earthquakes. *Earth and Planetary Science Letters*, 299(1-2) :118–125.

Chen, K., Chen, I., and Kim, A. (2016). Can slip heterogeneity be linked to earthquake recurrence ? *Geophys. Res. Lett.*, 43.

Chen, K., Nadeau, R., and Rau, R.-J. (2007). Towards a universal rule on the recurrence interval scaling of repeating earthquakes ? *Geophys. Res. Lett.*, 34(16).

Chen, T. and Lapusta, N. (2009). Scaling of small repeating earthquakes explained by interaction of seismic and aseismic slip in rate and state fault model. *J. Geophys. Res.*, 112 :B04305.

Chiaraluce, L. (2012). Unravelling the complexity of apenninic extensional fault systems : A review of the 2009 l'aquila earthquake (central apennines, italy)penninic extensional fault systems : A review of the 2009 L'Aquila earthquake (Central Apennines, Italy). *Journal of Structural Geology*, 42 :2–18.

Chlieh, M., Avouac, J., Hjorleifsdottir, V., Song, T.-R. A., Ji, C., Sieh, K., Sladen, A., Hebert, H., Prawirodirdjo, L., Bock, Y., and Galetzka, J. (2007). Coseismic slip and afterslip of the great Mw9.5 Sumatra-Andaman earthquake of 2004. *Bull. Seism. Soc. Amer.*, 97(1A) :S152–S173.

Chmiel, M., Roux, P., and Bardainne, T. (2016). Extraction of phase and group velocities from ambient surface noise in a patch-array configuration. *Geophysics*, 81(6) :KS231–KS240.

Cifuentes, I. L. and Silver, P. G. (1989). Low-frequency source characteristics of the great 1960 Chilean earthquake. *Journal of Geophysical Research : Solid Earth*, 94(B1) :643–663.

Corciulo, M., Roux, P., Campillo, M., Dubucq, D., and Kuperman, W. A. (2012). Multiscale matched-field processing for noise-source localization in exploration geophysics. *Geophysics*, 77(5) :KS33–KS41.

Cox, H. (2000). Multi-rate adaptive beamforming (MRABF) : Sensor Array and Multichannel Signal Processing Workshop. *Proceedings of the IEEE,*, page doi : 10.1109/SAM.2000.878019.

Cros, E., Roux, P., Vandemeulebrouck, J., and Kedar, S. (2011). Locating hydrothermal acoustic sources at Old Faithful Geyser using Matched Field Processing. *Geophys. J. Int.*, 187 :385–393.

Dieterich, J. H. (1979). Modeling of rock friction : 1. experimental results and constitutive equations. *Journal of Geophysical Research : Solid Earth*, 84(B5) :2161–2168.

Dietrich, J. (1972). Time-dependent friction in rocks. *Journal of Geoph. Res.*, 77 :3690–3697.

Dietrich, J. (1978). Preseismic fault slip and earthquake prediction. *J. Geophys. Res*, 83 :3940–3948.

Dietrich, J. (1979). Modelling of rock friction : 2. simulation of preseismic slip. *J. Geophys. Res.*, 84 :2169–2175.

Dietrich, J. (1986). *A model for the nucleation of earthquake slip in : Earthquake Source Mechanics.* AGU, Washington, D. C.

Dietrich, J. (1992). Earthquake nucleation on faults with rate-and-state dependent strength. *Tectonophysics*, 211 :115–134.

Dodge, D. A., Beroza, G., and Ellsworth, W. L. (1995). Foreshock sequence of the 1992 Landers, California, earthquake and its implications for earthquake nucleation. *Journal of Geophysical Research : Solid Earth*, 100(B6) :9865–9880.

Dodge, D. A., Beroza, G., and Ellsworth, W. L. (1996). Detailed observations of California foreshock sequences : Implications for the earthquake initiation process. *Journal of Geophysical Research : Solid Earth*, 101(B10) :22371–22392.

Donne, D. D., Harris, A., Rieppe, M., and Wright, R. (2010). Earthquake-induced thermal anomalies at active volcanoes. *Geology*, 38(9) :771–774.

Dragert, H., Wang, K., and James, T. S. (2001). A silent slip event on the deeper Cascadia subduction interface. *Science*, 292 :1525–1528.

Eggert, S. and Walter, T. (2009). Volcanic activity before and after large tectonic earthquakes : Observations and statistical significance. *Tectonophysics*, 474(1-2) :14–29.

Ellsworth, W. L. and Beroza, G. (1995). Seismic evidence for an earthquake nucleation phase. *Science*, 268 :851–855.

Ellsworth, W. L. and Bulut, F. (2016). Izmit foreshocks revisited. *AGU, Fall Meeting.*

Eshelby, J. (1957). The determination of the elastic field of an ellipsoidal inclusion, and related problems. *Proc.R. Soc. London, Ser. A*, 241 :376–396.

Fujie, G., Kasahara, J., Hino, R., Sato, T., Shinohara, M., and Suyehiro, K. (2002). A significant relation between seismic activities and reflection intensities in the Japan Trench region. *Geophys. Res. Lett.*, 29(7) :1100.

Fukuda, J., Kato, A., Obara, K., and Miura, S. (2014). Imaging of the early acceleration phase of the 2013–2014 Boso slow slip event. *Geophys. Res. Lett.*, 41 :7493–7500.

Gardonio, B., Marsan, D., Lengliné, O., Enescu, B., Bouchon, M., and Got, J. (2015). Changes in seismicity and stress loading on subduction faults in the Kanto region, Japan, 2011-2014. *Journal of Geophysical Research : Solid Earth*, 120.

Gibbons, S. and Ringdal, F. (2006). The detection of low magnitude seismic events using array-based waveform correlation. *Geophys. J. Int*, 165 :149–166.

Glangeaud, F. and Lacoume, J. (1985). Corrections of seismic traces by adaptive signal processing. *Applied Signal Processing*, pages 263–266.

Glangeaud, F. and Latombe, C. (1986). Multicomponent filtering of magnetic signais. *Signal Processing*, 11(2) :133–143.

Got, J., Fréchet, J., and Klein, F. (1994). Deep fault plane geometry inferred from multiplet relative relocation beneath the south flank of Kilauea. *Journal of Geoph. Res.*, 99 :15,375–15,386.

Got, J.-L. and Okubo, P. (2003). New insights into Kilauea's volcano dynamics brought by large-scale relative relocation of microearthquakes. *J. Geophys. Res.*, 108(B7) :2553.

Grunewald, E. and Stein, R. (2006). A new 1649-1884 catalog of destructive earthquakes near Tokyo and implications for the long-term seismic process. *J. Geophys. Res.*, 111.

Harris, D. (2006). *Subspace detectors : Theory*. Lawrence Livermore Natl. Lab. Rep. UCRL-TR-222758.

Hasegawa, A. and Yoshida, K. (2015). Preceding seismic activity and slow slip events in the source area of the 2011 Mw 9.0 Tohoku-Oki earthquake : a review. *Geoscience Letters*, 2(6).

Hashimoto, C., Noda, A., Sagiya, T., and Matsuura, M. (2009). Interplate seismogenic zones along the Kuril, Japan trench inferred from GPS data inversion. *Nature Geoscience*, 2 :141–144.

Hayes, G., Wald, D. J., and Johnson, R. L. (2012). Slab1.0 : A three-dimensional model of global subduction zone geometries. *J. Geophys. Res.*, 117(B01302).

Heki, K. and Tamura, Y. (1997). Short term afterslip in the 1994 Sanriku-Haruka-Oki earthquake. *Geophys. Res. Lett.*, 24(24) :3285–3288.

Herring, T., King, R., Floyd, M., and McClusky, S. (2015). Introduction to gamit/globk. *Department of Earth, Atmospheric, and Planetary Sciences. Massachusetts Institute of Technology.*

Hino, R., Inazu, D., Ohta, Y., Ito, Y., Suzuki, S., Iinuma, T., Osada, Y., Kido, M., Fujimoto, H., and Kaneda, Y. (2014). Was the 2011 Tohoku-Oki earthquake preceded by aseismic preslip ? examination of seafloor vertical deformation data near the epicenter. *Geophys. Res.*, 35 :181–190.

Hirose, F., Miyaoka, K., and et al., N. H. (2011). Outline of the 2011 off the Pacific coast of Tohoku Earthquake (Mw 9.0) —Seismicity : foreshocks, mainshock, aftershocks, and induced activity—. *Earth, Planets and Space*, 63(1).

Hirose, H., Hirahara, K., Kimata, F., Fujii, N., and Miyazaki, S. (1999). A slow thrust slip event following the two 1996 Hyganada earthquakes beneath the Bugo Channel, southwest Japan. *Geophys. Res. Lett.*, 26 :3237–3240.

Hirose, H., Kimura, H., Enescu, B., and Aoi, S. (2012). Recurrent slow slip event likely hastened by the 2011 Tohoku earthquake. *PNAS*, 109-38 :15157–15161.

Hirose, H., Matsuzawa, T., Kimura, T., and Hisanori (2014). The Boso slow slip events in 2007 and 2011 as a driving process for the accompanying earthquake swarm. *Geophys. Res. Lett.hys. Res. Lett.*, doi : 10.1002/2014GL059791.

Hirose, H. and Obara, K. (2005). Repeating short- and long-term slow slip events with deep tremor activity around the bungo channel region, southwest japan. *Earth, Planets and Space*, 57 :961–972.

Hooper, A., Pietrzak, J., Simons, W., Cui, H., Riva, R., Naeije, M., van Scheltinga, A. T., Schrama, E., Stelling, G., and Socquet, A. (2013). Importance of horizontal seafloor motion on tsunami height for the 2011 Mw= 9.0 Tohoku-Oki earthquake. *Earth Planet. Sci. Lett.*, 361 :469–479.

Hu, Y., Bürgmann, R., Uchida, N., Banerjee, P., and Freymueller, J. (2016). Stress-driven relaxation of heterogeneous upper mantle and time-dependent afterslip following the 2011 Tohoku earthquake. *Journal of Geophysical Research : Solid Earth*, 121(1) :385–411.

Ida, Y. (1972). Cohesive force across the tip of a longitudinal-shear crack and griffith's specific surface energy. *Journal of Geophysical Research,*, 77(20) :3796–3805.

Ide, S., Baltay, A., and Beroza, G. (2011). Shallow dynamic overshoot and energetic deep rupture in the 2011 Mw 9.0 Tohoku-Oki earthquake. *Science*, 332(1426).

Igarashi, T., Matsuzawa, T., and Hasegawa, A. (2003). Repeating earthquakes and interplate aseismic slip in the northeastern Japan subduction zone. *J. Geophys. Res.*, 108(B5).

Igarashi, T., Matsuzawa, T., Umino, N., and Hasegawa, A. (2001). Spacial distribution of focal mechanisms for interplate and intraplate earthquake associated with the subducting Pacific plate beneath the northeastern Japan arc : A triple-planed deep seismic zone. *Journal Geophys. Res.*, 106 :2177–2191.

Ihmlé, P., Harabaglia, P., and Jordan, T. (1993). Teleseismic detection of a slow precursor to the great 1989 Macquarie Ridge earthquake. *Science*, 261 :177–183.

Ihmlé, P. and Jordan, T. (1994). Teleseismic search for slow precursors to large earthquakes. *Science*, 266(5190) :1547.

Iinuma, T., Hino, R., Kido, M., Inazu, D., Osada, Y., Ito, Y., Ohzono, M., Tsushima, H., Suzuki, S., Fujimoto, H., and Miura, S. (2012). Coseismic slip distribution of the 2011 off the Pacific Coast of Tohoku earthquake (M9.0) refined by means of seafloor geodetic data. *Journal of Geophysical Research*, 117 :doi :10.1029/2012JB009186.

Iinuma, T., Ohzono, M., Ohta, Y., and Miura, S. (2011). Coseismic slip distribution of the 2011 off the Pacific coast of Tohoku earthquake (M 9.0) estimated based on GPS data—was the asperity in Miyagi-Oki ruptured ? *Earth, Planets and Space*, 63 :643–648.

Ishibe, T., Shimazaki, K., Satale, K., and Tsuruoka, H. (2011). Change in seismicity beneath the Tokyo metropolitan area due to the 2011 off the Pacific Coast of Tohoku earthquake. *Earth Planets Space*, 63 :731–735.

Ishida, M. (1992). Geometry and relative motion of the Philippine Sea plate and Pacific plate beneath the Kanto-Tokai District, Japan. *J. Geophys. Res*, 97(B1) :489–513.

Ito, Y., Hino, R., Suzuki, S., and Kaneda, Y. (2015). Episodic tremor and slip near the Japan Trench prior to the 2011 Tohoku-Oki earthquake. *Geophysical Research Letters*, 42 :1725–1731.

Ito, Y., Hinoa, R., Kidob, M., Fujimotob, H., Osadab, Y., Inazuc, D., Ohtaa, Y., Iinumab, T., Ohzonod, M., Miurae, S., Mishinaa, M., Suzukia, K., Tsujif, T., and Ashi, J. (2013). Episodic slow slip events in the Japan subduction zone before the 2011 Tohoku-Oki earthquake. *Tectonophysics*, 600 :14–26.

Ito, Y. and Obara, K. (2006). Very low frequency earthquakes within accretionary prisms are very low stress-drop earthquakes. *Geophysical Research Letters,*, 33(9).

Ito, Y., Obara, K., Shiomi, K., Sekine, S., and Hirose, H. (2007). Slow earthquakes coincident with episodic tremors and slow slip events. *Science*, 315 :503–506.

Iwasaki, T., Yoshii, T., Moriya, T., Kobayashi, A., Nishiwaki, M., Tsutsui, T., Iidaka, T., Ikami, A., and Masuda, T. (1994). Precise P and S wave velocity structures in the Kitakami Massif, Northern Honshu, Japan, from a seismic refraction experiment. *Journal of Geoph. Res.*, 99(B11) :22,187–22,204.

Jensen, F., Kuperman, W. A., Porter, M., and Schmidt, H. (2011). *Computational Ocean Acoustic*. Springer-Verlag, 2nd edition.

Johson, K., Mavrommatis, A., and Segall, P. (2015). Small interseismic asperities and widespread aseismic creep on the northern Japan subduction interface. *Geophys. Res. Lett.*, 43 :135–143.

Kanamori, H. and Cipar, J. J. (1974). Focal process of the great Chilean earthquake May 22, 1960. *Physics of the Earth and Planetary Interiors*, 9(2) :128–136.

Kato, A., Fukuda, J., Nakagawa, S., and Obara, K. (2016). Foreshock migration preceding the 2016 Mw 7.0 Kumamoto earthquake, Japan. *Geophys. Res. Lett.*, 43(17) :8945–8953.

Kato, A., Igarashi, T., and Obara, K. (2014). Detection of a hidden boso slow slip event immediately after the 2011 Mw 9.0 Tohoku-Oki earthquake, Japan. *Geophysical Research Letters*, 41(16) :5868–5874.

Kato, A. and Nakagawa, S. (2014). Multiple slow-slip events during a foreshock sequence of the 2014 Iquique, Chile Mw 8.1 earthquake. *Geophys. Res. Lett.*, 41(15) :5420–5427.

Kato, A., Obara, K., Igarashi, T., Tsuruoka, H., Nakagawa, S., and Hirata, N. (2012). Propagation of slow slip leading up to the 2011 Mw 9.0 Tohoku-Oki earthquake. *Sciencexpress*.

Kato, N. (2003). Repeating slip events at a circular asperity : Numerical simulation with a rate-and statedependent friction law. *Bull. Earthq. Res. Inst.*, 78(151-166).

Kido, M., Osada, Y., Fujimoto, H., Hino, R., and Ito, Y. (2011). Trench-normal variation in observed seafloor displacements associated with the 2011 Tohoku-Oki earthquake. *Geophys. Res. Lett.*, 38.

Kimura, H., Kasahara, K., Igarashi, T., and Hirata, N. (2006). Repeating earthquake activities associated with the Philippine Sea plate subduction in the Kanto district, central Japan : A new plate configuration revealed by interplate aseismic slips. *Tectonophysics*, 417 :101–118.

Kobayashi, A. and Hirose, F. (2016). Aseismic slips synchronized with earthquakes in northern Chiba Prefecture, central japan. 69(2) :1–9.

Latour, S., Schubnel, A., Nielsen, S., Madariaga, R., and Vinciguerra, S. (2013). Characterization of nucleation during laboratory earthquakes. *Geophysical Research Letters,*, 40(19) :5064–5069.

Lay, T., Kanamori, H., Ammon, C., Koper, K., Hutko, A., Ye, L., Yue, H., and Rushing, T. (2012). Depth-varying rupture properties of subduction zone megathrust faults. *Journal of Geophysical Research*, 117 :doi :10.1029/2011JB009133.

Leeman, J., Saffer, D., Scuderi, M., and Marone, C. (2016). Laboratory observations of slow earthquakes and the spectrum of tectonic fault slip modes. *nature communications*, 7 :11104.

Legaz, A., Revil, A., Roux, P., Vandemeulebrouck, J., Gouédard, P., Hurst, T., and Bolève, A. (2009). Self-potential and passive seismic monitoring of hydrothermal activity : A case study at Iodine Pool, Waimangu geothermal alley, New Zealand. *Journal of Volcanology and Geothermal Research*, 178 :11–18.

Lengliné, O., Enescu, B., Peng, Z., and Shiomi, K. (2012). Decay and expansion of the early aftershock activity following the 2011, Mw9.0 Tohoku earthquake. *Geophys. Res. Letts.*, 39 :L18309.

Lengliné, O. and Marsan, D. (2009). Inferring the coseismic and postseismic stress changes caused by the 2004 Mw=6 Parkfield earthquake from variations of recurrence times of microearthquakes. *J. Geophys. Res.*, 114.

Lin, A., Satsukawa, T., Wang, M., Asl, Z. M., Fueta, R., and Nakajima, F. (2016). Coseismic rupturing stopped by Aso volcano during the 2016 Mw 7.1 Kumamoto earthquake, Japan. *Science*, 354(6314) :869–874.

Linde, A. T., Suyehiro, K., Miura, S., Sacks, I. S., and Takagi, A. (1988). Episodic aseismic earthquake precursors. *Nature*, 334 :513–515.

Lomax, A., Michelini, A., and Curtis, A. (2009). *Earthquake Location, Direct, Global-Search Methods.* in Complexity In Encyclopedia of Complexity and System Science, Part 5. Springer, New York.

Loveless, J. and Meade, B. (2011). Spatial correlation of interseismic coupling and coseismic rupture extent of the 2011 Mw = 9.0 Tohoku-Oki earthquake. *Geophysical Research Letters*, 38 :doi :10.1029/2011GL048561.

Marone, C. (1998). Laboratory-derived friction laws and their application to seismic faulting. *Annual Review of Earth and Planetary Sciences*, 26(1) :643–696.

Marone, C., Vidale, J., and Ellsworth, W. (1995). Fault healing inferred from time dependent variations in source properties of repeating earthquakes. *Geophys. Res. Lett.*, 22 :3095–3098.

Marsan, D., Bouchon, M., Gardonio, B., Perfettini, H., Socquet, A., and Enescu, B. (2017). Change in seismicity along the Japan trench, 1990-2011, and its relationship with seismic coupling. *submitted*.

Marsan, D. and Enescu, B. (2012). Modeling the foreshock sequence prior to the 2011, Mw9.0 Tohoku, Japan, earthquake. *Journal of Geophysical Research : Solid Earth*, 117(B6).

Marsan, D., Prono, E., and Helmstetter, A. (2013). Monitoring aseismic forcing in fault zones using earthquake time series. *Bull. Seism. Soc. Amer.*, 103 :169–179.

Matsumoto, Y., Ishikawa, T., Fujita, M., Sato, M., Saito, H., Mochizuki, M., Yabuki, T., , and Asada, A. (2008). Weak interplate coupling beneath the subduction zone off Fukushima, NE Japan, inferred from GPS/acoustic seafloor geodetic observation. *Earth, Planets and Space*, 60(e9).

Matsu'ura, M. and Iwasaki, T. (1983). Study on coseismic and postseismic crustal movements associated with the 1923 Kanto earthquake. *Tectonophysics*, 97 :201–215.

Matsuzawa, T., Asano, Y., and Obara, K. (2015). Very low frequency earthquakes off the Pacific coast of Tohoku, Japan. *Geophys. Res. Lett.*, 42 :4318–4325.

Matsuzawa, T., Hirose, H., Shibazaki, B., and Obara, K. (2010). Modeling short- and long-term slow slip events in the seismic cycles of large subduction earthquakes. *Journal Geophys. Res.*, 115(B12301).

Matsuzawa, T., Igarashi, T., and Hasegawa, A. (2002). Characteristic small-earthquake sequence off Sanriku, northeastern Honshu, Japan. *Geophys. Res. Lett.*, 29(11).

Matsuzawa, T., Uchida, N., Igarashi, T., Okada, T., and Hasegawa, A. (2004). Repeating earthquakes and quasi-static slip on the plate boundary east off northern Honshu, Japan. *Earth Planets Space.*, 56 :803–811.

Mavrommatis, A., Segall, P., and Johnson, K. M. (2014). A decadal-scale deformation transient prior to the 2011 Mw 9.0 Tohoku-Oki earthquake. *Geophys. Res. Lett.*, 41 :4486–4494.

McLaskey, G. C. and Kilgore, B. D. (2013). Foreshocks during the nucleation of stick-slip instability. *Journal of Geophysical Research*, 118(6) :2982–2997.

McLaskey, G. C. and Lockner, D. A. (2014). Preslip and cascade processes initiate laboratory stick-slip. *Journal of Geophysical Research : Solid Earth*, 118(8) :6323–6336.

Mermoz, H. (1976). Imagerie, corrélation et modèles. *Ann. des Télécommunications*, 31 :17–36.

Mitsui, Y. (2015). Interval modulation of recurrent slow slip events by two types of earthquake loading. *Earth, Planets and Space*, 67(56).

Nadeau, R. and Johnson, L. (1998). Seismological studies ar Parkflied VI : Moment release rates and estimates of source parameters for small repeating earthquakes. *Bull. Seism. Soc. Amer.*, 88(3) :790–814.

Nadeau, R. and McEvilly, T. V. (1999). Fault slip rates at depth from recurrence intervals of repeating microearthquakes. *Science*, 285 :718–721.

Nadeau, R. M., Foxall, W., and McEvilly, T. V. (1995). Clustering and periodic recurrence of microearthquakes on the San-Andreas fault at Parkfield, California. *Science*, 267 :503–507.

Nadeau, R. M. and McEvilly, T. V. (1997). Seismological studies at Parkfield V : Characteristic microearthquake sequences as fault-zone drilling targets. *Bull. Seism. Soc. Am.*, 87(6) :1463–1472.

Nakamura, M. and Sunagawa, N. (2015). Activation of very low frequency earthquakes by slow slip events in the Ryukyu Trench. *Geophys. Res. Lett*, 42 :1076–1082.

Nishimura, T. (2014). Short-term slow slip events along the Ryukyu Trench, southwestern Japan, observed by continuous GNSS. *Prog. Earth Planet. Sci.*, 1(22).

Nishimura, T., Sagiya, T., and Stein, R. (2007). Crustal block kinematics and seismic potential of the northernmost Philippine Sea plate and Izu microplate, central Japan, inferred from GPS and leveling data. *J. Geophys. Res.*, 112.

Noda, A., Hashimoto, C., Fukahata, Y., and Matsu'ura, M. (2013). Interseismic GPS strain data inversion to estimate slip-deficit rates at plate interfaces : application to the Kanto region, central Japan. *Geophys. J. Int.*, page doi : 10.1093/gji/ggs129.

Nyst, M., Nishimura, N., Pollitz, F., and Thatcher, W. (2006). The 1923 Kanto earthquake reevaluated using a newly augmented geodetic data set. *J. Geophys. Res.*, 111.

Obara, K. (2002). Nonvolcanic deep tremor associated with subduction in southwest Japan. *Science*, 296 :1679–1681.

Obara, K., Hirose, H., Yamamizu, F., and Kasahara, K. (2004). Episodic slow slip events accompanied by non-volcanic tremors in southwest Japan subduction zone. *Geophys. Res. Lett.*, 31(L23602) :doi :10.1029/2004GL020848.

Obara, K. and Ito, Y. (2005). Very low frequency earthquake excited by the 2004 off the Kii peninsula earthquake : A dynamic deformation process in the large accretionary prism. *Earth, Planets and Space*, 57 :321–326.

Obara, K. and Kato, A. (2016). Connecting slow earthquakes to huge earthquakes. *Science*, 353(6296).

Ohnaka, M. (2003). A constitutive scaling law and a unified comprehension for frictional slip failure, shear fracture of intact rock, and earthquake rupture. *Journal of Geophysical Research*, 108(B2).

Ohta, Y., Hino, R., Inazu, D., Ohzono, M., Ito, Y., Mishina, M., Iinuma, T., Nakajima, J., Osada, Y., Suzuki, K., Fujimoto, H., Tachibana, K., Demachi, T., and Miura, S. (2012). Geodetic constraints on afterslip characteristics following the March 9, 2011, Sanriku-Oki earthquake, Japan. *Geophysical Research Letters*, 39 :L16304.

Ozawa, S. (2014). Shortening of recurrence interval of Boso slow slip events in Japan. *Geophys. Res. Lett*, 41 :2762–2768.

Ozawa, S., Miyazaki, S., Hatanaka, Y., Imakiire, T., Kaidzu, M., and Murakami, M. (2003). Characteristic silent slip earthquakes in the eastern part of the Boso peninsula, Central Japan. *Geophys. Res. Lett.*, 30-6.

Ozawa, S., M.Kaidzu, Murakami, M., Imakiire, T., and Hatanaka, Y. (2004). Coseismic and postseismic crustal deformation after the Mw 8 Tokachi-oki earthquake in Japan. *Earth, Planets and Space*, 56 :675–680.

Ozawa, S., Murakami, M., and Tada, T. (2001). Time-dependent inversion study of the slow thrust event in the Nankai Trough subduction zone, southwestern Japan. *Journal of Geophysical Research*, 106 :787–802.

Ozawa, S., Nishimura, T., Munekane, H., Suito, H., Kobayashi, T., Tobita, M., and Imakiire, T. (2012). Preceding, coseismic, and postseismic slips of the 2011 Tohoku earthquake, Japan. *J. Geophys. Res.*, 117(B07404).

Ozawa, S., Nishimura, T., Suito, H., Kobayashi, T., Tobita, M., and Imakiire, T. (2011). Coseismic and postseismic slip of the 2011 magnitude-9 Tohoku-Oki earthquake. *Nature*.

Ozawa, S., Suito, H., and Tobita, M. (2007). Occurrence of quasi-periodic slow-slip off the east coast of the Boso peninsula, Central Japan. *Earth Planets Space*, 59 :1241–1245.

Ozawa, S., Yarai, H., Imakiire, T., and Tobita, M. (2013). Spatial and temporal evolution of the long-term slow slip in the Bungo Channel, Japan. *Earth Planets Space*, 65 :67–73.

Pacheco, J., Sykes, L., and Scholz, C. (1993). Nature of seismic coupling along simple plate boundaries of subduction type. *J. Geophys. Res*, 98 :14133–14159.

Passelègue, F., Latour, S., Schubnel, A., Nielsen, S., Suresh, H. B., and Madariaga, R. (2014). Precursory processes during stick-slip experiments on crustal rocks. *AGU Fall Meeting Abstracts*, 1(4442).

Peng, Z. and Ben-Zion, Y. (2005). Spatiotemporal variations of crustal anisotropy from similar events in aftershocks of the 1999 M7.4 Izmit and m7.1 Düzce, Turkey, earthquake sequences. *Geophys. J. Int.*, 160 :1027–1043.

Peng, Z. and Zhao, P. (2009). Migration of early aftershocks following the 2004 parkfield earthquake,. *Nature Geoscience*, 2 :877–881.

Perfettini, H. and Avouac, J. (2014). The seismic cycle in the area of the 2011 Mw9.0 Tohoku-Oki earthquake. *Journal of Geophysical Research : Solid Earth*, 119 :4469–4515.

Radiguet, M., Perfettini, H., Cotte, N., Gualandi, A., Valette, B., Kostoglodov, V., Lhomme, T., Walpersdorf, A., Cano, E. C., and Campillo, M. (2016). Triggering of the 2014 mw7.3 Papanoa earthquake by a slow slip event in Guerrero, Mexico. *Nature Geoscience*, 9 :829–833.

Reverso, T. (2015). *Sismogenese dans les zones de deformations transitoires*. PhD thesis, Université Savoie Mont-Blanc.

Reverso, T., Marsan, D., Helmstetter, A., and Enescu, B. (2016). Background seismicity in Boso Peninsula, Japan : Long-term acceleration, and relationship with slow slip events. *Geophysical Research Letters*, 43 :5671–5679.

Rice, J. (1983). Constitutive relations for fault slip and earthquake instabilities. *Pageoph*, 121 :443–475.

Rogers, G. and Dragert, H. (2003). Episodic tremor and slip on the Cascadia subduction zone : the chatter of silent slip. *Science*, 300 :1942–1943.

Rost, S. and Thomas, C. (2002). Array seismology : Methods and applications. *Reviews of Geophysics*, 40(3) :1008.

Ruina, A. (1983). Slip instability and state variable friction laws. *Journal of Geophysical Research : Solid Earth*, 88(B12) :10,359–10,370.

Ruiz, S., Metois, M., Fuenzalida, A., Ruiz, J., Leyton, F., Grandin, R., Vigny, C., Madariaga, R., and Campos, J. (2014). Intense foreshocks and a slow slip event preceded the 2014 Iquique Mw 8.1 earthquake. *Science*, 345 :1165–1169.

Sagiya, T. (2004). Interplate coupling in the Kanto Disctrict, Central Japan, and the Boso Peninsula Silent Earthquake in May 1996. *Pure and Appl. Geoph.*, 161 :2317–2342.

Sagiya, T., Miyazaki, S., and Tada, T. (2000). Continuous GPS array and present-day crustal deformation of Japan. *Pure Appl. Geophys.*, 157 :2303–2322.

Samson, J. (1983). The spectral matrix, eigenvalues, and principal components in the analysis of multichannel geophysical data. *Ann. Geophys.*, 1(1) :115–125.

Sato, T., Hiratsuka, S., and Mori, J. (2013). Precursory seismic activity surrounding the high-slip patches of the 2011 Mw 9.0 Tohoku-Oki earthquake. *Bull. Seism. Soc. Am.*, 103(6) :3104–3114.

Schaff, D., Beroza, G. C., and Shaw, B. E. (1998). Postseismic response of repeating aftershocks. *Geophys. Res. Lett.*, 25 :4549–4552.

Scholz, C. (1990). *The Mechanics of Earthquakes and Faulting.* Cambridge University Press, New York.

Schwartz, S. Y. and Rokosky, J. M. (2007). Slow slip events and seismic tremor at circum-pacific subduction zones. *Reviews of Geophysics*, 45.

Scuderi, M. M., Marone, C., Tinti, E., Stefano, G. D., and Collettini, C. (2016). Precursory changes in seismic velocity for the spectrum of earthquake failure modes. *Nature Geoscience*, 9 :695–702.

Selvadurai, P. and Glaser, S. (2016). Effective strength heterogeneity controlling slow slip events on laboratory faults. *Geophys. Res. Lett.*

Shelly, D., Beroza, G., and Ide, S. (2007). Non-volcanic tremor and low-frequency earthquake swarms. *Nature*, 446 :305–307.

Simons, M., Minson, S., Sladen, A., Ortega, F., Jiang, J., Owen, S., Meng, L., Ampuero, J., Wei, S., Chu, R., Helmberger, D., Kanamori, H., Hetland, E., Moore, A., and Webb, F. (2011). The 2011 Magnitude 9.0 Tohoku-Oki Earthquake : Mosaicking the Megathrust from Seconds to Centuries. *Science*, 332(6036) :1421–1425.

Somerville, P. (2014). A post-Tohoku earthquake review of earthquake probabilities in the southern Kanto District, Japan. *Geoscience Letters*, 1 :1–13.

Steinbrugge, K. V., Zacher, E. G., Tocher, D., Whitten, C. A., and Claire, C. N. (1960). Creep on the San Andreas fault. *Bulletin of the Seismological Society of America*, 50 :389–415.

Suwa, Y., Hasegawa, A., Sato, T., and Tachibana, K. (2006). Interplate coupling beneath NE Japan inferred from three-dimensional displacement field. *Journal of Geophysical Research*, 111.

Takagi, R., Nakahara, H., Kono, T., and Okada, T. (2014). Separating body and rayleigh waves with cross terms of the cross-correlation tensor of ambient noise. *Journal of Geophysical Research : Solid Earth*, 119 :2005–2018.

Tanaka, A., Yamano, M., Yano, Y., and Sasada, M. (2004). Geothermal gradient and heat flow data in and around Japan (i) : Appraisal of heat flow from geothermal gradient data. *Earth, Planets and Space*, 56 :1191–1194.

Thompson, B. D., Young, R. P., and Lockner, D. A. (2009). Premonitory acoustic emissions and stick-slip in natural and smooth-faulted westerly granite. *Journal of Geophysical Research*, 114(B2).

Tocher, D. (1960). Creep rate and related measurements at Vineyard, California. *Bull. Seismol. Soc. Am.*, 50 :396–404.

Toda, S. and Stein, R. (2013). The 2011 M=9.0 Tohoku-Oki earthquake more than doubled the probability of large shocks beneath Tokyo. *Geophys. Res. Letts.*, 40 :1–5.

Toda, S., Stein, R., and Lin, J. (2011). Widespread seismicity excitation throughout central Japan following the 2011 M=9.0 Tohoku earthquake and its interpretation, by Coulomb stress transfer . *Geophys. Res. Lett*, 38.

Tsumura, K. (2005). *National Seismic Hazard Maps for Japan,*. National Seismic Hazard Maps for Japan.

Turek, G. and Kuperman, W. (1997). Applications of matched-field processing to structural vibration problems. *The Journal of the Acoustical Society of America*, 101(3).

Uchida, N. and Matsuzawa, T. (2011). Coupling coefficient, hierarchical structure, and earthquake cycle for the source area of the 2011 off the Pacific coast of Tohoku earthquake inferred from small repeating earthquake data. *Earth Planets Space*, 63 :675–679.

Uchida, N. and Matsuzawa, T. (2013). Pre- and postseismic slow slip surrounding the 2011 Tohoku-oki earthquake rupture. *Earth and Planetary Science Letters*, 374 :81–91.

Uchida, N., Matsuzawa, T., and Hasegawa, A. (2003). Interplate quasi-static slip off Sanriku, NE Japan, estimated from repeating earthquakes. *Geophys. Res. Lett.*, 30(15).

Uchida, N., Matsuzawa, T., Nakajima, J., and Hasegawa, A. (2010). Subduction of a wegde-shaped Philippine Sea plate beneath Kanto, central Japan, estimated from converted waves and small repeating earthquakes. *Journal of Geoph. Res.*, 115.

Uchida, N., Nakajima, J., Hasegawa, A., and T., T. M. (2009). What controls interplate coupling ? : evidence for abrupt change in coupling across a border between two over-lying plates in the NE Japan subduction zone. *Earth and Planetary Science Letters*, 283 :111–121.

Uchida, N., Shimamura, K., Matsuzawa, T., and Okada, T. (2015). Postseismic response of repeating eartqhuakes around the 2011 Tohoku-oki earthquake : Moment increases dure to fast loading rate. *J. Geophys. Res. Solid Earth*, 120 :259–274.

Uenishi, K. and Rice, J. R. (2003). Universal nucleation length for slip-weakening rupture instability under nonuniform fault loading. *Journal of Geophysical Research : Solid Earth*, 108(B1).

Valoroso, L., Chiaraluce, L., Piccinini, D., Stefano, R. D., Schaff, D., and Waldhauser, F. (2013). Radiography of a normal fault system by 64,000 high-precision earthquake locations : The 2009 L'Aquila (central italy) case study. *Journal Geophys. Res.*, 118.

Vandemeulebrouck, J., Roux, P., Gouédard, P., Legaz, A., Revil, A., Hurst, T., Bolève, A., and Jardani, A. (2010). Application of acoustic noise and selfpotential localization techniques to a buried hydrothermal vent (Waimangu Old Geyser site, New Zealand). *Geophys. J. Int*, 180 :883–890.

Vidale, J., Ellsworth, W. L., Cole, A., and Marone, C. (1994). Variations in rupture process with recurrence interval in a repeated small earthquake. *Nature*, 368 :624–626.

Wald, D. and Somerville, P. (1995). Variable-slip rupture model of the great 1923 Kanto, Japan, earthquake : Geodetic and body-waveform analysis. *Bull. Seism. Soc. Amer.*, 85(1) :159–177.

Wallace, L. and Beavan, J. (2010). Diverse slow slip behavior at the Hikurangi subduction margin, New Zealand. *Journal Geophys. Res.*, 115(B12402).

Wallace, L. M., Webb, S. C., Ito, Y., Mochizuki, K., Hino, R., Henrys, S., Schwartz, S. Y., and Sheehan, A. F. (2016). Slow slip near the trench at the Hikurangi subduction zone, New Zealand. *Science*, 352 :701–704.

Wech, A. and Bartlow, N. (2014). Slip rate and tremor genesis in Cascadia. *Geophys. Res. Lett.*, 41 :392–398.

Wei, S., Graves, R., Helmberger, D., Avouac, J.-P., and Jiang, J. (2012). Sources of shaking and flooding during the Tohoku-Oki earthquake : A mixture of rupture styles. *Earth Planet. Sci. Lett.*, 333-334 :91–100.

Wu, F., Okaya, D., Sato, H., and Hirata, N. (2007). Interaction between two subducting plates under Tokyo and its possible effects on seismic hazards. *Geophys. Res. Lett.*, 34.

Yagi, Y., Okuwaki, R., Enescu, B., Kasahara, A., Miyakawa, A., and Otsubo, M. (2016). Rupture process of the 2016 Kumamoto earthquake in relation to the thermal structure around Aso volcano. *Earth, Planets and Space*, 68(118).

Yamanaka, Y. and Kikuchi, M. (2004). Asperity map along the subduction zones in NE Japan inferred from regional seismic data. *Journal of Geophysical Research*, 109(B07307).

Yamashita, Y., Yakiwara, H., Asano, Y., Shimizu, H., Uchida, K., Hirano, S., Umakoshi, K., Miyamachi, H., Nakamoto, M., Fukui, M., Kamizono, M., Kanehara, H., Yamada, T., Shinohara, M., and Obara, K. (2015). Migrating tremor off southern Kyushu as evidence for slow slip of a shallow subduction interface. *Science*, 348 :676–679.

Yokota, Y. and Koketsu, K. (2015). A very long-term transient event preceding the 2011 Tohoku earthquake. *nature communications*.

Yoshioka, S., Matsuoka, Y., and Ide, S. (2015). Spatiotemporal slip distributions of three long-term slow slip events beneath the Bungo Channel, southwest Japan, inferred from inversion analyses of GPS data. *Geophys. J. Int.*, 201(3) :1437–1455.